



January 2017

## Determining Glacier Drift Ages Using Multispectral Remote Sensing Data

Paula Crock

[How does access to this work benefit you? Let us know!](#)

Follow this and additional works at: <https://commons.und.edu/theses>

---

### Recommended Citation

Crock, Paula, "Determining Glacier Drift Ages Using Multispectral Remote Sensing Data" (2017). *Theses and Dissertations*. 2106.

<https://commons.und.edu/theses/2106>

This Thesis is brought to you for free and open access by the Theses, Dissertations, and Senior Projects at UND Scholarly Commons. It has been accepted for inclusion in Theses and Dissertations by an authorized administrator of UND Scholarly Commons. For more information, please contact [und.common@library.und.edu](mailto:und.common@library.und.edu).

# DETERMINING GLACIER DRIFT AGES USING MULTISPECTRAL REMOTE SENSING DATA

---

A thesis submitted for the degree of Masters of Science in the Department of Space Studies/The  
University of North Dakota

**Paula Crock**  
**May 2017**

This thesis, submitted by Paula Crock in partial fulfillment of the requirements for the Degree of Master of Science from the University of North Dakota, has been read by the Faculty Advisory Committee under whom the work has been done and is hereby approved.



\_\_\_\_\_  
Dr. Santhosh Seelan



\_\_\_\_\_  
Dr. Jaakko Putkonen



\_\_\_\_\_  
Dr. Prasad Thenkabail

This thesis is being submitted by the appointed advisory committee as having met all of the requirements of the School of Graduate Studies at the University of North Dakota and is hereby approved.

\_\_\_\_\_  
Grant McGimpsey  
Dean of the School of Graduate Studies

\_\_\_\_\_  
Date

## PERMISSION

Title           Determining Glacier Drift Ages Using Multispectral Remote Sensing Data  
Department   Space Studies  
Degree        Masters of Science

In presenting this thesis in partial fulfillment of the requirements for a graduate degree from the University of North Dakota, I agree that the library of this University shall make it freely available for inspection. I further agree that permission for extensive copying for scholarly purposes may be granted by the professor who supervised my thesis work or, in his absence, by the Chairperson of the department or the dean of the School of Graduate Studies. It is understood that any copying or publication or other use of this thesis or part thereof for financial gain shall not be allowed without my written permission. It is also understood that due recognition shall be given to me and to the University of North Dakota in any scholarly use which may be made of any material in my thesis.

Paula Rena Crock

4 May, 2017

## CONTENTS

CONTENTS.....	iv
LIST OF FIGURES .....	vi
LIST OF TABLES.....	ix
ACKNOWLEDGEMENTS.....	x
ABSTRACT.....	xi
INTRODUCTION .....	1
LITERATURE REVIEW .....	2
BACKGROUND .....	7
Background: Remote Sensing with Earth Observing Satellites.....	8
Background: Glaciers.....	13
Background: Ong Valley Site Field Area .....	14
DATA AND METHODOLOGY.....	20
Data.....	21
Ground Truth Data.....	27
ANALYSIS AND RESULTS.....	29
Analysis: PCA.....	29

Analysis: Empirical.....	40
CONCLUSION.....	53
REFERENCES .....	56
APPENDIX A: MATLAB PROGRAMS.....	60
APPENDIX B: IMAGE CHIPS AND SUB-IMAGES .....	72
APPENDIX C: SUM-IMAGE PIXEL MEAN TABLES.....	96

## LIST OF FIGURES

Figure 1: Classification Results of Iceland’s Langjökull Ice Cap (Pope and Rees, 2014) .....	4
Figure 2: PCA Results from Spectral Data (Pope and Rees, 2014).....	5
Figure 3: Antarctica with Continental US for comparison .....	15
Figure 4: Location of Ong Valley .....	16
Figure 5: Ong Valley Image with Drift Demarcation and Sample Locations (Figure 1 from Bibby, <i>et al.</i> , 2014) .....	17
Figure 6: Ong Valley Base Camp (photo: Jaakko Putkonen).....	18
Figure 7: Ong Valley (Photo: Jaakko Putkonen).....	19
Figure 8: Example Image Set used in Analysis. Data collected February 17, 2011. All images set to same color scale. (a) Band 1, Costal: 400-450 nm, (b) Band 2, Blue: 450-510 nm, (c) Band 3, Green: 510-580 nm, (d) Band 4, Yellow: 585-625 nm, (e) Band 5, Red: 630-690 nm, (f) Band 6, Red Edge: 705-745 nm, (g) Band 7, Near IR-1: 770-895 nm, (h) Band 8, Near IR-2: 860-900nm. ....	23
Figure 9: 22 Dec. 2011 Band 1 full image with image chip outlined (red box). Coordinate values are pixel number relative to full image origin. Color indicates intensity of signal, in digital number counts.....	26
Figure 10: 22 Dec 2011 Band 1 image chip with sub-images for each Region outlined (red boxes). Coordinate values are pixel number relative to image chip origin. Color indicates intensity of signal, in digital number counts.....	26
Figure 11: 22 Dec 2011 Sub-Images from Figure 13. Coordinate values are pixel number relative to sub-image origin. Color indicates intensity of signal, in digital number counts. ....	27

Figure 12: Principal components plot from Table 4 .....	34
Figure 13: Plot of Mean Counts with 1 Sigma Error Bars, 22 Dec. 2011 Data.....	36
Figure 14: Plot of Mean Counts with 1 Sigma Error Bars, 12 Dec. 2013 Data.....	37
Figure 15: Principal components plot from Table 6 .....	40
Figure 16: Normalized Mean Count Values, 22 Dec. 11 data .....	44
Figure 17: Region 1 Sub-Image NDI, 22 Dec. 2011 Data. Coordinate values are pixel number relative to sub-image origin. Color indicates Normalized Drift Index (NDI) value. ....	47
Figure 18: Region 2 Sub-Image NDI, 22 Dec. 2011 Data. Coordinate values are pixel number relative to sub-image origin. Color indicates Normalized Drift Index (NDI) value. ....	48
Figure 19: Region 3 Sub-Image NDI, 22 Dec 2011 Data. Coordinate values are pixel number relative to sub-image origin. Color indicates Normalized Drift Index (NDI) value.....	49
Figure 20: Region 1 Sub-Image NDI, 25 Jan. 2014 Data. Coordinate values are pixel number relative to sub-image origin. Color indicates Normalized Drift Index (NDI) value.....	50
Figure 21: Region 2 Sub-Image NDI, 25 Jan. 2014 Data. Coordinate values are pixel number relative to sub-image origin. Color indicates Normalized Drift Index (NDI) value.....	51
Figure 22: Region 3 Sub-Image NDI, 25 Jan. 2014 Data. Coordinate values are pixel number relative to sub-image origin. Color indicates Normalized Drift Index (NDI) value.....	52
Figure 23: Image Chip from 22 Dec 2011, Band 8.....	72
Figure 24: Region 1 Sub-Image from 22 Dec 2011, Band 8 .....	73
Figure 25: Region 2 Sub-Image from 22 Dec 2011, Band 8 .....	74
Figure 26: Region 3 Sub-Image from 22 Dec 2011, Band 8 .....	75
Figure 27: Image Chip from 13 Dec 2013, Band 8.....	76
Figure 28: Region 1 Sub-Image from 13 Dec 2013, Band 8 .....	77



Figure 29: Region 2 Sub-Image from 13 Dec 2013, Band 8 .....	78
Figure 30: Region 3 Sub-Image from 13 Dec 2013, Band 8 .....	79
Figure 31: Image Chip from 13 Dec 2013 (second image collected), Band 8.....	80
Figure 32: Region 1 Sub-Image from 13 Dec 2013 (second image collected), Band 8 .....	81
Figure 33: Region 2 Sub-Image from 13 Dec 2013 (second image collected), Band 8 .....	82
Figure 34: Region 3 Sub-Image from 13 Dec 2013 (second image collected), Band 8 .....	83
Figure 35: Image Chip from 25 Jan 2014, Band 8.....	84
Figure 36: Region 1 Sub-Image from 25 Jan 2014, Band 8 .....	85
Figure 37: Region 2 Sub-Image from 25 Jan 2014, Band 8 .....	86
Figure 38: Region 3 Sub-Image from 25 Jan 2014, Band 8 .....	87
Figure 39: Image Chip from 2 Feb 2015, Band 8.....	88
Figure 40: Region 1 Sub-Image from 2 Feb 2015, Band 8.....	89
Figure 41: Region 2 Sub-Image from 2 Feb 2015, Band 8.....	90
Figure 42: Region 3 Sub-Image from 2 Feb 2015, Band 8.....	91
Figure 43: Image Chip from 2 Feb 2015 (second image collected), Band 8.....	92
Figure 44: Region 1 Sub-Image from 2 Feb 2015 (second image collected), Band 8.....	93
Figure 45: Region 2 Sub-Image from 2 Feb 2015 (second image collected), Band 8.....	94
Figure 46: Region 3 Sub-Image from 2 Feb 2015 (second image collected), Band 8.....	95

## LIST OF TABLES

Table 1: Relevant Spacecraft and Sensor Specifications for Worldview-2 and Worldview-3 Imagers.....	21
Table 2: Image Data used in PCA Analysis.....	25
Table 3: Sub-Image Aggregate Means for Each Band, as Input to PCA Function .....	32
Table 4: PCA Coefficient Results from Table 3 Input .....	33
Table 5: Sub-Image Means for Each Band using only Shadow-Free Image Sets, as Input to PCA Function.....	37
Table 6: PCA Coefficient Results from Table 5 Input (Non-Shaded Data Sets).....	38
Table 7: Sub-Image Means for Each Band, Color-Coded by Max, Min with Standard Deviation (green = band maximum, orange = band minimum) .....	41
Table 8: Example Pattern 1 Normalized Sub-Image Means, Color-Coded by Max, Min with Standard Deviation (green = band maximum, orange = band minimum) .....	42
Table 9: Example Pattern 2 Normalized Sub-Image Means, Color-Coded by Max, Min with Standard Deviation (green = band maximum, orange = band minimum) .....	43
Table 10: Normalized Band Values Used for Differentiation of Drift Regions 22 Dec. 2011 .....	45
Table 11: Normalized Band Values Used for Differentiation of Drift Regions 25 Jan. 201445	

## ACKNOWLEDGEMENTS

The author would like to thank George Roth and the Polar Geospatial Center at the University of Minnesota for the data used in this research.

## ABSTRACT

Determining the ages of glacier drifts in Antarctica can help paleoclimatologists determine the changes Earth's climate has gone through and thereby inform models for future climate change prediction. However, many of these drifts are difficult to reach for sample collection necessary to determine their ages. This research attempts to use multispectral remote sensing data to expand the mapping of drift ages from known point measurements regionally. This research is based on existing drift ages from Ong Valley, Transantarctic Mountains. Two methods were used to determine a combination of the image band data that would sufficiently distinguish the three age-distinct drift regions: Principal Component Analysis (PCA) and an empirical analysis based on observed trends in the data. The PCA results showed that virtually all bands contribute equally to the differences in the image data from the three drift regions, precluding the use of a small number of bands in an index to classify the regions. An index was developed from the empirical analysis but this index was unable to sufficiently overcome the count variations in the data sets to successfully classify the regions. Although neither method provided a conclusive means to distinguish the drift regions from the remote sensing data used in this analysis other remote sensing data, e.g. – data at different or more extensive bands ranges, or other analysis techniques, e.g. – more preprocessing of the data or machine learning algorithms applied to the image data, may yet yield successful results.

## INTRODUCTION

In the past four decades, with the advent and subsequent rapid growth of satellite remote sensing capabilities, the products of remote sensing technology have gone from those first Landsat images of Earth's varied landscape in the mid-1970s to imagery so ubiquitous that many people with online access can find free images with sufficient resolution to show what color car is parked in their driveway or on the street outside their apartment. Since the use of early aerial photography and pre-Landsat satellites, researchers and scientists have been using remote sensing technology to collect data on objects of interest that would otherwise be difficult or impossible to obtain by any other means. One field that has greatly benefitted from the wealth of data in recent decades is Environment Science. More specifically, the field of glaciology has especially benefitted, given the remote nature and large physical scale of this field's subject.

The research presented in this thesis takes advantage of the wealth of remote sensing data and applies it in a new way to study glaciers – to determine the age of glacier drift with remote sensing. As a glacier retreats, or stagnates and ablates in place, the rock material picked up and transported by the glacier during its advance is left behind or exposed on the surface of the glacier. This material is called glacial drift. Dating glacier drift allows researchers to determine when a glacier retreated or stagnated, which can yield historic glacier states going back thousands, tens of thousands or even millions of years. Traditionally, dating glacial drift is done by collecting *in situ* till samples, transporting these samples back to the laboratory and then measuring their cosmogenic isotope concentrations, which is directly related to the time that has passed since the glacier retreated or stagnated. By analyzing remote sensing data from a glacial valley with known drift ages, determined through cosmogenic isotope dating, this project

attempts to expand the point measurements of ages to mapping a wider region in the same general geological region without the need for sample collection, return and analysis.

## LITERATURE REVIEW

The availability of remote sensing data at a broad range of wavelengths has given researchers a myriad of new ways to approach glacier studies traditionally based upon on site measurements and observations. The most fundamental use of remote sensing data with respect to glaciers is the use of Visible and Near Infrared (NIR) image data to map glacier boundaries to determine a glacier's area and terminus, typically with respect to changes in these parameters over time. Global satellite image data have been available since the launch of Earth Resources Technology Satellite (later renamed Landsat) imaging satellite in 1972 but ground-based and aero-based imagery has been available for substantially longer. Therefore, image data can provide decadal change information for many glacier regions in the world. While there are limitations to the information obtained through imagery data, the substantial collection of images from various satellite programs like Landsat and Terra constitute the core data sets from which glaciologists have determined the global glacier population and the recent changes to it. These results include, for example, detailed time series changes of regional glacier perimeters at both decadal (Bolch, 2007 and Paul, *et al.*, 2007) and seasonal time scales (Bernard, *et al.*, 2013) and maps of Little Ice Age glacier ranges (Wolken, 2006) based on image data.

Issues with using Visible and NIR data to study glaciers include the limitation that these data are only good over sun-lit, cloud-free regions and that the shadowed regions of the glacier can be difficult to successfully incorporate into the analysis. Microwave remote sensing via satellite

provides all-weather, day/night viewing and active, uniform illumination across glacier surfaces even in topographically challenging regions. If images of one scene are taken from sensors with different look angles, the images can be registered to produce topographic information, a process known as Interferometric Topographic Mapping. This is how the digital elevation models are derived, for example. If images are collected from sensors with the same look angles then information can be obtained on changes between the two images, a process known as Interferometric Velocity Mapping (Jensen, 2000). Non-image data like radar interferograms and have allowed researchers to develop glacier flow rates for entire glaciers (Li, *et al.*, 2008) and over entire glacier regions (Luckman, *et al.*, 2007) as well as determine glacier thickness (Lee, *et al.*, 2013).

Finally, the fusion of different remote sensing data types, like image data, digital elevation maps, radar and LiDAR have allowed researchers to determine glacier perimeters in regions that are difficult to study otherwise, such as the frequently cloud covered and topologically challenging terrain of the Indian Himalayan regions (Frey, *et al.*, 2012) and small, debris-covered glaciers (Karimi *et al.*, (2012). These techniques and methods have even been used by planetologists to study glaciers on Mars, including determining seasonal carbon dioxide mass loss from Mars' southern polar ice cap (Schmidt, *et al.*, 2010) and constraining the past mass balance patterns of Mars' northern polar water ice cap (Koutnik, *et al.*, 2009).

New algorithm development has been instrumental in taking advantage of the wealth of information on glaciers available in remote sensing data. These developments include new methods for combining different types of remote sensing data to produce a semi-automated way to classify glacier and non-glacier surfaces (Paul *et al.*, 2004), comparison of statistical and

machine learning classification techniques on heavily debris-covered glaciers (Brenning, 2009), and an assessment of image matching algorithms on different, varied glacier regions around the world (Heid and Kaab, 2012).

Most relevant to this study are past projects aimed at determining the best way to distinguish different glacier surface types using multispectral data. Two of these will be discussed in more detail below.

Pope and Rees (2014) present an analysis of classification of glacier surfaces using full spectrum data to answer this question: which wavelengths are actually the most important in distinguishing between different glacier surface types? They collected full spectrum in situ reflectance spectra data on a variety of surfaces on two glaciers in Iceland in late summer, varieties of clean, dry and debris-covered snow and ice. For image data they selected Landsat

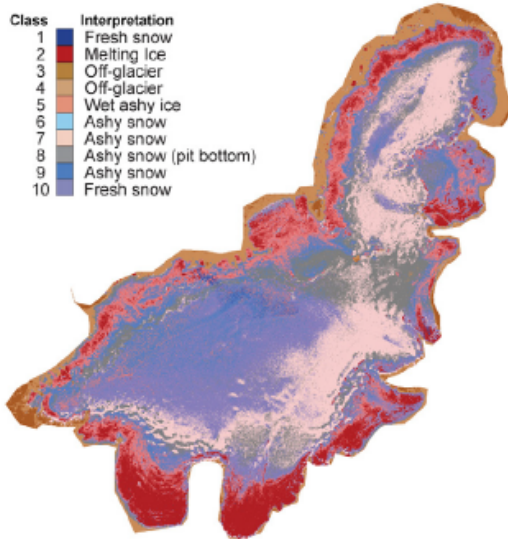


**Figure 1: Classification Results of Iceland's Langjökull Ice Cap (Pope and Rees, 2014)**

EMT+ data from 2000. The image data was classified using an unsupervised ISODATA classification technique with a result of 10 different surface classes for glacier regions in the image. Figure 1 shows the classification results for one of the two glaciers. A qualitative analysis was done comparing the spectral information with classified



satellite imagery to determine important areas to investigate and to try to associate spectral features with physical properties of the glacier. This qualitative analysis revealed that brighter classes, i.e. - those with more reflectance, are associated with higher elevations and darker classes are associated with lower elevations.

This suggests that brighter classes are associated with accumulation regions and darker classes are associated with ablation regions. However, there was no clear way to distinguish intermediate regions based on the image data classification. Following the qualitative analysis, a quantitative analysis was done using principal component analysis (PCA) on each glaciers spectral data to determine which wavelengths contribute the most to differentiating surface classes. The PCA resulted in three principal components from each data set. A plot of the PCA

results, shown in Figure 2, revealed several key points.

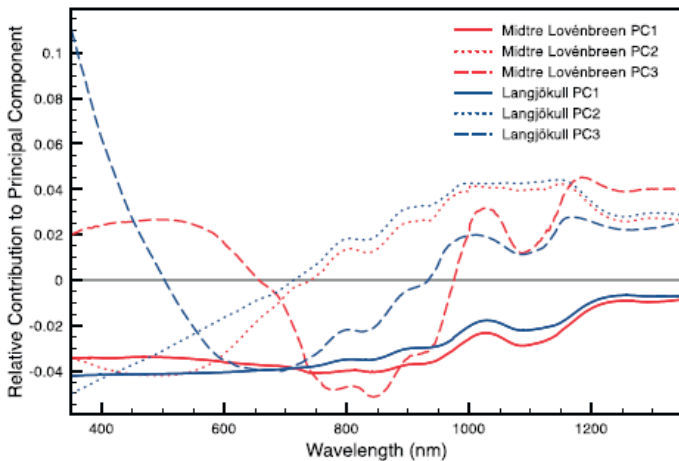


**Figure 2: PCA Results from Spectral Data (Pope and Rees, 2014)**

First, component 1, which accounts for 98% of the variation and is associated with broadband albedo, is consistent for both glacier data sets and doesn't exhibit much variation across the spectrum.

Second, component 2, which accounts for ~ 1.5% of the variation,

is likewise consistent between the two data sets. Unlike component 1, however, it does exhibit a change across the spectrum, with positive values on the blue end of the spectrum and negative

values on the red end, with the switch occurring at about 750nm. This slope indicates that the difference between blue reflectance and NIR reflectance is an important distinguishing characteristic. Third, component 3, which accounts for ~ 0.5% of the variation, differs more than the other two components between the data sets but has a consistent sign change in the middle part of the spectrum. This indicates that the difference in brightness between the middle part of the spectrum and the ends is also a distinguishing characteristic. Using the observations from the PCA results, and after mapping the spectra data onto the EMT band regions, the following linear combinations of ETM+ bands were found to give the most distinguishable surface characteristics, where the coefficients for each band, e.g.  $-\frac{1}{2}$  for wet ice band 2, are rounded-off PCA coefficients:

snow: band 1 + band 2 + band 3 + band 4

wet ice: band 1 +  $\frac{1}{2}$ (band 2) –  $\frac{1}{2}$ (band 3) - band 4

dry ice: band 1 –  $\frac{1}{2}$ (band 2) – band 3 +  $\frac{1}{2}$ (band 4)

As a conclusion of their analysis Pope and Rees stated that aside from surfaces with ash or debris, hyperspectral data such as the in situ spectra data sets do not give significantly more information for glacier classification than visible and near IR data do.

Salvatore, *et al.* (2014) conducted an extensive project combining laboratory sample analysis and remote sense data analysis to determine the chemical variations in surface dolerite of the Dry Valleys in Antarctica. The team conducted substantial laboratory analysis of 64 samples collected *in situ* throughout the Dry Valleys including spectral analysis on all 64 samples and

spectroscopy on 18 dolerite samples to obtain bulk chemistry. They also collected *in situ* VNIR calibration data at three sites. Advanced Land Imager (ALI) and Advanced Spaceborn Thermal Emission and Reflection Radiometer (ASTER) remote sensing data were used after processing with ENVI software and a significant amount of custom processing including converting the digital number counts to spectral radiance value, and then correcting for atmospheric transmission. The *in situ* calibration data was used to ensure that values between the ALI and ASTER data sets were in agreement after atmospheric correction. The calibrated and corrected image data combined with laboratory spectral analysis of dolerite samples collected *in situ* allowed the team to produce maps of pure dolerite deposits and maps of regions characterized by unaltered Mg-rich dolerite, unaltered Mg-poor dolerite, and altered Mg-poor dolerite. The team discovered that this analysis works better on fine-grained dolerite than coarse-grained dolerite because weathering of the coarse-grained dolerite removes the chemical spectral signatures used to characterize different Mg chemical variations.

## BACKGROUND

As the previous section outlines, a substantial amount of research has been done using remote sensing data to study glaciers throughout this world and beyond. This thesis adds to that body of work by addressing the specific topic of glacier drift ages, and even more specifically the drifts of the Ong Valley in the Transantarctic Mountains. This background section provides relevant fundamentals of remote sensing with respect to Earth observing satellites, including common satellite and sensor parameters, an outline of the current satellite constellation and more specific information on the particular remote sensing satellites whose data are used for this project. This section also includes background on glaciers in general and on the specific field site used in this study, the Ong Valley, including the previous research on its drifts that this project is based on.

## Background: Remote Sensing with Earth Observing Satellites

Remote sensing in general is the act of collecting data on an object without being in physical contact with the object. A very common method of collecting remote sensing data is through Earth observing (EO) satellites. What started as a constellation of one satellite in 1972 with Earth Resource Technology Satellite 1, later renamed Landsat 1, has blossomed into more than 60 EO satellites with dozens more set to launch over the next decade. Along with the number of satellites, there has been tremendous progress in the science and engineering of EO satellites both in hardware, as ever more sophisticated instruments are developed, in data archiving and distribution aided by remarkable advances in data storage media capabilities and data transfer rates of the internet, and in the commercialization of remotely sensed data. There has also been growth in the number of countries with their own satellite industry, including many developing countries.

Earth observing satellites typically operate in polar (passing over or near the North and South Pole), low Earth orbit (LEO, below 2000 km) so as to obtain near-global coverage. These satellites are also commonly sun-synchronous, meaning that they pass over the same region on Earth at the same time each day, which allows them to observe day-to-day changes without the effects of local time difference, e.g. – different shadow lengths. Orbit periods for low Earth orbit EO satellites are on the order of 100 minutes and ground tracks, the area of Earth directly under the satellite, shifts about 25 degrees per orbit due to Earth's rotation. Thus a LEO satellite will be back over the exact same location every ~ 14 orbits. Landsat 7, for example, orbits at 702km, has an orbital period of 98.9 minutes, with 14.5 orbits per day and returns to the exact same orbital location every 16 days. While a satellite may take many days to be over the exact same spot of an earlier pass, the ability to tilt or steer the sensors allows for viewing of the same location –

albeit from slightly different angles – much more frequently. The time between successive viewing possibilities is called a satellites revisit time. Some EO satellites, such as weather satellites, are in geosynchronous orbit, enabling them to see the same 1/3<sup>rd</sup> of Earth at all times.

With a few exceptions, the sensors on EO satellites are designed to collect photon data at one or more wavelength bands, from UV (0.4  $\mu\text{m}$ ) to radio (> 100 cm). However, due to atmospheric absorption at many regions of the electromagnetic spectrum, most sensors operate in the Visible, IR and microwave regions of the spectrum, where atmospheric absorption windows exist. These sensors are characterized primarily by spatial resolution, spectral resolution, radiometric resolution, and swath width. Spatial resolution is the minimum size of an object that can be resolved in an image. Spectral resolution is the minimum resolvable difference in wavelength for an image, or, equivalently, the width of the spectral bands that a sensor collects data in, e.g. – the Landsat 7 EMT+ sensor's blue band collects data between wavelengths of 0.45-0.52 micron. Radiometric resolution is the minimum difference possible between intensity levels in an image. Swath width, partially determined by orbit and partially determined by sensor characteristics, is the ground distance covered by an image.

Current EO technology is a well-developed field -- the present day remote sensing satellite constellation has spatial resolution down to under a meter. Furthermore, there are sufficient ground receiving stations that data can be disseminated in less than a day in emergency situations: based on a presentation given by Wang Xiaoming at the 13<sup>th</sup> DMC Consortium Meeting, data from Beijing-1 was given to the UN Office for Outer Space Affairs within 17 hours of the Haiti earthquake and less than 12 hours after the request was received. The systems

that make this remarkable accomplishment possible include the combination of the science and engineering of the remote sensing satellite systems themselves and the storage, distribution and commercialization of the resulting data and data products.

As of November 2011, the Committee on Earth Observing Satellites (COES) Missions, Instruments and Measurements database lists a total of 63 multi-purpose EO satellites. Of these, 49 are multi-purpose land imagery measurement satellites, three measure landscape topography, three measure snow cover, edge and depth, three measure soil moisture, two measure land surface temperature and three measure vegetation. The technology and application of each of these measurement types will be discussed separately.

Multi-purpose land imagery satellites, which make up the bulk of the list, are primarily used to produce spatial information on surface features but are also used to collect data for many of the other measurements listed. They generally collect data via multi-spectral or hyperspectral Visible and Infrared (IR) sensors. The spatial resolution of these sensors ranges from coarse, like the 120 m thermal IR band of Landsat TM, to very high, like the < 1 m Quickbird. Swath widths range from large-scale / global scenes like the 180 km Landsat TM to imaging radar (synthetic aperture radar, SAR) with small scenes like the 2.1x0.8 m SAR on RADARSAT-2. SAR has the added advantage of not being blocked by clouds. Moderate scene sized sensors like the 23.5 m LISS-III on Resourcesat-2 are useful as well, since the regional-scale information from them is used in a wide range of research and resource-management areas, e.g. – forestry, agriculture, disaster management, civil planning, etc. The public is most familiar with this type of satellite imagery due to widely adopted mapping software applications like Google Earth™. The data used in this thesis project comes from imaging satellites WorldView-2 and WorldView-3, which sport high spatial resolution (0.31 m – 2.4 m, depending on band) multi-spectral sensors with a

swath width of 16.4 km at nadir. The data for this project was collected by multi-purpose land imagery satellites WorldView-2 and WorldView-3.

Landscape topography satellites are used primarily to produce information on the height of land surface features through digital elevation maps (DEMs). The data used to generate these maps is gathered using multi-band imagers and SARs to produce stereoimages or with radar altimeters like the SIRAL on CryoSat-2. Digital elevation maps have many uses including flood prediction, civil planning and monitoring/predicting natural disasters.

Snow cover and ice sheet mapping satellites provide valuable information on climate change. Some data is collected using multi-frequency imaging microwave sensors like the SSM/IS on DMSP F-18 or with radar altimeters like SIRAL on CryoSat-2. RADARSAT imaging radar data was used to create the first high-resolution map of Antarctica. Multi-spectral data from TM or MODIS can be used to calculate a normalized difference snow index similar to NDVI for vegetation that can be used as a threshold brightness to characterize snow-covered versus non-snow-covered land (Dozier, *et al.* 2004). Hyperspectral imagery is also used to extract snow and ice characteristics like grain size.

Soil moisture content is also obtained, generally, from satellites via multi-frequency imaging microwave sensors like the TMI aboard TRMM. However, soil moisture is difficult to measure due to high signal to noise ratios over the smaller surface areas (10s of km) that users typically want measurements for. The MIRAS radiometer on SMOS was built specifically to measure sea surface salinity and soil moisture by employing a new measurement technique using a 2-D interferometer radiometer to address the spatial resolution problem with imaging microwave sensors. MIRAS consists of a y-shaped array of 69 antennae elements, each of which is an L-

band sensor. This configuration of elements provides resolution similar to an 8 m antenna and has a spatial resolution of 35 – 50 km. Soil moisture is used in agriculture and in conjunction with other data to predict weather and climate change.

Land surface temperature is measured in medium- to high-resolution IR band sensors aboard many satellites. The VHRR instrument on KALPANA-1 and the INSAT satellites measure temperatures from geostationary orbits with a spatial resolution of 8 km while the VIIRS sensor suite on the NPOESS pathfinding mission NPP measure surface temperature from a sun-synchronous non-geostationary orbit with a resolution of 0.4 to 1.6 km. Land surface temperature information is used quite widely, for example in volcano and fire monitoring, in predicting the heat effects of urban areas, and in predicting best planting times and frost risk in agriculture.

Vegetation measurements are taken using multi-spectral Visible and IR sensors such as the 1-3 km resolution SEVRI radiometer on the Meteosat satellites or for higher resolution with SAR such as the 3-8 m resolution SAR-X on the RISAT satellites. A large amount of data has also been collected by Landsat TM and ETM+, and other multi-purpose sensors (Xie, *et al.* 2008). Global, continental, regional and local resolution data are widely available. These measurements typically consist of red and near-IR bands because vegetation shows characteristic relative relationships among these bands. Data from these bands are typically combined into a single value (e.g. – NDVI from AVHRR and EVI from MODIS) that characterizes the health of the vegetation since this value is related to the amount of photosynthesis occurring. Vegetation measurements at the local and regional level can be used to monitor crops while continental and global measurements can be used to monitor entire ecosystems. The 40-year history of Landsat data provides a ready means to quantify vegetative land cover change over time.



## **Background: Glaciers**

Glaciers are large, dynamic masses of freshwater ice that persist over many years. This ice is formed by snowfall in accumulation regions which slowly, over decades to hundreds of years, turns to ice as the accumulating mass of fresh snow compresses older snow into ice crystals. This increasing mass also slowly forces the flow of older ice downward to ablation regions, generally at lower elevation, where the ice is lost to melting, evaporation or calving. When accumulation happens more rapidly than ablation the glacier advances; when ablation happens more rapidly than accumulation the glacier retreats. The mass balance of a glacier is the difference between its accumulation and ablation. Given that glacier mass is gained through snowfall and lost when ice is evaporated or melted, glacier advance or retreat is dependent on both change in precipitation and change in temperature. Common glacier features are crevasses, large cracks that can form when glaciers flow quickly, and moraines, rocky fields that become scattered across glacier surfaces and along the edges due to the glacier scraping along rocky surfaces as it flows and/or rockfalls onto the glacier's surface.

Glaciers grow or shrink based on the local climate. In turn, this growth or shrinkage by a glacier can impact, sometimes dramatically, the environment around it both on short time scales like seasons and longer time scales like decades or centuries. For example, the release of fresh water through melting of glaciers can have a significant impact on humans for good or ill. Much of the world's population depends on fresh water runoff from seasonal glacier melt for drinking water, agriculture and hydroelectric power. And conversely, sudden release of glacial lakes can cause devastatingly destructive flooding. On a longer time scale, a continued trend of melting can deplete glaciers and use up the stored fresh water supply that these communities depend on.

According to the Intergovernmental Panel on Climate Change (Confalonieri, 2007) greater than 1/6th of the world's population will be impacted by a decrease in the water volume from decreasing glaciers. Furthermore, as glaciers are sensitive to yearly temperature trending, glacier retreats or advances can serve as an early indication of global climate change. Another way changing glaciers can change the environment is that glaciers also cause sea level rise due to melting. According to a different report from the Intergovernmental Panel on Climate Change (Lemke, 2007) global glacier melt contributed  $0.37 \pm 0.16$  mm/yr to sea levels from 1961 – 1990 but  $0.77 \pm 0.2$  mm/yr from 1990 – 2003. Therefore the changing state of glaciers is of interest to environmental scientists, hydrologists, farmers, emergency planners and many others outside the field of glaciology.

The basic properties of glaciers that can be determined from remote sense data is glacier perimeter and area, but change data in those properties over time can yield glacier retreat or advance trends, flow rate, and mass balance; furthermore, global glacier change data can give information about the state of the global climate. Recent advances in remote sensing technology and methodologies for using the resulting data have led to three-dimensional mapping of glaciers as well.

### **Background: Ong Valley Site Field Area**

Antarctica is the coldest, windiest, driest and highest continent on Earth. It is located almost entirely within the Antarctic Circle and has a land surface that is 98% covered by ice, which averages almost 2 km thick over the continent. There is no indigenous population on the continent. Antarctica covers 14 million km<sup>2</sup>, significantly larger than the continental US (Figure 5).



**Figure 3: Antarctica with Continental US for comparison**

The specific location used for this research project is the Ong Valley in Antarctica's Transantarctic Mountain Range (Figure 6). The Ong Valley is approximately 9 km long by 3 km wide, and is located in the Miller Range. Unlike much of Antarctica this valley is mainly free of exposed ice, although a large fraction of the valley is underlain by ancient glacier ice.

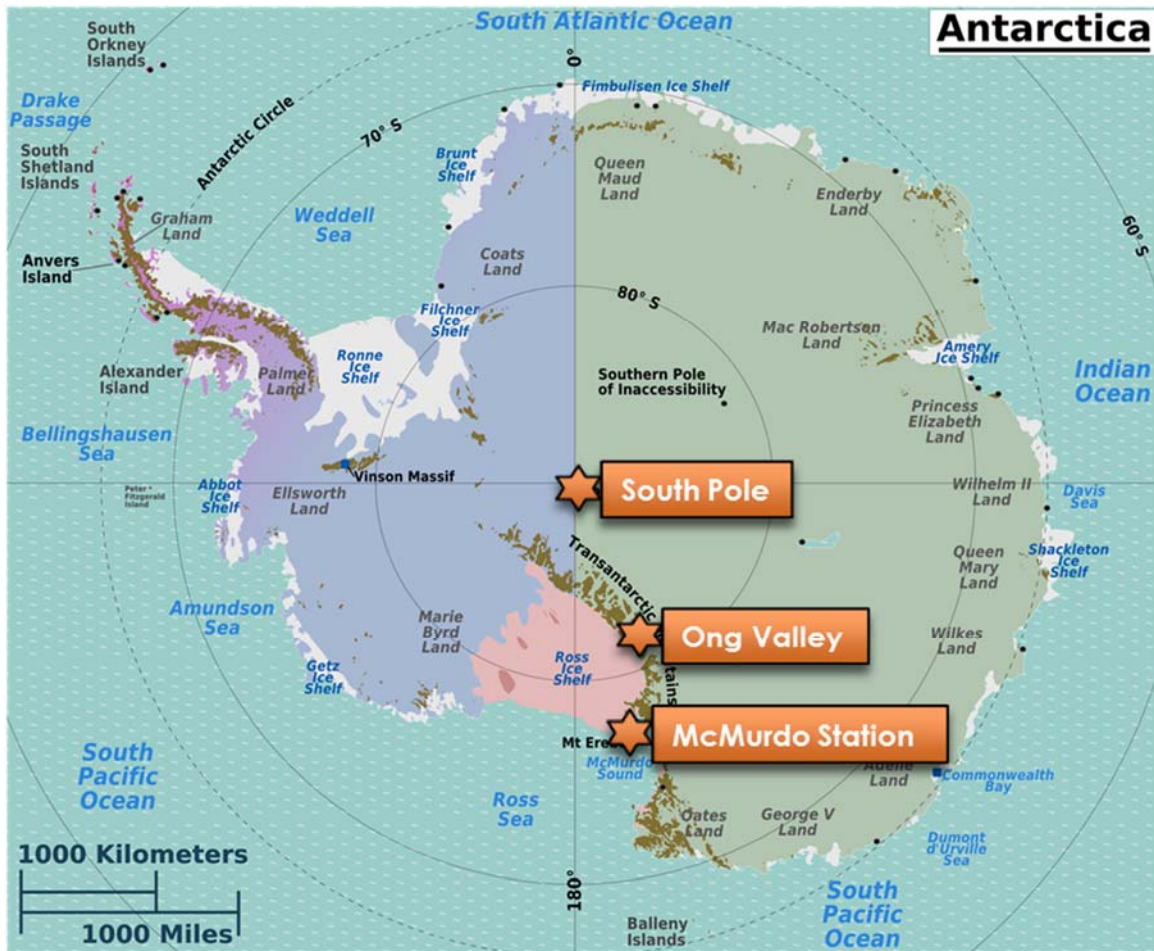


**Figure 4: Location of Ong Valley**

Although the Ong Valley is very remote (anecdotally more people have been to the Moon than to Ong Valley), the drifts in this valley have been studied and samples collected by Dr. Jaakko Putkonen, Director of Harold Hamm School of Geology & Geological Engineering at University of North Dakota, and his team. This on-site survey, sample collection and the subsequent laboratory analysis done on the samples have yielded ages for each of the three distinct drift regions in the valley, results which were published by Bibby, *et al.* (2016). Figure 7, which is from Bibby, *et al.*, is a satellite image overlaid with dashed lines showing the extent of each of the three drift regions and indicating where test profile samples were collected. The head

of the valley has an unnamed glacier (Figure 7, upper left). The entrance to the valley (Figure 7, lower right) is blocked by a lobe from Argosy Glacier that fills the 2km wide valley entrance.

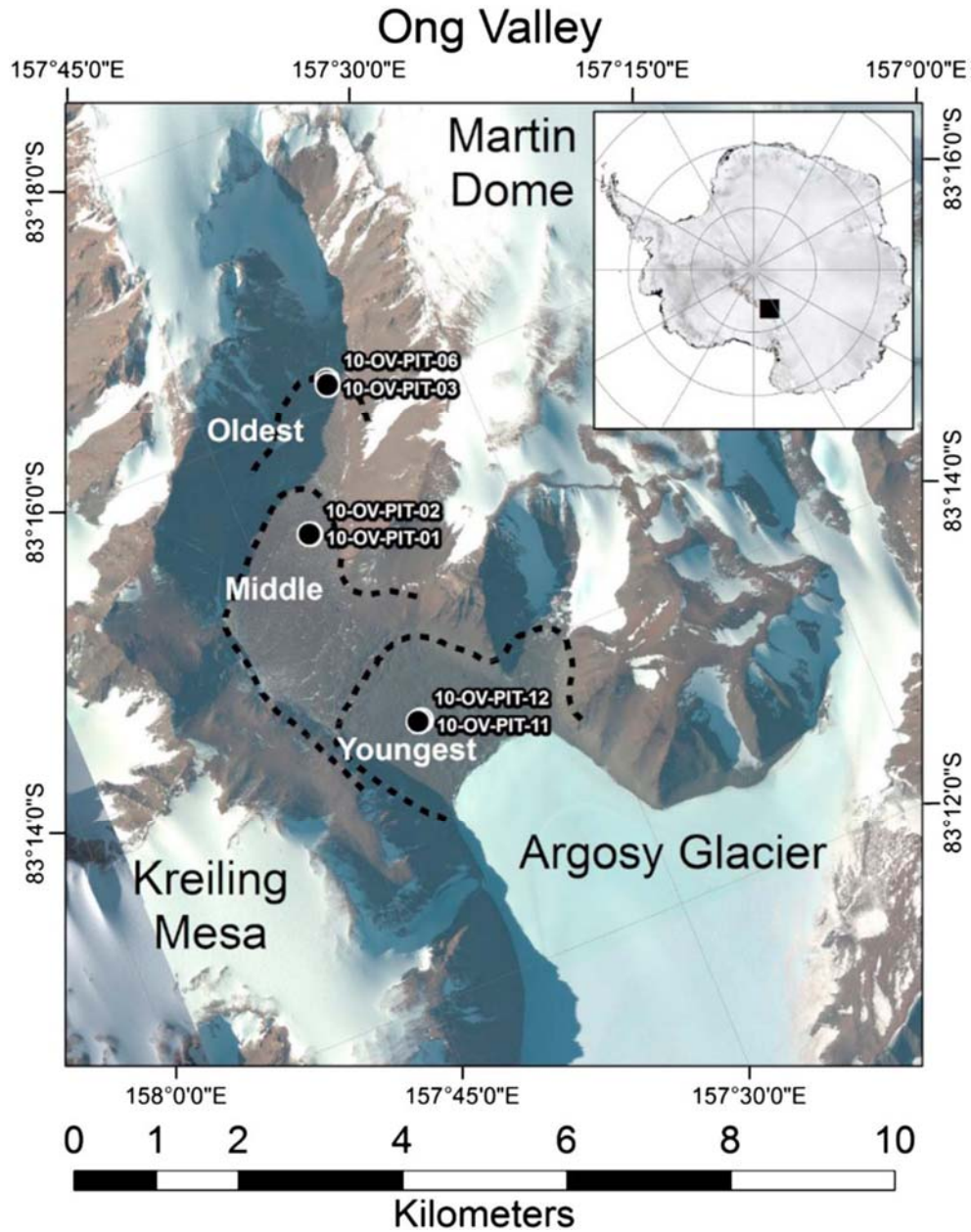


Figure 5: Ong Valley Image with Drift Demarcation and Sample Locations (Figure 1 from Bibby, *et al.*, 2014)

The field research team concluded that most of the Ong Valley floor consists of three drifts (Figure 7, dashed lines), which are each composed of unconsolidated sedimentary deposits of different ages. The rest of the valley floor consists of talus from the surrounding bedrock outcrops of the valley walls. Much of the sedimentary deposits have naturally formed into patterned ground polygons due to contraction cracking of the till (Figure 8, upper half). For a sense of scale, the four yellow dots on the ice patch (white area) of Figure 8 are individual camping tents while the larger multicolor item is a larger tent structure. A person can be seen walking across the ice patch towards the larger tent structure. Finally, Figure 9 is a photograph taken from near the head of the valley looking up towards the entrance and Argosy Glacier, at approximately the 'e' in the 'Oldest' text on Figure 7.



**Figure 6: Ong Valley Base Camp (photo: Jaakko Putkonen)**

The research team at Ong Valley determined from field observations that the three distinct lobe-shaped regions (Figure 7, dashed lines) correspond to three previous pairs of advance and subsequent retreat stages of Argosy Glacier into the valley. The ultimate question the team wanted to answer was what the ages of the drifts are, and subsequently when these three glacial retreats occurred. Glacial advance plucks rocky debris from the surface it is flowing over and this debris gets carried along as the glacier advances. When the glacier subsequently retreats, the plucked rock that flowed with it during advance is left behind as drift; therefore, rock that was once buried under ice is now exposed on the surface of Earth after the glacier retreats. Part of that exposure includes high energy cosmic rays, which interact with the atoms, knocking out neutrons or protons from the nucleus, creating an isotope that is otherwise very rare. The amount

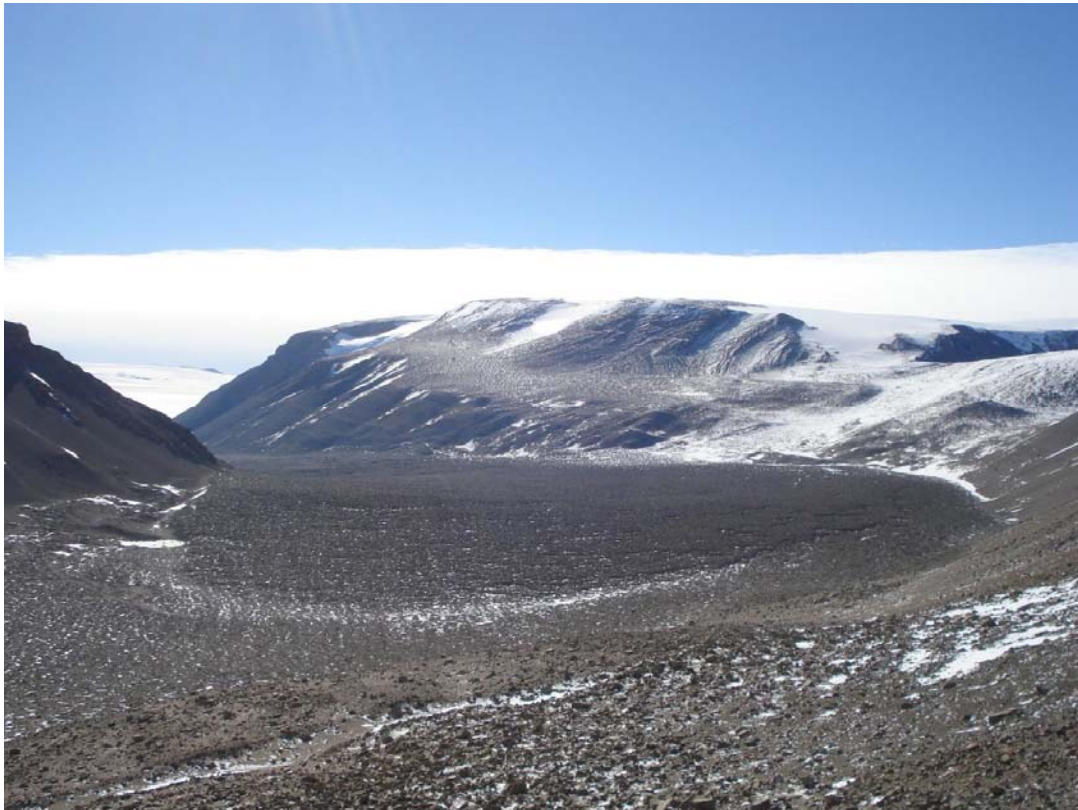


**Figure 7: Ong Valley (Photo: Jaakko Putkonen)**

of these cosmogenic-induced isotopes, cosmogenic nuclides, in a rock sample is directly proportional to the amount of time the rock has been exposed on the surface of Earth.

Therefore, determining the amount of cosmogenic isotopes in rocks from the different drift regions of the Ong Valley will allow determination of the ages of the drifts. The team collected drift samples at several locations in the valley (Figure 7, black circles). From cosmogenic dating analysis, the team concluded that the oldest drift is at least 1.56 Ma and likely older than 2.63 Ma, the middle drift is at least 1.1 Ma and likely greater than 1.78 Ma, and the youngest drift is 11 – 13 ka.

With this ground truth data and available remote sensing data of the region, the Ong Valley is an ideal choice to determine if remote sensing data can be used to differentiate glacier drifts of varying ages and/or same age drifts in the general region of the central Transantarctic Mountains.

## DATA AND METHODOLOGY

Multispectral remote sensing image data sets were obtained and assessed for suitability in the analysis, processed to extract sub-images from each drift region in the image and then used in a principal component analysis (PCA) to determine the best way to qualitatively characterize the drift regions using remote sensing data and to determine which spectral bands would be most useful in differentiating the regions. These PCA results combined with the ground truth data will be used to determine a method to quantitatively characterize the drift region ages based on remote sensing data.



## Data

The remote sensing data for this study came from the WorldView-2 and WorldView-3 satellites. WorldView-2, launched in 2009, and WorldView-3, launched in 2014, are commercial Earth-observing imagers, each slightly larger than a minivan (excluding solar arrays), that are owned and operated by DigitalGlobe. Both are in sun-synchronous orbits with periods of about 100 minutes. Table 1, which is based on data from Satellite Image Corporation’s web site [www.satimagingcorp.com](http://www.satimagingcorp.com), gives the relevant specifications for these two imaging satellites.

**Table 1: Relevant Spacecraft and Sensor Specifications for Worldview-2 and Worldview-3 Imagers**

Specification	WorldView-2	WorldView-3
Launch Date	October 8, 2009	August 13, 2014
Orbit Altitude	770 km	617 km
Orbit Type	Sun synchronous, 10:30 am (LT) descending Node	Sun synchronous, 1:30 pm (LT) descending Node
Orbit Period	100 minutes	97 minutes
Spacecraft Size, Mass, & Power	4.3 m (14 ft) tall x 2.5 m (8 ft) across, 7.1 m (23 ft) across the deployed solar arrays; 2800 kilograms (6200 pounds); 3.2 kW solar array, 100 Ahr battery	5.7 m (18.7 ft) tall x 2.5 m (8 ft) across, 7.1 m (23 ft) across the deployed solar arrays; 2800 kilograms (6200 pounds); 3.1 kW solar array, 100 Ahr battery
Sensor Bands	Panchromatic: 450-800 nm  8 Multispectral: (red, red edge, coastal, blue, green, yellow, near-IR1 and near-IR2) 400 nm - 1040 nm	Panchromatic: 450-800 nm  8 Multispectral: (red, red edge, coastal, blue, green, yellow, near-IR1 and near-IR2) 400 nm - 1040 nm
Sensor Resolution	Panchromatic Nadir: 0.46 m GSD at Nadir, 0.52 m GSD at 20° Off-Nadir  Multispectral Nadir: 1.84 m GSD at Nadir, 2.4 m GSD at 20° Off-Nadir	Panchromatic Nadir: 0.31 m GSD at Nadir, 0.34 m at 20° Off-Nadir  Multispectral Nadir: 1.24 m at Nadir, 1.38 m at 20° Off-Nadir
Sensor Dynamic Range	11 bits per pixel	11 bits per pixel

The WorldView data used in this project were provided by the Polar Geospatial Center at the University of Minnesota. This data set includes 190 GB (120 image sets) of data collected from 2010 to 2015. The data are minimally processed with just radiometric correction and sensor correction performed. These data consist of .tif image files containing an 8192 by 9216 by 8 raster image stack (8192 pixels tall by 9216 pixel wide with one image per band) and associated metadata xml files. The metadata files contain information such as image dimensions, latitude and longitude of each corner of each image in the stack, timestamp for when the image was taken, collection parameters like swath mode, and cloud cover. The metadata files were used to filter out images that were not sufficient for PCA analysis, although these images may still be useful for testing the PCA results. Images were rejected for PCA analysis using a basic algorithm: if they did not contain the center coordinate of the valley (-83.2333333 latitude, 157.6166667 longitude) or if they had > 25% of cloud cover they were rejected. A MATLAB script was written to select out all image files that met the criteria listed above. However, although the metadata file contains a cloud cover value, these values were found to be unreliable. Therefore, each image that passed the test of containing the center of the valley was assessed for cloud cover manually. This two-step filtering process resulted in 10 image files sufficient for use in the analysis, 8 from WorldView-2 and two from WorldView-3. Some of these 10 image files do not contain the entirety of the valley or contain only small, cloud-free parts of the valley; these will be used to test the PCA analysis results. Below is a representative set of images, one for each band, from data collected on February 17, 2011.

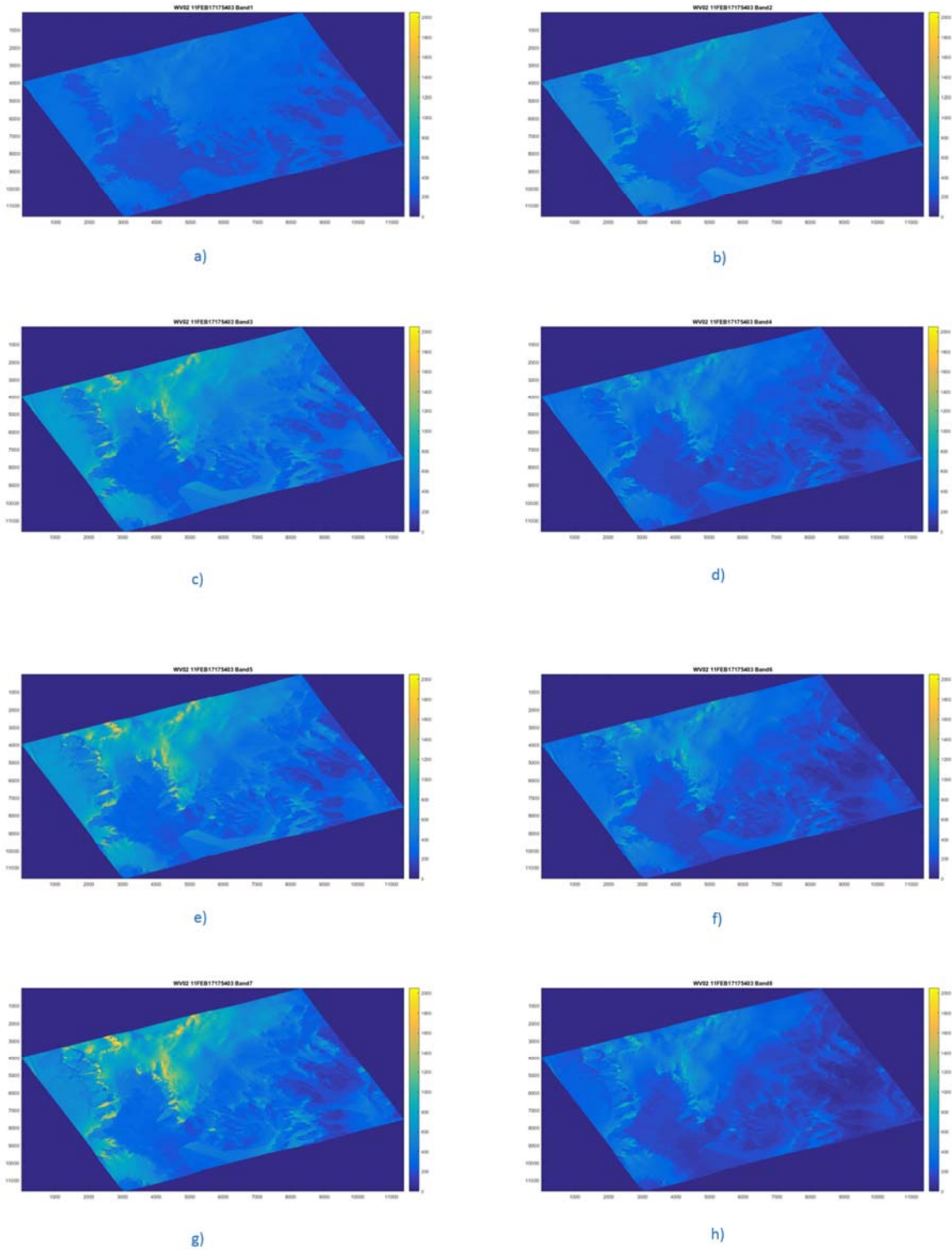


**Figure 8: Example Image Set used in Analysis. Data collected February 17, 2011. All images set to same color scale. (a) Band 1, Coastal: 400-450 nm, (b) Band 2, Blue: 450-510 nm, (c) Band 3, Green: 510-580 nm, (d) Band 4, Yellow: 585-625 nm, (e) Band 5, Red: 630-**

**690 nm, (f) Band 6, Red Edge: 705-745 nm, (g) Band 7, Near IR-1: 770-895 nm, (h) Band 8, Near IR-2: 860-900nm.**

Due to the size of the full image data sets, an image chip containing just the Ong Valley was extracted from the full image for each of the data sets to minimize processing time. The image chip row and column pixel ranges are given in Table 2 and are relative to the full image 8192 by 9216 pixel size. After extracting image chips from each full image, three sub-images containing a representative section of each of the three drift regions of the valley was extracted from each image chip. Each region was manually identifiable because each of the three regions is visually distinct in the image chip, as are the termini between each of the regions. These row and column ranges are different for each image in the analysis, i.e. - data sets from each of the three regions are not necessarily the same size, but the row and column ranges are the same for each band within an image set. The pixel values from these sub-images, three sub-images for each of the eight bands per image file, are the data used in the analysis for this project. Table 2 lists the row and column pixel ranges, relative to the image chip, for each of the three regions in each data file. The green data rows in the table were the sub-image data sets used as input to the PCA function. The rows in white were not sufficient for PCA analysis input but can be used to assess performance of PCA results.

Figure 12 and 13 show the relationship between the full image, the image chip and the three sub-images.

**Table 2: Image Data used in PCA Analysis**

Filename	Image Chip	Region 1 (oldest drift)	Region 2	Region 3 (youngest drift)
WV02_10DEC21180354_103001000817E D00_10DEC21180354-M1BS- 500092301160_01_P010_u16ns3031	4630:10060, 1607:5520	Shaded	3078:3509, 1619:2066	3814:4207,2606:2981
WV02_11DEC22195305_1030010010AA EE00_11DEC22195305x2DM1BS0x2D5 0	1530:5728, 5380:9334	1414:1710 ,1770:1953	2254:2480 , 1565:1856	2980:3327 , 2318:2771
WV02_11FEB17175403_10300100092952 00_11FEB17175403x2DM1BS0x2D50	4469:10450, 1273:6189	Cloud Cover	3144:3565 ,2347:2682	4187:4403 , 3295:3716
WV02_13DEC13163520_103001002B973 000_13DEC13163520x2DM1BS0x2D50	4469:10450, 1273:6189	1665:2030 ,1249:1389	2693:3038 ,1028:1319	3336:3609 ,1621:2192
WV02_13DEC13163632_103001002A0A9 500_13DEC13163632x2DM1BS0x2D50	2586:6913, 2299:6195	1407:1752 ,1718:1894	2576:3055 ,1463:1875	3141:3472 ,2218:2765
WV02_14JAN25201052_103001002B37A 900_14JAN25201052x2DM1BS0x2D50	2642:7541, 5166:8729	2067:2419 ,1613:1828	2791:3492 ,1266:1755	3683:4000 ,2172:2764
WV02_15FEB02191005_103001003C260 800_15FEB02191005x2DM1BS0x2D50	2535:7464, 4610:7603	1543:1822 ,1065:1200	2520:3273 ,887:1204	3302:3623 ,1510:2152
WV02_15FEB02191125_103001003CC6E 400_15FEB02191125x2DM1BS0x2D50	2169:6835, 4404:7659	1712:1967 ,1291:1449	2626:3503 ,1138:1376	3430:3778 ,1756:2161
WV03_14NOV01201351_10400100047E1 900_14NOV01201351x2DM1BS0x2D50	6943:12510, 4606:8992	1998:2617 ,2696:2953	2037:4234 ,2342:2863	Not in Image
WV03_14NOV01201353_10400100047E1 900_14NOV01201353x2DM1BS0x2D50	1492:5964, 2792:7363	Not in Image	895:1935 ,1161:1730	2211:2429 , 2398:3034

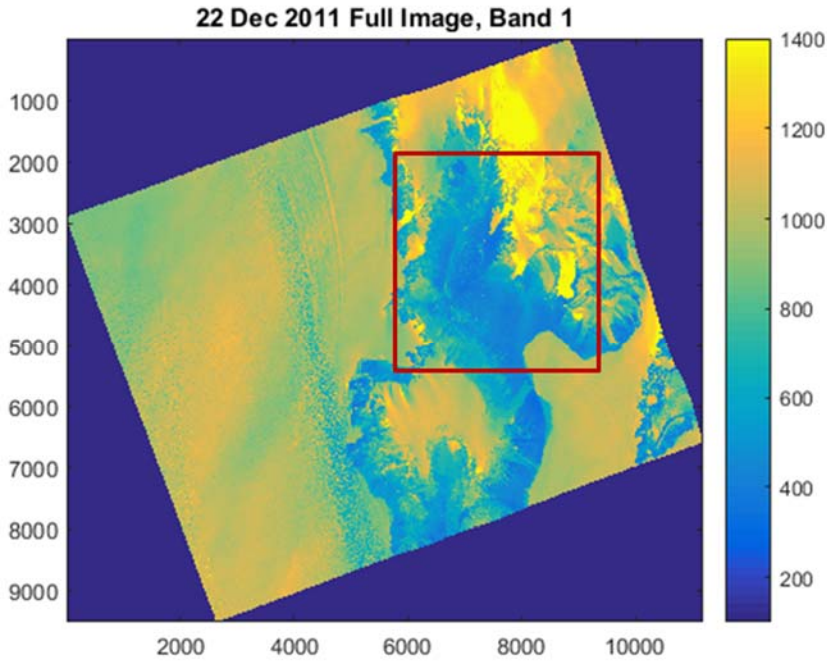


Figure 9: 22 Dec. 2011 Band 1 full image with image chip outlined (red box). Coordinate values are pixel number relative to full image origin. Color indicates intensity of signal, in digital number counts.

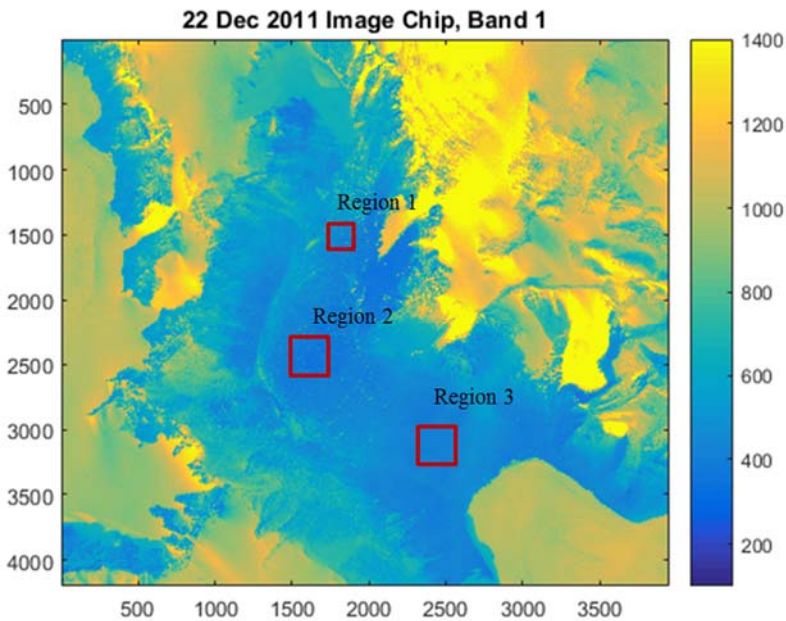
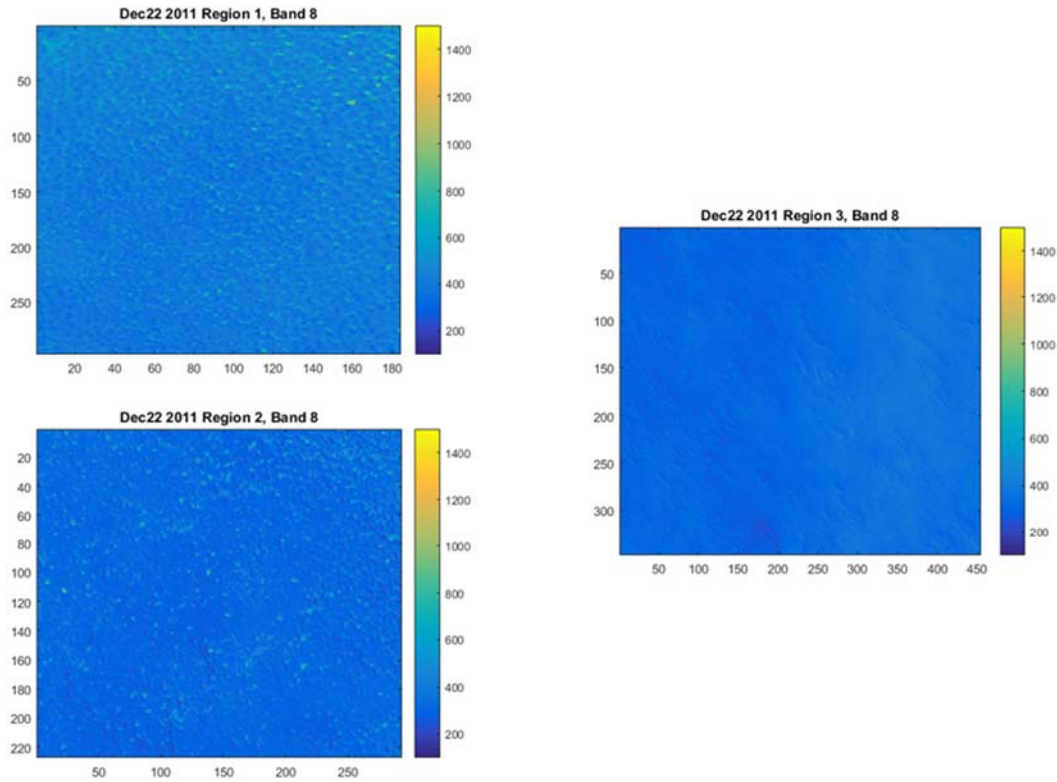


Figure 10: 22 Dec 2011 Band 1 image chip with sub-images for each Region outlined (red boxes). Coordinate values are pixel number relative to image chip origin. Color indicates intensity of signal, in digital number counts.



**Figure 11: 22 Dec 2011 Sub-Images from Figure 13. Coordinate values are pixel number relative to sub-image origin. Color indicates intensity of signal, in digital number counts.**

### Ground Truth Data

As mentioned previously in this paper, the ground truth used in this analysis consists of independently determined ages for each of the three drift regions of the Ong Valley. These ages were determined by measuring the cosmogenic isotope concentrations from rock samples collected at each of the three drift regions of the Ong Valley.

Cosmogenic isotopes are created when material such as rock is exposed to high-energy cosmic rays on the Earth’s surface, as they are after a glacier retreats and leaves behind the accumulated rock plucked from the glacier’s bed during its advance. These cosmic rays occasionally hit the nucleus of an atom in the rocks and expel either a neutron or proton from it, creating an isotope that is otherwise rare in nature. Since the incidence of cosmic rays is well

characterized, the amount of cosmogenic nuclides is directly proportional to the amount of time the rock has been exposed on the surface. Bibby, *et al.* (2016) determined the rate at which cosmogenic nuclides would have been produced in the Ong Valley, correcting the standard production rate for altitude, latitude and the shielding from the valley walls.

Bibby, *et al.* collected both surface and subsurface sediment samples from the middle of each drift region to minimize contamination from rock fall from the valley walls. These samples were collected at two locations within 10m of each other in each region to determine reproducibility of the results. Quartz from each of the samples was assessed via mass spectrometry to determine its  $^{10}\text{Be}$  or  $^{26}\text{Al}$  content. Additional samples from one location per region were assessed for  $^{21}\text{Ne}$  content. By looking at the change in isotope content with depth, the team was able to determine that no significant vertical mixing has occurred in the three drift regions. Additionally, from the  $^{10}\text{Be}/^9\text{Be}$  and  $^{27}\text{Al}/^{26}\text{Al}$  isotope ratios the team was able to estimate the sublimation and erosion rates of the drifts.

For the youngest drift, the subsurface  $^{21}\text{Ne}$  content was not significantly different from the surface  $^{21}\text{Ne}$  content, suggesting a young drift and also providing information on the amount of initial  $^{21}\text{Ne}$  content from prior exposure. Based on  $^{10}\text{Be}/^9\text{Be}$  and  $^{27}\text{Al}/^{26}\text{Al}$  isotope ratios, the youngest drift was determined to be 11–13 ka old. For the middle and oldest drifts, the  $^{10}\text{Be}/^9\text{Be}$  and  $^{27}\text{Al}/^{26}\text{Al}$  ratios were approaching their steady state values, thus becoming less reliable for dating. However, these regions show decreasing  $^{21}\text{Ne}$  content with depth, which allows for a better estimate of the ages than the  $^{10}\text{Be}$  and  $^{27}\text{Al}$  ratios alone allow for. Using the surface  $^{21}\text{Ne}$  content of the middle and oldest regions along with an initial  $^{21}\text{Ne}$  content based on the youngest drift data, the middle drift was determined to be at least 1.1 Ma and likely greater than 1.78 Ma, while the oldest drift was determined to be 1.56 Ma and likely older than 2.63 Ma.



## ANALYSIS AND RESULTS

This section details the analysis performed on the Ong Valley image data and also shows the results of the analysis. Initially a principal component analysis was performed in an attempt to determine a way to differentiate the three drift regions in the image data. That analysis proved to be ineffective, and so another method, based on an empirical, qualitative study of the data, was performed.

### **Analysis: PCA**

The goal of this project is to determine whether remote sensing data can be used to differentiate glacier drifts of different ages. To that end, the sub-image pixel data from each of the three drift regions was processed using a Principal Component Analysis (PCA) technique. PCA is a mathematical method to reduce a potentially-correlated multivariable data set to its uncorrelated components. As this reduction is done starting with the component exhibiting the most variability in the set, it provides for a way to characterize members of a data set based on fewer, potentially many fewer, variables than exist in the source data set. Furthermore, the component coefficients produced by PCA indicate the degree to which each variable contributes to the variation.

As a simple example, suppose one wanted to determine by mass whether fat, carbohydrates or protein contributed the most to the calorie content of food. Given known total calorie content of a variety of foods along with their relative fat, carbohydrate and protein content and the total mass of each food item, a PCA could be performed on this data. It would show that fat contributes about twice as much to total calorie content per gram as fiber and carbohydrates.

Specifically, the PCA component 1 coefficient for fat should be approximately twice the value as the coefficients for carbohydrates and protein.

As with the simple example above, PCA analysis on the sub-image data set should provide a method to characterize the image data into three distinct sets, each one corresponding to a different drift region and therefore different age. The relative values of the components should indicate which bands contribute most to the differences between regions and can be used to inform what linear combination of bands may be most effective in differentiating the three regions. Although PCA is a complex statistical analysis method, MATLAB provides a pre-made PCA function that eliminates the need for developing code to perform the analysis method. This MATLAB function was used in conjunction with the sub-image pixel data to produce PCA results, as detailed below.

The steps taken in this analysis are as follows:

1. For each image data set, extract out sub-image data from each band. This will be three  $n$  by  $m$  arrays of pixels, one for each drift region, and one set of three for each band in the image data set. The result is 24 sub-images for each image data set. Note that  $n$  and  $m$ , the number of rows and columns, may differ for each region within an image set but will be the same for each sub-image taken from the same region. In other words, if Region 1 sub-image is  $300 \times 350$ , then that will be the array size for each of the sub-images for that region in all 8 bands.
2. Determine the mean for each sub-image. This will produce a  $3 \times 8$  matrix of image means for each image data set. Standard deviation will also be calculated.

3. Aggregate the means from all image sets into an overall 3 x 8 matrix that is a mean of means. This is what will be input into the PCA algorithm.
4. Assess the results of the PCA algorithm to determine the best way to combine the band values to differentiate the three regions in the image data.

As mentioned in the previous section, to minimize processing time and memory usage, image chips containing just the Ong Valley were extracted from the full image data sets and processing was done on these image chips. Two assumptions were made about the data sets used in this analysis: 1. Any count value differences due to shaded regions in the valley would be removed during the normalization process of the PCA function, i.e. – shade changes count values equally across all bands. 2. The valley floor is flat enough to not require correction for slope in the data.

Before the analysis can begin, the sub-images need to be extracted from the image chips and the mean and standard deviation for each one needs to be computed. A MATLAB script was written to extract out the sub-image pixels for each band of each data set, determine the means and standard deviation of those sub-images and then form the aggregate means into a table. This resulted in an eight by three matrix, one element for each of the eight bands and each of the three sub-image means, which is input into the PCA function in MATLAB. The MATLAB script is listed in Appendix A. Table 3 shows the resulting aggregate means from this script. Appendix C contains tables for each image set's mean and standard deviation. An aggregate table of standard deviations was not produced.

**Table 3: Sub-Image Aggregate Means for Each Band, as Input to PCA Function**

	Band 1	Band 2	Band 3	Band 4	Band 5	Band 6	Band 7	Band 8
Region 1 Mean	285.24	324.11	359.71	195.99	298.41	174.61	289.94	154.46
Region 2 Mean	265.03	307.27	361.63	209.13	334.18	203.55	361.18	195.72
Region 3 Mean	274.63	322.89	380.34	210.36	324.64	190.95	327.97	174.60

To perform the PCA calculation in MATLAB, the values from Table 3, called `tbl_mean`, are entered as follows:

```
[coeff score, latent, tsquared, explained] = pca(tbl_mean);
```

The primary result is *coeff*, an eight by eight matrix of coefficient values, with the first column of eight values corresponding to the coefficients that map the data onto the component vector that most differentiates the data. An additional part of the output provided by the PCA function is the PCA score *explained*, which is a metric for how much of the variation among the three bands is accounted for by each column vector of coefficients. Once the component coefficients are determined from the data set, these coefficients can then be applied to the original data or other data to assess -- both visually and with the use of metrics -- the success of coefficients in differentiating the regions. Table 4 contains the coefficient results from the PCA.

**Table 4: PCA Coefficient Results from Table 3 Input**

Band Coefficient	PC 1	PC 2	PC 3	PC 4	PC 5	PC 6	PC 7	PC 8
1	-0.2040	0.0293	0.0000	0.0000	0.0000	0.0000	0.0000	0.0000
2	-0.1640	0.3494	0.0000	0.0000	0.0000	0.0000	0.0000	0.0000
3	0.0349	0.8339	0.0000	0.0000	0.0000	0.0000	0.0000	0.0000
4	0.1386	0.2995	0.0000	0.0000	0.0000	0.0000	0.0000	0.0000
5	0.3670	0.2656	0.0000	0.0000	0.0000	0.0000	0.0000	0.0000
6	0.2931	0.0067	0.0000	0.0000	0.0000	0.0000	0.0000	0.0000
7	0.7197	-0.0763	0.0000	0.0000	0.0000	0.0000	0.0000	0.0000
8	0.4153	-0.1249	0.0000	0.0000	0.0000	0.0000	0.0000	0.0000

With the following scores:

1<sup>st</sup> component: 93.07 %

2<sup>nd</sup> component: 6.93 %

These results indicate the following:

1. The variation in the data set is completely accounted for by the first two Principal components.
2. The vast majority – 93% – is accounted for in the first component. As with the Pope and Rees analysis (Pope and Rees, 2014) this is likely variation due to broadband albedo of the surface and may not be the most useful set of coefficients to use to differentiate the regions since it reflects albedo differences rather than spectral differences in the image data.

3. Within that first component, Band 7 is the most influential variable, although all bands contribute to a significant degree. There is anti-correlation between Bands 1 and 2 versus Bands 3 through 8.
4. Within the second component, Band 3 contributes the most to the differences between regions although most other bands contribute to a significant degree. There is anti-correlation between Bands 7 and 8 versus Bands 1 through 6.

A common analysis technique used to interpret PCA results is to plot the first two component coefficient values and observe any clustering. Figure 12 is the resulting plot for the coefficient values in Table 4. No discernable clustering can be identified in the plot.

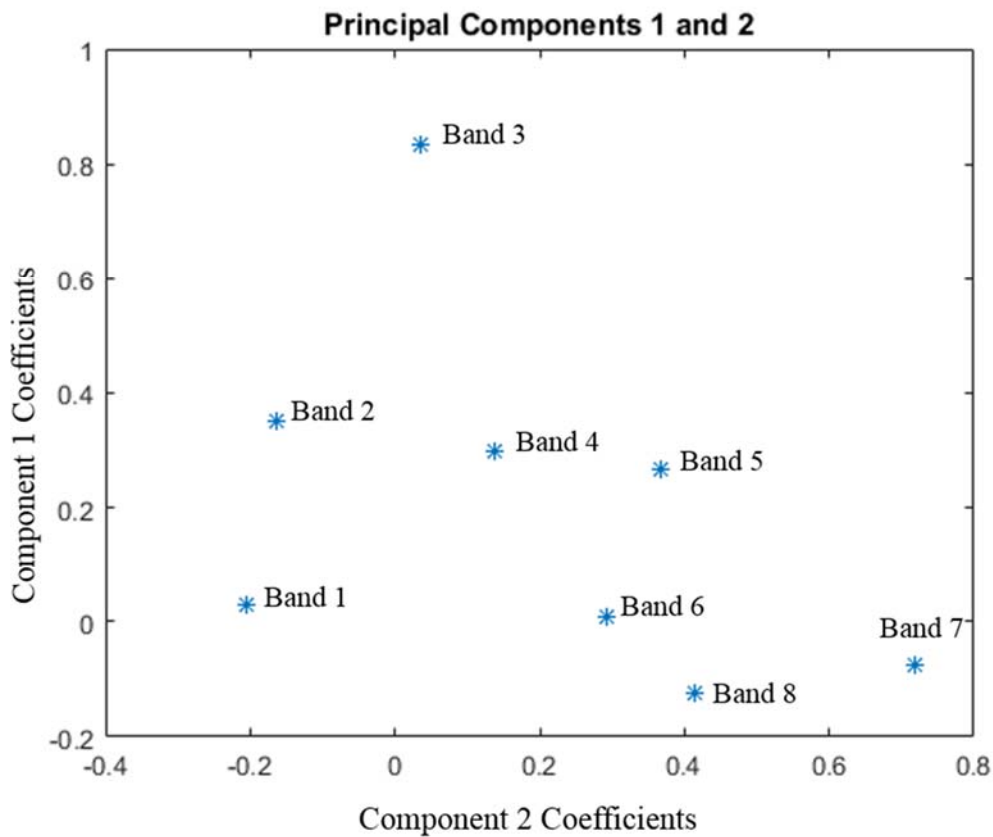


**Figure 12: Principal components plot from Table 4**

Since data from most of the spectral bands contribute a significant degree to the differences between drift regions, based on their coefficients, a simple linear combination of a small number of band to differentiate the regions does not seem apparent. Furthermore, since the component coefficient plot did not reveal any obvious clustering of coefficient pair data, differentiating bands or groups of bands from others which could be exploited to differentiate the regions, these PCA results are not easily interpreted as a straightforward linear combination of band data.

Given that the initial attempt at a PCA analysis didn't produce clearly usable results, a closer look at the data was warranted to determine if variation among the data could be due to factors not directly related to the differences of interest in this analysis. When comparing the tables of means and standard deviations in Appendix C, it is clear that the image data sets fall into two categories, one in which Region 1 image data is shaded and one in which Region 1 image data is not shaded. For example, see the Image Chip for 25 Jan 2014 (unshaded) versus the Image Chip for 13 Dec 2013 (shaded) in the Appendix B. Figures 15 and 16 illustrate this difference. Each plot is the mean count value for each region plotted for each band. Error bars are the standard deviations of the mean values. It is clear that whereas Region 2 and Region 3 data are similar between the two plots, Region 1 data is dissimilar. Because all image set means were aggregated together for PCA input, this difference is likely muddying the analysis results. To address this issue, a second PCA was performed, this time using only data from image sets that do not contain shaded Region 1 data.

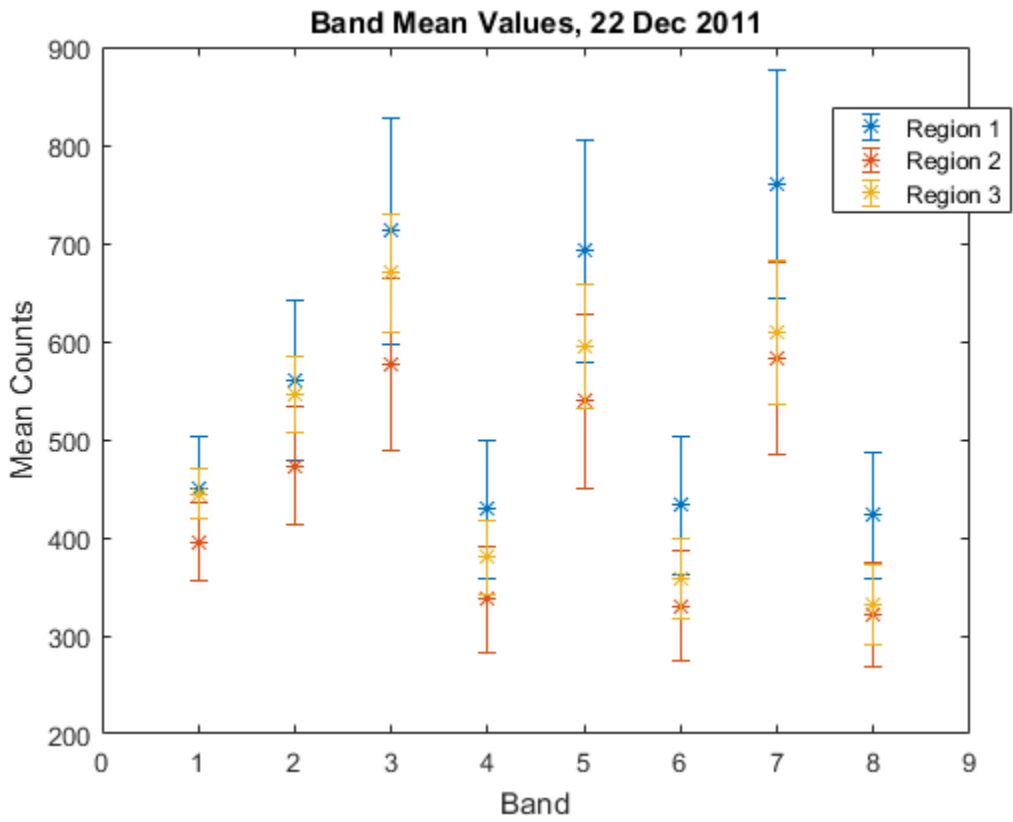
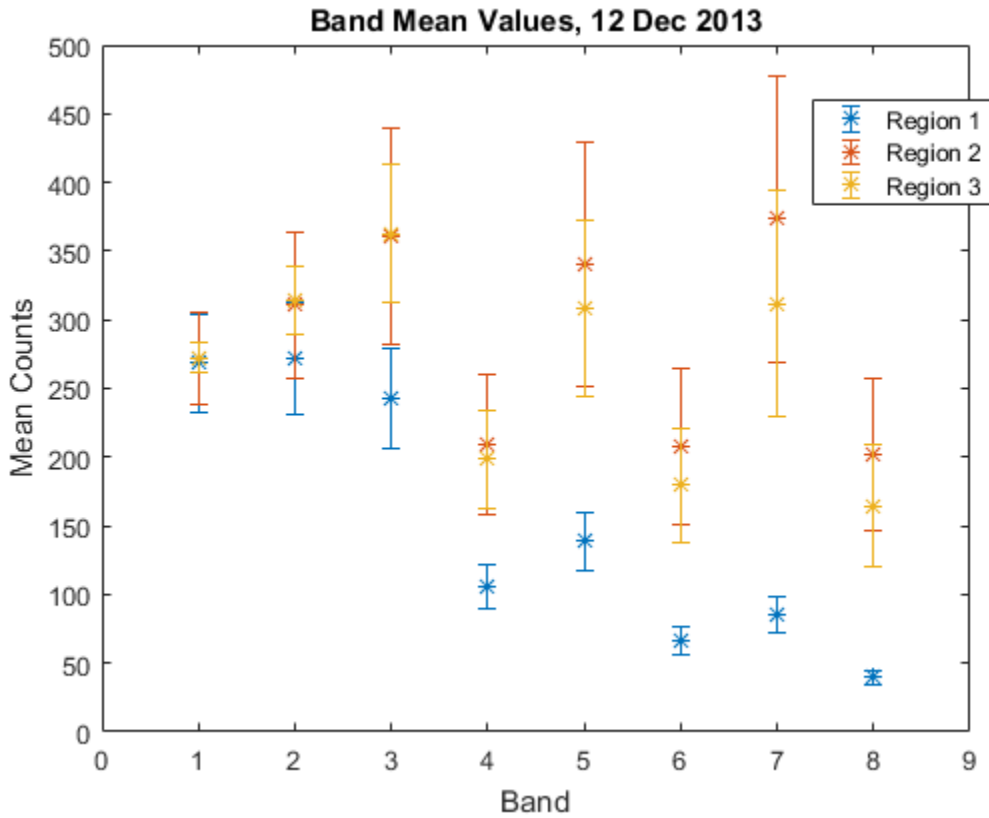


Figure 13: Plot of Mean Counts with 1 Sigma Error Bars, 22 Dec. 2011 Data





**Figure 14: Plot of Mean Counts with 1 Sigma Error Bars, 12 Dec. 2013 Data**

Table 5 contains the aggregate sub-image means for just the non-shaded data.

**Table 5: Sub-Image Means for Each Band using only Shadow-Free Image Sets, as Input to PCA Function**

	Band 1	Band 2	Band 3	Band 4	Band 5	Band 6	Band 7	Band 8
Region 1 Mean	384.64	484.98	628.39	384.07	626.83	390.52	694.34	381.07
Region 2 Mean	323.36	382.61	464.72	273.61	439.98	270.12	481.94	264.66
Region 3 Mean	349.97	423.39	516.37	292.05	456.28	272.23	469.31	253.82

The data in Table 5 produces the following PCA results.

**Table 6: PCA Coefficient Results from Table 5 Input (Non-Shaded Data Sets)**

Band Coefficient	PC 1	PC 2	PC 3	PC 4	PC 5	PC 6	PC 7	PC 8
1	0.12893	0.32171	0.0000	0.0000	0.0000	0.0000	0.0000	0.0000
2	0.21951	0.48234	0.0000	0.0000	0.0000	0.0000	0.0000	0.0000
3	0.36616	0.56770	0.0000	0.0000	0.0000	0.0000	0.0000	0.0000
4	0.26559	0.13658	0.0000	0.0000	0.0000	0.0000	0.0000	0.0000
5	0.46600	0.00728	0.0000	0.0000	0.0000	0.0000	0.0000	0.0000
6	0.30971	-0.12141	0.0000	0.0000	0.0000	0.0000	0.0000	0.0000
7	0.56475	-0.45985	0.0000	0.0000	0.0000	0.0000	0.0000	0.0000
8	0.31393	-0.31089	0.0000	0.0000	0.0000	0.0000	0.0000	0.0000

With the following scores:

1<sup>st</sup> component: 97.62 %

2<sup>nd</sup> component: 2.38 %

These results indicate the following:

1. The variation in the data set is completely accounted for by the first two Principal components.
2. The vast majority – 98% – is accounted for in the first component. As with the Pope and Rees analysis (Pope and Rees, 2014) this is likely variation due to broadband albedo of the surface and may not be the most useful set of coefficients to use to differentiate the

regions since it reflects albedo differences rather than spectral differences in the image data.

3. Within that first component, Band 7 is the most influential variable, although all bands contribute to a significant degree. Unlike the initial PCA results, there is no anti-correlation in this set of coefficients.
4. Within the second component, Band 3 contributes the most to the differences between regions although most other bands contribute to a significant degree. There is anti-correlation between Bands 6, 7 and 8 versus Bands 1 through 5.

As with the previous PCA results, the two component coefficients were plotted to find clustering in the data. Figure 15 is the resulting plot for the coefficient values in Table 6. No discernable clustering can be identified in the plot.

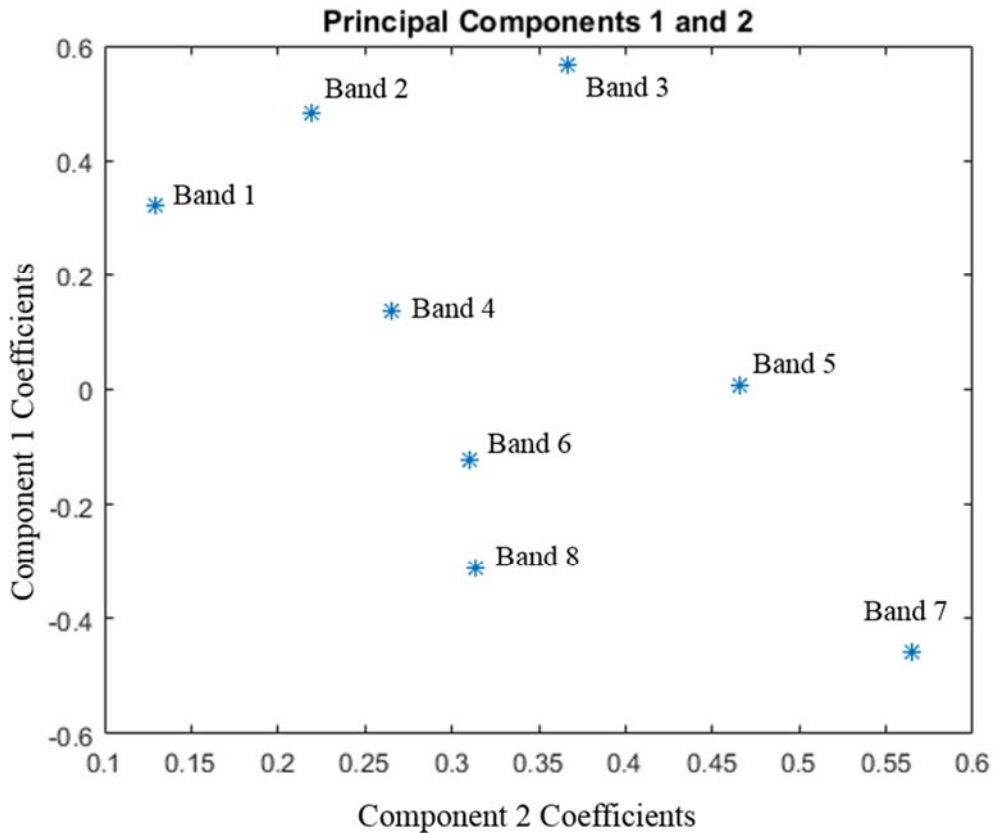


**Figure 15: Principal components plot from Table 6**

As with the previous PCA results, since data from most spectral bands contribute a significant degree to the differences between drift regions, based on their coefficients, a simple linear combination of a small number of band to differentiate the regions does not seem apparent. Furthermore, since the component coefficient plot did not reveal any obvious clustering of coefficient pair data, differentiating bands or groups of bands from others which could be exploited to differentiate the regions, these PCA results are not easily interpreted as a straightforward linear combination of band data.

### **Analysis: Empirical**

Because the PCA analysis did not provide a clear linear combination of band values to differentiate the drift regions, a follow-on empirical analysis was attempted. When working with

the data, it was noted that there are characteristic difference in the band relationships between each of the three regions, particularly which region has a maximum value and which has a minimum value within each band set. The table below illustrates the point. It is the same data as in Table 3 with an additional column for standard deviation. Cells in green are the maximum of the data set within a band, cells in orange are the minimum. It is clear that bands 1 and 2, bands 3 and 4 and bands 5 through 8 behave differently in terms of which sub-image region has the maximum and minimum values.

**Table 7: Sub-Image Means for Each Band, Color-Coded by Max, Min with Standard Deviation (green = band maximum, orange = band minimum)**

	Band 1	Band 2	Band 3	Band 4	Band 5	Band 6	Band 7	Band 8
Region 1 Mean	285.24	324.11	359.71	195.99	298.41	174.61	289.94	154.46
Region 2 Mean	265.03	307.27	361.63	209.13	334.18	203.55	361.18	195.72
Region 3 Mean	274.63	322.89	380.34	210.36	324.64	190.95	327.97	174.60
Std Dev	10.11	9.39	11.40	7.97	18.52	14.51	35.65	20.63

At first glance, this pattern of maximum and minimum values within a region could be used to develop an empirical method to differentiate the three regions. A mathematical combination of values from three different bands, with one set of data from each of the three band sets that behaves similarly, e.g. – values from either Band 1 or Band 2, combined with values from either Band 3 or Band 4, combined with any value from Bands 5 -8 should best maximize the differences. This is analogous to band ratios values like those calculated for determining glacial areas, as mentioned in the several papers in the Literature Review section of this document. However, as mentioned previously, when looking more closely at the data, specifically at the

means for each of the six data sets that were incorporated into the values for Table 7, it is clear that the above pattern of maximum and minimum values is the result of the averaging and does not hold true for each of the data sets individually. Instead the data sets fall into one of two maximum/minimum patterns, as shown in Tables 8 and 9, based on whether Region 1 is shaded or not. Note that to minimize the effects of different illumination levels, the mean values in these tables are normalized by the sum of the mean values for the region, i.e. – each band’s mean count value was divided by the sum of the count values for all 8 bands of that region. Two of the six sub-image mean tables follow Pattern 1 and four follow Pattern 2. Looking at the image chip figures (see Appendix B, e.g. - Image Chip for 25 Jan 2014 (unshaded) versus the Image Chip for 13 Dec 2013 (shaded)) it appears that the pattern, as mentioned before, has to do with whether Region 1 is shaded or not. Based on this observation, it would seem that the unshaded data should be used to derive the empirical formula so that

**Table 8: Example Pattern 1 Normalized Sub-Image Means, Color-Coded by Max, Min with Standard Deviation (green = band maximum, orange = band minimum)**

	Band 1	Band 2	Band 3	Band 4	Band 5	Band 6	Band 7	Band 8
Region 1 Mean (normalized)	0.10073	0.12562	0.15985	0.09620	0.15529	0.09703	0.17047	0.09481
Region 2 Mean (normalized)	0.11126	0.13303	0.16217	0.09469	0.15162	0.09285	0.16388	0.09050
Region 3 Mean (normalized)	0.11298	0.13883	0.17020	0.09653	0.15117	0.09095	0.15490	0.08444
Std Dev	0.00664	0.00662	0.00543	0.00098	0.00226	0.00311	0.00782	0.00521

**Table 9: Example Pattern 2 Normalized Sub-Image Means, Color-Coded by Max, Min with Standard Deviation (green = band maximum, orange = band minimum)**

	Band 1	Band 2	Band 3	Band 4	Band 5	Band 6	Band 7	Band 8
Region 1 Mean (normalized)	0.21995	0.22308	0.19891	0.08696	0.11395	0.05438	0.07034	0.03244
Region 2 Mean (normalized)	0.11941	0.13652	0.15840	0.09188	0.14965	0.09133	0.16399	0.08883
Region 3 Mean (normalized)	0.12903	0.14884	0.17172	0.09392	0.14606	0.08502	0.14763	0.07779
Std Dev	0.05548	0.04683	0.02065	0.00358	0.01965	0.01977	0.05002	0.02989

all regions' data sets are comparable. However, the results may not work to differentiate regions in an image that contains shaded parts of the valley. Figure 13 is also informative in helping choose which bands to include in the band ratio. Ideally, the count value sets for the selected bands should be as far apart as possible from each other but should also be separated by greater than their standard deviations, otherwise noise in the data will potentially nullify the separation method. To help clarify the band selection choices, the normalized mean count values were plotted for one of the data image sets (Figure 16).

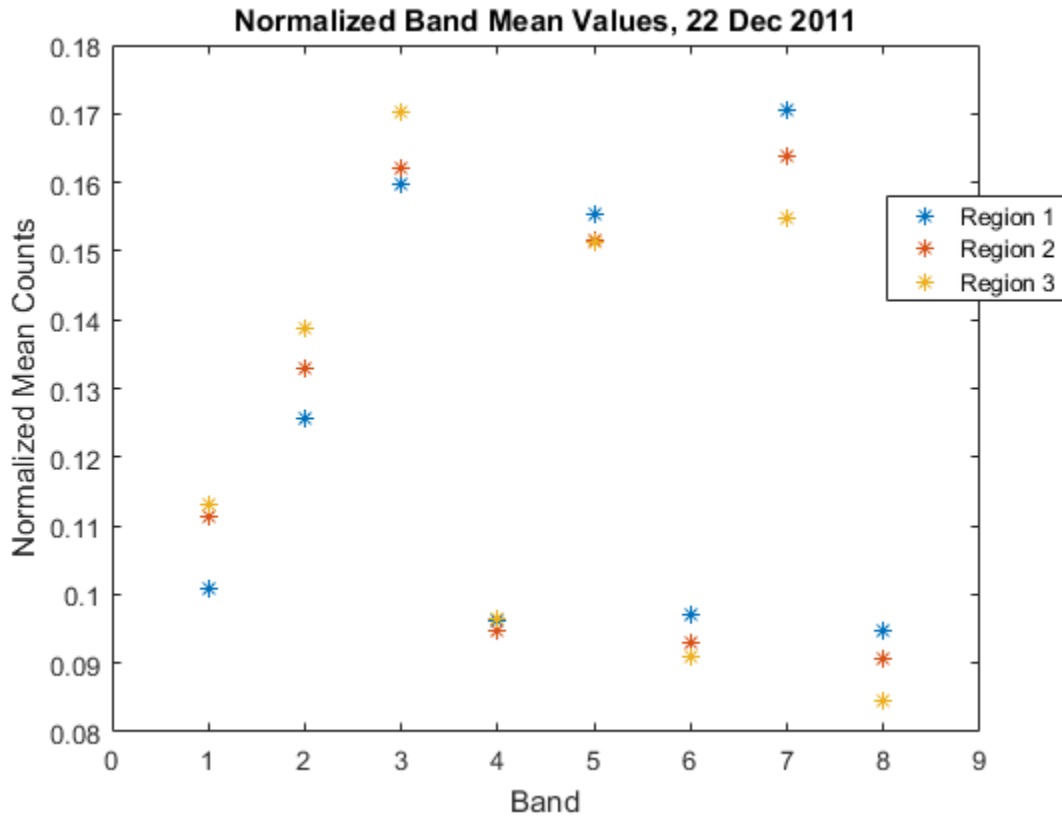


**Figure 16: Normalized Mean Count Values, 22 Dec. 11 data**

The band selection criteria are therefore the following:

1. Choose bands that have different max/min relationships for each of two or three regions
2. Among the possible choices that satisfy condition 1, choose bands whose three mean count value standard deviations minimally overlap (Figure 13)
3. Among the possible choices that satisfy condition 2, choose bands with the largest normalized standard deviations (Table 7) or, comparably, data spread within a band (Figure 17)



Based on those considerations and using commonly developed methods of band combinations, such as for NDVI, the following formula was developed as Normalized Drift Index:

$$\text{Normalized Drift Index (NDI)} = \frac{\text{Normalized Band 7} - \text{Normalized Band 2}}{\text{Normalized Band 7} + \text{Normalized Band 2}}$$

where, as with NDVI, each band value is first normalized by the total count value in all bands before use in the calculation. This allows for an analysis that is independent of the relative signal intensity between bands and in relative signal differences between other data sets. Tables 10 and 11 show the normalized values used for the analysis as well as the resulting NDI value for each of the two image sets.

**Table 10: Normalized Band Values Used for Differentiation of Drift Regions 22 Dec. 2011**

	Band 2	Band 7	Result
Region 1	0.12562	0.17047	0.151474
Region 2	0.13303	0.16388	0.103904
Region 3	0.13883	0.1549	0.05471

**Table 11: Normalized Band Values Used for Differentiation of Drift Regions 25 Jan. 2014**

	Band 2	Band 7	Result
Region 1	0.11741	0.18006	0.21061
Region 2	0.13008	0.16970	0.13216
Region 3	0.14095	0.15436	0.04541

The resulting NDI values in the tables show that a similar relationship holds for each of the two image data sets, namely that NDI values are highest for Region 1 and lowest for Region 3. From this, as with NDVI, a range of values could be established for each Region, indicating that if a pixel's NDI value falls within that range, it is of that Region type, i.e. – drift age. However, while the relative assessment of highest and lowest NDI values holds, it is worrying that the values themselves differ between data sets. For example, the Region 2 NDI value from the 25 Jan. data is close to both the Region 1 and Region 2 value from the 22 Dec. data. Depending on how much these values vary over the image region in question, it may be difficult to find value ranges that unambiguously determine that a pixel, based on its NDI, belongs to one of the three Regions.

To assess how effective these NDI values might be in determining which Region a pixel belongs to, the NDI method was applied to image data. This method to differentiate pixels based on regions should work best on the data sets used to generate the NDI values. To that end, a MATLAB script was written that takes each sub-image from the 22 Dec. data image set, normalizes each pixel of each of the three sub-images by the sum of the count values for that pixel in all bands and then calculates the NDI as listed above. The following figures are the result. Note that the color scale is the same for all three images.

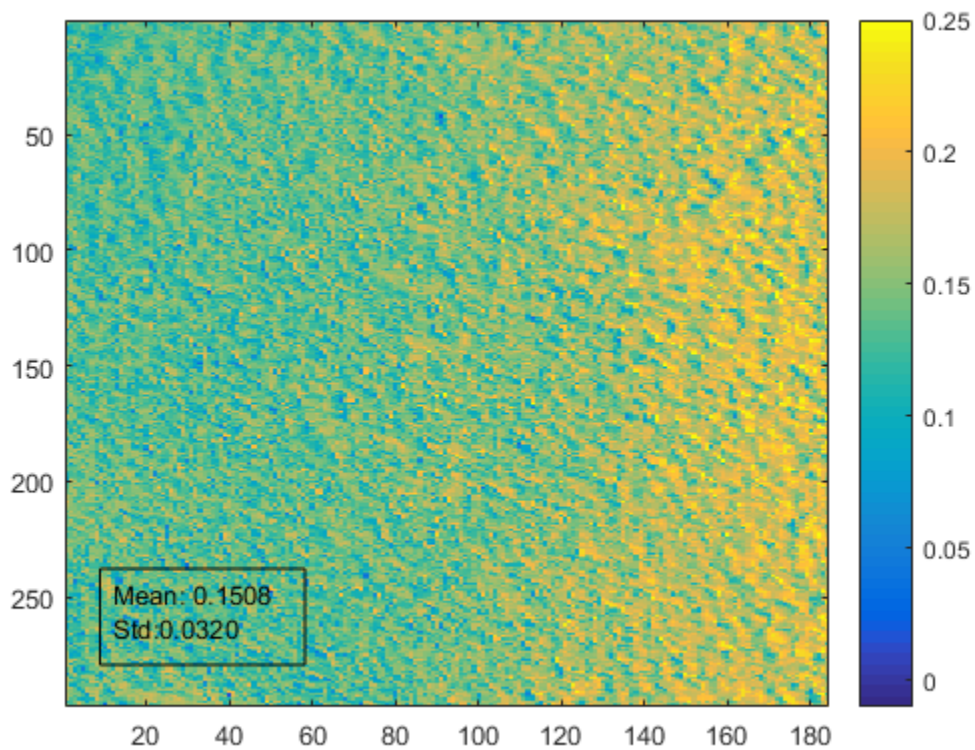


**Figure 17: Region 1 Sub-Image NDI, 22 Dec. 2011 Data. Coordinate values are pixel number relative to sub-image origin. Color indicates Normalized Drift Index (NDI) value.**

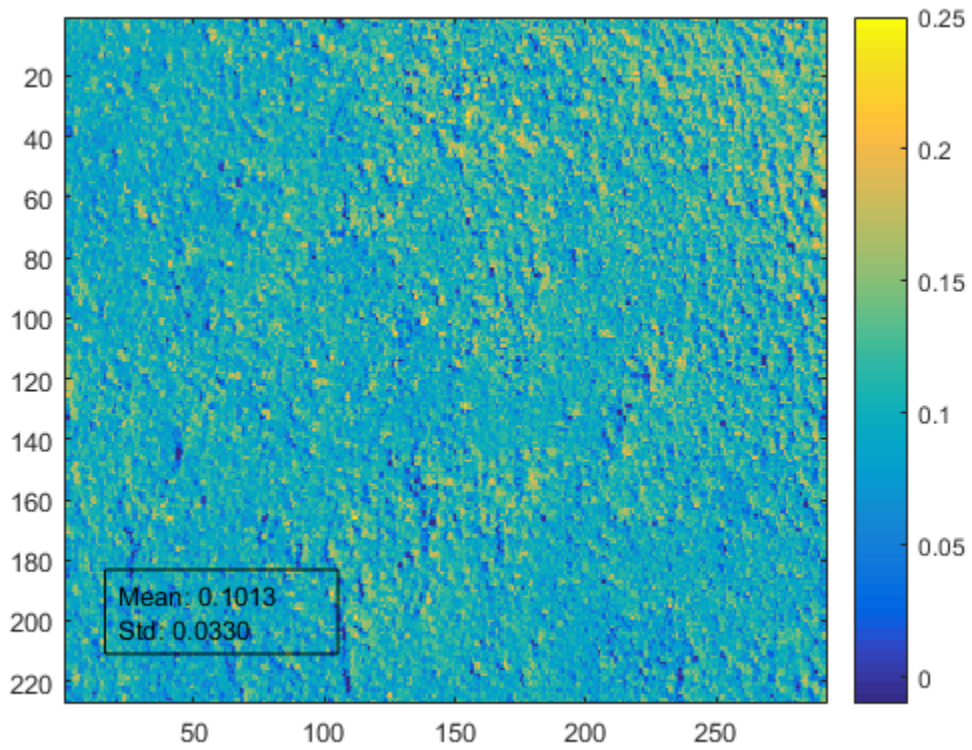


**Figure 18: Region 2 Sub-Image NDI, 22 Dec. 2011 Data. Coordinate values are pixel number relative to sub-image origin. Color indicates Normalized Drift Index (NDI) value.**

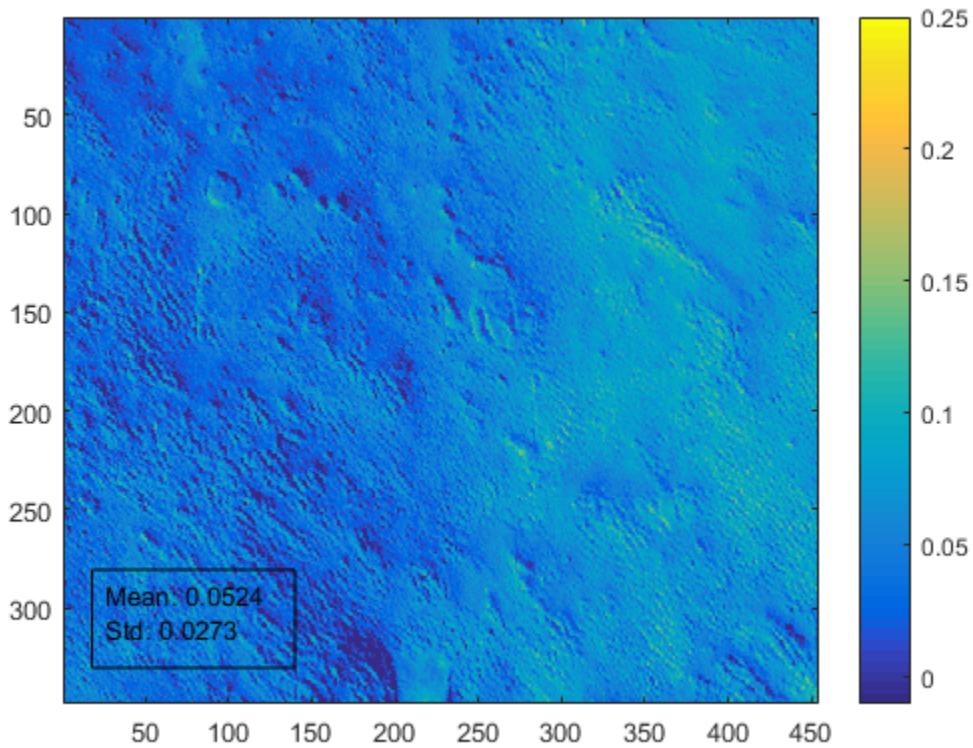


**Figure 19: Region 3 Sub-Image NDI, 22 Dec 2011 Data. Coordinate values are pixel number relative to sub-image origin. Color indicates Normalized Drift Index (NDI) value.**

A similar analysis was done for the 25 Jan. 2014 data with the following figures as a result.

Note that the color scale is the same for all three images but different from the color scale for the 22 Dec data.

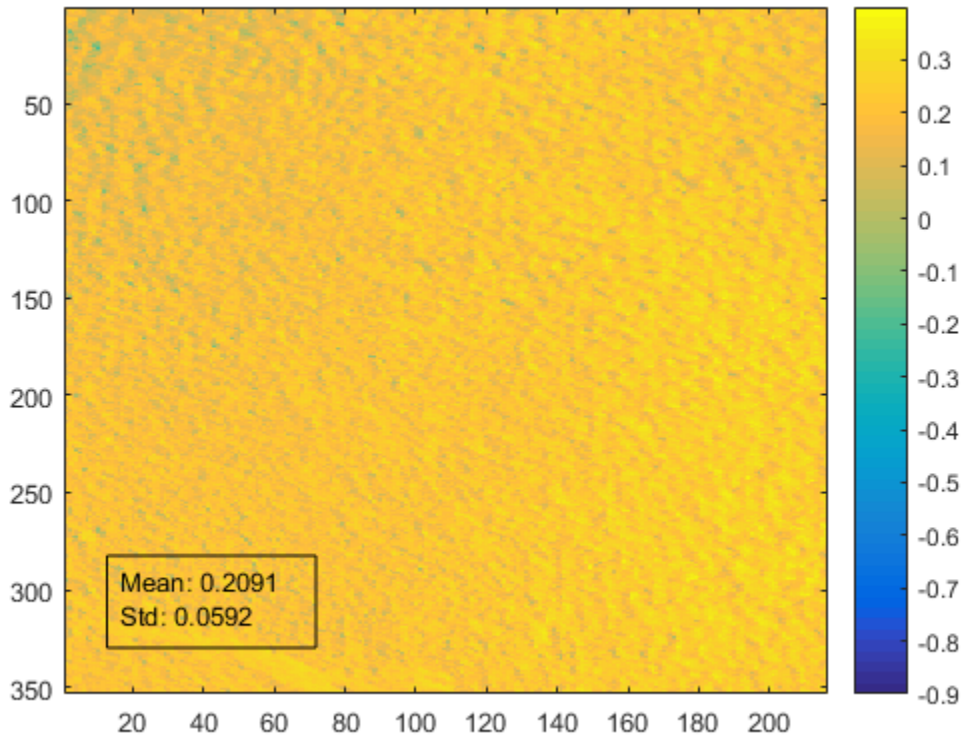


**Figure 20: Region 1 Sub-Image NDI, 25 Jan. 2014 Data. Coordinate values are pixel number relative to sub-image origin. Color indicates Normalized Drift Index (NDI) value.**

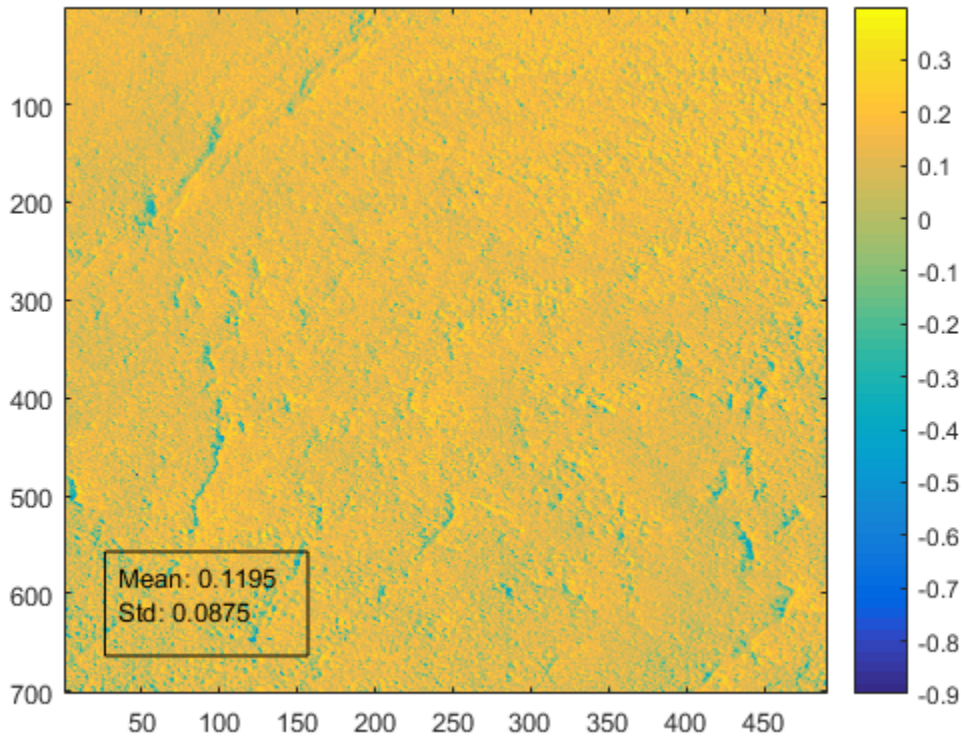


**Figure 21: Region 2 Sub-Image NDI, 25 Jan. 2014 Data. Coordinate values are pixel number relative to sub-image origin. Color indicates Normalized Drift Index (NDI) value.**

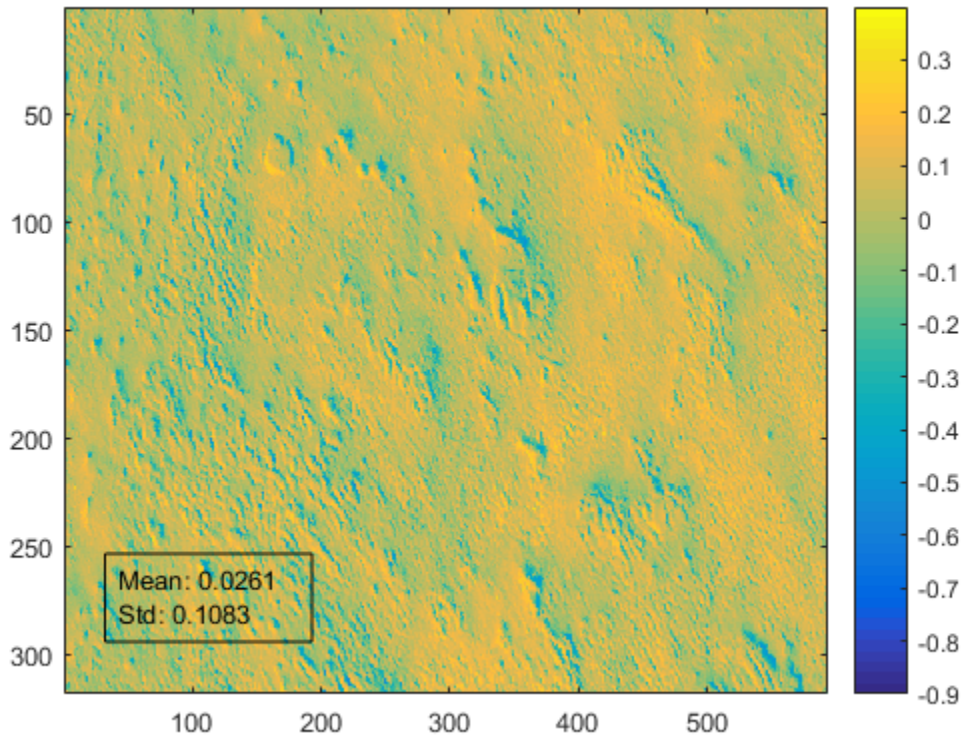


**Figure 22: Region 3 Sub-Image NDI, 25 Jan. 2014 Data. Coordinate values are pixel number relative to sub-image origin. Color indicates Normalized Drift Index (NDI) value.**

It is clear from the images, both visually and when their means and standard deviations are considering that the data within a sub-image have too wide of a count value range to characterize the regions accurately using their NDI values. In other words, the standard deviation within a sub-image and the mean count value differences between image sets for the same region produce greater differences than the NDI method is able to produce between different regions. Given that these data sets represent the best case scenario for applying this method it is apparent that the developed NDI is not sufficient to characterize drift regions based on the remote sense data as used in this analysis.



## CONCLUSION

Knowing the ages of glacier drifts in Antarctica would help map out changes in the paleoclimate and give researchers a better understanding of how Earth's climate has changed over the last several million years. The ability to determine the age of glacier drifts in Antarctica via remote sensing would be a great asset to these researchers as it would eliminate the need to visit these remote areas to collect samples for laboratory analysis.

The analysis behind this thesis was an attempt to find out how to use remote sensing data to determine drift ages for the three drifts of the Ong Valley, whose ages are known from sample collection and laboratory analysis. The remote sensing data set used in this analysis was 8 band multispectral image level 1B data from WorldView-2 and WorldView-3 collected between 2010 and 2015. Sub-image means for each of the drift regions and all 8 bands were used in the analysis of this project. Both Principal Component Analysis and an empirical analysis of the remote sensing image data were performed.

The PCA analysis showed that all of the variation within the data set is captured in two principal components. The coefficients for first component were all within the same order of magnitude and all but one of the coefficients for the second component were likewise all within the same order of magnitude. Therefore the PCA results suggest that all bands contribute roughly the same to the differences between the regions. Furthermore, the coefficients pairs do not cluster in a way to indicate that particular bands or groups of bands exhibit properties different from other groups which could be exploited to differentiate the regions. These results suggest that a linear combination of a small subset of band data would not be sufficient to differentiate the drift regions for classification as different ages.

Nevertheless, an empirical analysis was performed as well. This analysis was based on observed trends in the data, i.e. - which normalized count values within a band are a maximum and which are a minimum for each region. From this data trend a drift index was developed, a combination of data from bands 2 and 7. This index was then applied to the image data to assess whether the three drift regions exhibit index values in distinct and separate ranges. While these index results showed statistically significant differences between regions 1 and 3 within an image data set region 2 was not statistically different from the other regions. Furthermore drift index values for the same region between image data sets were not quantitatively comparable, i.e. – index values from region 1 were higher than values from regions 2 and 3 within their respective data sets but index values from region 1 in one image data set were closer to index values from region 2 in the other image data set. Therefore this developed index could potentially be used to qualitatively differentiate drift regions by age, with higher index values corresponding to older drifts but does not seem sufficient to quantitatively differentiate between drifts of different ages. A qualitative differentiation of drift regions is likely to be of limited use to paleoclimatologists and therefore further work in this area is recommended.

This analysis did not cover all possible ways to assess and use the available data, and thus future research may provide a solution. Just the literature review in this document, which is by no means a complete summary of the research to date, indicates several potential avenues to explore for this problem. To begin with, little preprocessing was done on the data used – just radiometric correction and sensor correction. Perhaps geometric correction or noise removal would produce a more compatible set of images that eliminates much of the variation in the data that prevented a successful NDI criteria test in this project. Furthermore, the only PCA performed for this analysis was the standard version found in MATLAB. Variations on that

function, such as using eigenvalue decomposition or alternating least squares weighted variance instead of the singular value decomposition default, were not explored. And while PCA was used for this analysis, it is only one of several analysis techniques that could be applied to this data set. Finally, as new and better remote sensing technologies become available, new data will likely be collected at better spatial and spectral resolution and in different parts of the EM spectrum, possibly requiring the need for more extensive computing power, such as cloud computing, to analyze larger data set volumes. This new data may yield a solution to dating glacier drifts. Alternatively, following the method used in Pope and Rees (2014) and a similar method used to map surface mineralogy on the south Tamil Nadu coast of India (Chandrasekar, *et al.*, 2011) spectral analysis on collected drift samples from the Ong Valley could be used to inform the image data analysis as to which bands or band combinations would best differentiate the image data into the different drift regions.

## REFERENCES

- Bernard, É., Friedt, J. M., Tolle, F., Griselin, M., Martin, G., Laffly, D., & Marlin, C. (2013). Monitoring seasonal snow dynamics using ground based high resolution photography (Austre Lovénbreen, Svalbard, 79°N). *ISPRS Journal of Photogrammetry and Remote Sensing*, Volume 75, 92-100.
- Bibby, T., Putkonen, J., Morgan, D., Balco, G., & Shuster, D. L. (2016). Million year old ice found under meter thick debris. *Geophysical Research Letters*, 43(13), 6995–7001.
- Bolch, T. (2007). Climate change and glacier retreat in northern Tien Shan (Kazakhstan/Kyrgyzstan) using remote sensing data. *Global and Planetary Change*, Volume 56, Issues 1–2, 1-12.
- Brenning, A. (2009). Benchmarking classifiers to optimally integrate terrain analysis and multispectral remote sensing in automatic rock glacier detection. *Remote Sensing of Environment*, Volume 113, Issue 1, 239-247.
- Chandrasekar, N., Sheikmujabar, P., & Rajamanickam, G. V. (2011). Investigation of heavy-mineral deposits using multispectral satellite data. *International Journal of Remote Sensing*, 8641–8655.
- Confalonieri, U. M. (2007). *Climate Change 2007: Impacts, Adaptation and Vulnerability. Contribution of Working Group II to the Fourth Assessment Report of the Intergovernmental Panel on Climate Change*. Cambridge, UK: Cambridge University Press.

- Dozier, J., & Painter, T. H. (2004). Multispectral and Hyperspectral Remote Sensing of Alpine Snow Properties. *Annual Review Earth Planetary Science*, 32, 465-95.
- Frey, H., Paul, F., & Strozzi, T. (2012). Compilation of a glacier inventory for the western Himalayas from satellite data: methods, challenges, and results. *Remote Sensing of Environment*, Volume 124, 832-843.
- Heid, T., & Kääb, A. (2012). Evaluation of existing image matching methods for deriving glacier surface displacements globally from optical satellite imagery. *Remote Sensing of Environment*, Volume 118, 339-355.
- Jensen, J. R. (2000). *Remote Sensing of the Environment, An Earth Resource Perspective*. Upper Saddle River, NJ: Prentice-Hall, Inc.
- Kargel, J. S., Abrams, M. J., Bishop, M. P., Bush, A., Hamilton, G., Jiskoot, H., . . . Wessels, R. (2005). Multispectral imaging contributions to global land ice measurements from space. *Remote Sensing of Environment*, Volume 99, Issues 1–2, 187-219.
- Karimi, N., Farokhnia, A., Karimi, L., Eftekhari, M., & Ghalkhani, H. (2012). Combining optical and thermal remote sensing data for mapping debris-covered glaciers (Alamkouh Glaciers, Iran). *Cold Regions Science and Technology*, Volume 71, 73-83.
- Koutnik, M. R., Waddington, E. D., & Winebrenner, D. P. (2009). A method to infer past surface mass balance and topography from internal layers in martian polar layered deposits. *Icarus*, Volume 204, Issue 2, 458-470.

- Lee, H., Shum, C. K., Tseng, K.-H., Huang, Z., & Sohn, H.-G. (2013). Elevation changes of Bering Glacier System, Alaska, from 1992 to 2010, observed by satellite radar altimetry. *Remote Sensing of Environment, Volume 132*, 40-48.
- Lemke, P. J. (2007). *Climate Change 2007: The Physical Science Basis. Contribution of Working Group I to the Fourth Assessment Report of the Intergovernmental Panel on Climate Change*. Cambridge, United Kingdom: Cambridge University Press.
- Li, S., Benson, C., Gens, R., & Lingle, C. (2008). Motion patterns of Nabesna Glacier (Alaska) revealed by interferometric SAR techniques. *Remote Sensing of Environment, Volume 112, Issue 9*, 3628-3638.
- Luckman, A., Quincey, D., & Bevan, S. (2007). The potential of satellite radar interferometry and feature tracking for monitoring flow rates of Himalayan glaciers. *Remote Sensing of Environment, Volume 111, Issues 2-3*, 172-181.
- Paul, F., Huggel, C., & Kääb, A. (2004). Combining satellite multispectral image data and a digital elevation model for mapping debris-covered glaciers. *Remote Sensing of Environment, Volume 89, Issue 4*, 510-518.
- Paul, F., Kääb, A., & Haeberli, W. (2007). Recent glacier changes in the Alps observed by satellite: Consequences for future monitoring strategies. *Global and Planetary Change, Volume 56, Issues 1-2*, 111-122.
- Pope, A., & Rees, G. (2014). Using in situ spectra to explore Landsat classification of glacier surfaces. *International Journal of Applied Earth Observation and Geoinformation, Volume 27, Part A*, 42-52.

- Raup, B., Racoviteanu, A., Khals, S. J., Helm, C., & Armstrong, R. (2007). The GLIMS geospatial glacier database: A new tool for studying glacier change. *Global and Planetary Change, Volume 56, Issues 1–2*, 101-110.
- Salvatore, M., Mustard, J., Head, J., Marchant, D., & Wyatt, M. (2014). Characterization of spectral and geochemical variability within the Ferrar Dolerite of the McMurdo Dry Valleys, Antarctica: Weathering, alteration, and magmatic processes. *Antarctic Science*, 49-68.
- Schmidt, F., Schmitt, B., Douté, S., Forget, F., Jian, J.-J., Martin, P., . . . the OMEGA Team. (2010). Sublimation of the Martian CO<sub>2</sub> Seasonal South Polar Cap. *Planetary and Space Science, Volume 58, Issue 10*, 1129-1138.
- Wolken, G. J. (2006). High-resolution multispectral techniques for mapping former Little Ice Age terrestrial ice cover in the Canadian High Arctic. *Remote Sensing of Environment, Volume 101, Issue 1*, 104-114.
- Xiaoming , W. (2011). Beijing-1 Small Satellite System & Its Application. *13th DMC Consortium Meeting*. <http://www.spaceconference.co.uk/dmc13.html>.
- Xie, Y., Sha, Z., & Yu, M. (2008). Remote sensing imagery in vegetation mapping: a review. *Journal of Plant Ecology, 1 Number 1*, 9-23.

## APPENDIX A: MATLAB PROGRAMS

```
% This script opens each image file used in the analysis, extracts out the
% image chip, then determines the mean for each sub-region in the image
% chip
% The result is an 8x3 matrix of where each element is the mean of the
% means of each image's regional mean

clear;
close all;

% 22Dec 2011 data
rawDataFull =
importdata('C:\Users\Paula\Desktop\thesisAnalysis\thesis_data_subset\output\WV02_11DEC22195305_103001001
0AAEE00_11DEC22195305-MIBS-500092642100_01_P003_u16ns3031.tif');
rawData = rawDataFull(1530:5728,5380:9334,:);
% clear the full array so save processing time and memory
clear rawDataFull;

data_11Dec(1,1) = mean(mean(rawData(1414:1710 , 1770:1953,1)));
data_11Dec(1,2) = mean(mean(rawData(2254:2480 , 1565:1856,1)));
data_11Dec(1,3) = mean(mean(rawData(2980:3327 , 2318:2771,1)));
s1 = size(rawData(1414:1710 , 1770:1953,1));
s2 = size(rawData(2254:2480 , 1565:1856,1));
s3 = size(rawData(2980:3327 , 2318:2771,1));
vec1 = reshape(rawData(1414:1710 , 1770:1953,1), s1(1)*s1(2),1);
vec2 = reshape(rawData(2254:2480 , 1565:1856,1), s2(1)*s2(2),1);
vec3 = reshape(rawData(2980:3327 , 2318:2771,1), s3(1)*s3(2),1);
std_11Dec(1,1) = std(double(vec1));
std_11Dec(1,2) = std(double(vec2));
std_11Dec(1,3) = std(double(vec3));

data_11Dec(2,1) = mean(mean(rawData(1414:1710 , 1770:1953,2)));
data_11Dec(2,2) = mean(mean(rawData(2254:2480 , 1565:1856,2)));
data_11Dec(2,3) = mean(mean(rawData(2980:3327 , 2318:2771,2)));
vec1 = reshape(rawData(1414:1710 , 1770:1953,2), s1(1)*s1(2),1);
vec2 = reshape(rawData(2254:2480 , 1565:1856,2), s2(1)*s2(2),1);
vec3 = reshape(rawData(2980:3327 , 2318:2771,2), s3(1)*s3(2),1);
std_11Dec(2,1) = std(double(vec1));
std_11Dec(2,2) = std(double(vec2));
std_11Dec(2,3) = std(double(vec3));

data_11Dec(3,1) = mean(mean(rawData(1414:1710 , 1770:1953,3)));
data_11Dec(3,2) = mean(mean(rawData(2254:2480 , 1565:1856,3)));
data_11Dec(3,3) = mean(mean(rawData(2980:3327 , 2318:2771,3)));
vec1 = reshape(rawData(1414:1710 , 1770:1953,3), s1(1)*s1(2),1);
vec2 = reshape(rawData(2254:2480 , 1565:1856,3), s2(1)*s2(2),1);
vec3 = reshape(rawData(2980:3327 , 2318:2771,3), s3(1)*s3(2),1);
std_11Dec(3,1) = std(double(vec1));
std_11Dec(3,2) = std(double(vec2));
std_11Dec(3,3) = std(double(vec3));
```



```

data_11Dec(4,1) = mean(mean(rawData(1414:1710 , 1770:1953,4)));
data_11Dec(4,2) = mean(mean(rawData(2254:2480 , 1565:1856,4)));
data_11Dec(4,3) = mean(mean(rawData(2980:3327 , 2318:2771,4)));
vec1 = reshape(rawData(1414:1710 , 1770:1953,4), s1(1)*s1(2),1);
vec2 = reshape(rawData(2254:2480 , 1565:1856,4), s2(1)*s2(2),1);
vec3 = reshape(rawData(2980:3327 , 2318:2771,4), s3(1)*s3(2),1);
std_11Dec(4,1) = std(double(vec1));
std_11Dec(4,2) = std(double(vec2));
std_11Dec(4,3) = std(double(vec3));

```

```

data_11Dec(5,1) = mean(mean(rawData(1414:1710 , 1770:1953,5)));
data_11Dec(5,2) = mean(mean(rawData(2254:2480 , 1565:1856,5)));
data_11Dec(5,3) = mean(mean(rawData(2980:3327 , 2318:2771,5)));
vec1 = reshape(rawData(1414:1710 , 1770:1953,5), s1(1)*s1(2),1);
vec2 = reshape(rawData(2254:2480 , 1565:1856,5), s2(1)*s2(2),1);
vec3 = reshape(rawData(2980:3327 , 2318:2771,5), s3(1)*s3(2),1);
std_11Dec(5,1) = std(double(vec1));
std_11Dec(5,2) = std(double(vec2));
std_11Dec(5,3) = std(double(vec3));

```

```

data_11Dec(6,1) = mean(mean(rawData(1414:1710 , 1770:1953,6)));
data_11Dec(6,2) = mean(mean(rawData(2254:2480 , 1565:1856,6)));
data_11Dec(6,3) = mean(mean(rawData(2980:3327 , 2318:2771,6)));
vec1 = reshape(rawData(1414:1710 , 1770:1953,6), s1(1)*s1(2),1);
vec2 = reshape(rawData(2254:2480 , 1565:1856,6), s2(1)*s2(2),1);
vec3 = reshape(rawData(2980:3327 , 2318:2771,6), s3(1)*s3(2),1);
std_11Dec(6,1) = std(double(vec1));
std_11Dec(6,2) = std(double(vec2));
std_11Dec(6,3) = std(double(vec3));

```

```

data_11Dec(7,1) = mean(mean(rawData(1414:1710 , 1770:1953,7)));
data_11Dec(7,2) = mean(mean(rawData(2254:2480 , 1565:1856,7)));
data_11Dec(7,3) = mean(mean(rawData(2980:3327 , 2318:2771,7)));
vec1 = reshape(rawData(1414:1710 , 1770:1953,7), s1(1)*s1(2),1);
vec2 = reshape(rawData(2254:2480 , 1565:1856,7), s2(1)*s2(2),1);
vec3 = reshape(rawData(2980:3327 , 2318:2771,7), s3(1)*s3(2),1);
std_11Dec(7,1) = std(double(vec1));
std_11Dec(7,2) = std(double(vec2));
std_11Dec(7,3) = std(double(vec3));

```

```

data_11Dec(8,1) = mean(mean(rawData(1414:1710 , 1770:1953,8)));
data_11Dec(8,2) = mean(mean(rawData(2254:2480 , 1565:1856,8)));
data_11Dec(8,3) = mean(mean(rawData(2980:3327 , 2318:2771,8)));
vec1 = reshape(rawData(1414:1710 , 1770:1953,8), s1(1)*s1(2),1);
vec2 = reshape(rawData(2254:2480 , 1565:1856,8), s2(1)*s2(2),1);
vec3 = reshape(rawData(2980:3327 , 2318:2771,8), s3(1)*s3(2),1);
std_11Dec(8,1) = std(double(vec1));
std_11Dec(8,2) = std(double(vec2));
std_11Dec(8,3) = std(double(vec3));

```

```
clear rawData;
```

```
% 13 Dec 2013 data
```

```

rawDataFull =
importdata('C:\Users\Paula\Desktop\thesisAnalysis\thesis_data_subset\output\WV02_13DEC13163520_103001002
B973000_13DEC13163520-M1BS-500106170150_01_P003_u16ns3031.tif');
rawData = rawDataFull(3349:7872,2532:5709,:);
clear rawDataFull;

data_13Dec(1,1) = mean(mean(rawData(1665:2030 , 1249:1389,1)));
data_13Dec(1,2) = mean(mean(rawData(2693:3038 , 1028:1319,1)));
data_13Dec(1,3) = mean(mean(rawData(3336:3609 , 1621:2192,1)));
s1 = size(rawData(1665:2030 , 1249:1389,1));
s2 = size(rawData(2693:3038 , 1028:1319,1));
s3 = size(rawData(3336:3609 , 1621:2192,1));
vec1 = reshape(rawData(1665:2030 , 1249:1389,1), s1(1)*s1(2),1);
vec2 = reshape(rawData(2693:3038 , 1028:1319,1), s2(1)*s2(2),1);
vec3 = reshape(rawData(3336:3609 , 1621:2192,1), s3(1)*s3(2),1);
std_13Dec(1,1) = std(double(vec1));
std_13Dec(1,2) = std(double(vec2));
std_13Dec(1,3) = std(double(vec3));

data_13Dec(2,1) = mean(mean(rawData(1665:2030 , 1249:1389,2)));
data_13Dec(2,2) = mean(mean(rawData(2693:3038 , 1028:1319,2)));
data_13Dec(2,3) = mean(mean(rawData(3336:3609 , 1621:2192,2)));
vec1 = reshape(rawData(1665:2030 , 1249:1389,2), s1(1)*s1(2),1);
vec2 = reshape(rawData(2693:3038 , 1028:1319,2), s2(1)*s2(2),1);
vec3 = reshape(rawData(3336:3609 , 1621:2192,2), s3(1)*s3(2),1);
std_13Dec(2,1) = std(double(vec1));
std_13Dec(2,2) = std(double(vec2));
std_13Dec(2,3) = std(double(vec3));

data_13Dec(3,1) = mean(mean(rawData(1665:2030 , 1249:1389,3)));
data_13Dec(3,2) = mean(mean(rawData(2693:3038 , 1028:1319,3)));
data_13Dec(3,3) = mean(mean(rawData(3336:3609 , 1621:2192,3)));
vec1 = reshape(rawData(1665:2030 , 1249:1389,3), s1(1)*s1(2),1);
vec2 = reshape(rawData(2693:3038 , 1028:1319,3), s2(1)*s2(2),1);
vec3 = reshape(rawData(3336:3609 , 1621:2192,3), s3(1)*s3(2),1);
std_13Dec(3,1) = std(double(vec1));
std_13Dec(3,2) = std(double(vec2));
std_13Dec(3,3) = std(double(vec3));

data_13Dec(4,1) = mean(mean(rawData(1665:2030 , 1249:1389,4)));
data_13Dec(4,2) = mean(mean(rawData(2693:3038 , 1028:1319,4)));
data_13Dec(4,3) = mean(mean(rawData(3336:3609 , 1621:2192,4)));
vec1 = reshape(rawData(1665:2030 , 1249:1389,4), s1(1)*s1(2),1);
vec2 = reshape(rawData(2693:3038 , 1028:1319,4), s2(1)*s2(2),1);
vec3 = reshape(rawData(3336:3609 , 1621:2192,4), s3(1)*s3(2),1);
std_13Dec(4,1) = std(double(vec1));
std_13Dec(4,2) = std(double(vec2));
std_13Dec(4,3) = std(double(vec3));

data_13Dec(5,1) = mean(mean(rawData(1665:2030 , 1249:1389,5)));
data_13Dec(5,2) = mean(mean(rawData(2693:3038 , 1028:1319,5)));
data_13Dec(5,3) = mean(mean(rawData(3336:3609 , 1621:2192,5)));
vec1 = reshape(rawData(1665:2030 , 1249:1389,5), s1(1)*s1(2),1);
vec2 = reshape(rawData(2693:3038 , 1028:1319,5), s2(1)*s2(2),1);
vec3 = reshape(rawData(3336:3609 , 1621:2192,5), s3(1)*s3(2),1);

```

```

std_13Dec(5,1) = std(double(vec1));
std_13Dec(5,2) = std(double(vec2));
std_13Dec(5,3) = std(double(vec3));

data_13Dec(6,1) = mean(mean(rawData(1665:2030 , 1249:1389,6)));
data_13Dec(6,2) = mean(mean(rawData(2693:3038 , 1028:1319,6)));
data_13Dec(6,3) = mean(mean(rawData(3336:3609 , 1621:2192,6)));
vec1 = reshape(rawData(1665:2030 , 1249:1389,6), s1(1)*s1(2),1);
vec2 = reshape(rawData(2693:3038 , 1028:1319,6), s2(1)*s2(2),1);
vec3 = reshape(rawData(3336:3609 , 1621:2192,6), s3(1)*s3(2),1);
std_13Dec(6,1) = std(double(vec1));
std_13Dec(6,2) = std(double(vec2));
std_13Dec(6,3) = std(double(vec3));

data_13Dec(7,1) = mean(mean(rawData(1665:2030 , 1249:1389,7)));
data_13Dec(7,2) = mean(mean(rawData(2693:3038 , 1028:1319,7)));
data_13Dec(7,3) = mean(mean(rawData(3336:3609 , 1621:2192,7)));
vec1 = reshape(rawData(1665:2030 , 1249:1389,7), s1(1)*s1(2),1);
vec2 = reshape(rawData(2693:3038 , 1028:1319,7), s2(1)*s2(2),1);
vec3 = reshape(rawData(3336:3609 , 1621:2192,7), s3(1)*s3(2),1);
std_13Dec(7,1) = std(double(vec1));
std_13Dec(7,2) = std(double(vec2));
std_13Dec(7,3) = std(double(vec3));

data_13Dec(8,1) = mean(mean(rawData(1665:2030 , 1249:1389,8)));
data_13Dec(8,2) = mean(mean(rawData(2693:3038 , 1028:1319,8)));
data_13Dec(8,3) = mean(mean(rawData(3336:3609 , 1621:2192,8)));
vec1 = reshape(rawData(1665:2030 , 1249:1389,8), s1(1)*s1(2),1);
vec2 = reshape(rawData(2693:3038 , 1028:1319,8), s2(1)*s2(2),1);
vec3 = reshape(rawData(3336:3609 , 1621:2192,8), s3(1)*s3(2),1);
std_13Dec(8,1) = std(double(vec1));
std_13Dec(8,2) = std(double(vec2));
std_13Dec(8,3) = std(double(vec3));

clear rawData;

% 13 Dec 2013 data second data set
rawDataFull =
importdata('C:\Users\Paula\Desktop\thesisAnalysis\thesis_data_subset\output\WV02_13DEC13163632_103001002
A0A9500_13DEC13163632-M1BS-500110222050_01_P003_u16ns3031.tif');
rawData = rawDataFull(2586:6913,2299:6195,:);
clear rawDataFull;

data_13Dec2(1,1) = mean(mean(rawData(1407:1752 ,1718:1894,1)));
data_13Dec2(1,2) = mean(mean(rawData(2576:3055 ,1463:1875,1)));
data_13Dec2(1,3) = mean(mean(rawData(3141:3472 ,2218:2765,1)));
s1 = size(rawData(1407:1752 ,1718:1894,1));
s2 = size(rawData(2576:3055 ,1463:1875,1));
s3 = size(rawData(3141:3472 ,2218:2765,1));
vec1 = reshape(rawData(1407:1752 ,1718:1894,1), s1(1)*s1(2),1);
vec2 = reshape(rawData(2576:3055 ,1463:1875,1), s2(1)*s2(2),1);
vec3 = reshape(rawData(3141:3472 ,2218:2765,1), s3(1)*s3(2),1);
std_13Dec2(1,1) = std(double(vec1));
std_13Dec2(1,2) = std(double(vec2));
std_13Dec2(1,3) = std(double(vec3));

```

```

data_13Dec2(2,1) = mean(mean(rawData(1407:1752 ,1718:1894,2)));
data_13Dec2(2,2) = mean(mean(rawData(2576:3055 ,1463:1875,2)));
data_13Dec2(2,3) = mean(mean(rawData(3141:3472 ,2218:2765,2)));
vec1 = reshape(rawData(1407:1752 ,1718:1894,2), s1(1)*s1(2),1);
vec2 = reshape(rawData(2576:3055 ,1463:1875,2), s2(1)*s2(2),1);
vec3 = reshape(rawData(3141:3472 ,2218:2765,2), s3(1)*s3(2),1);
std_13Dec2(2,1) = std(double(vec1));
std_13Dec2(2,2) = std(double(vec2));
std_13Dec2(2,3) = std(double(vec3));

```

```

data_13Dec2(3,1) = mean(mean(rawData(1407:1752 ,1718:1894,3)));
data_13Dec2(3,2) = mean(mean(rawData(2576:3055 ,1463:1875,3)));
data_13Dec2(3,3) = mean(mean(rawData(3141:3472 ,2218:2765,3)));
vec1 = reshape(rawData(1407:1752 ,1718:1894,3), s1(1)*s1(2),1);
vec2 = reshape(rawData(2576:3055 ,1463:1875,3), s2(1)*s2(2),1);
vec3 = reshape(rawData(3141:3472 ,2218:2765,3), s3(1)*s3(2),1);
std_13Dec2(3,1) = std(double(vec1));
std_13Dec2(3,2) = std(double(vec2));
std_13Dec2(3,3) = std(double(vec3));

```

```

data_13Dec2(4,1) = mean(mean(rawData(1407:1752 ,1718:1894,4)));
data_13Dec2(4,2) = mean(mean(rawData(2576:3055 ,1463:1875,4)));
data_13Dec2(4,3) = mean(mean(rawData(3141:3472 ,2218:2765,4)));
vec1 = reshape(rawData(1407:1752 ,1718:1894,4), s1(1)*s1(2),1);
vec2 = reshape(rawData(2576:3055 ,1463:1875,4), s2(1)*s2(2),1);
vec3 = reshape(rawData(3141:3472 ,2218:2765,4), s3(1)*s3(2),1);
std_13Dec2(4,1) = std(double(vec1));
std_13Dec2(4,2) = std(double(vec2));
std_13Dec2(4,3) = std(double(vec3));

```

```

data_13Dec2(5,1) = mean(mean(rawData(1407:1752 ,1718:1894,5)));
data_13Dec2(5,2) = mean(mean(rawData(2576:3055 ,1463:1875,5)));
data_13Dec2(5,3) = mean(mean(rawData(3141:3472 ,2218:2765,5)));
vec1 = reshape(rawData(1407:1752 ,1718:1894,5), s1(1)*s1(2),1);
vec2 = reshape(rawData(2576:3055 ,1463:1875,5), s2(1)*s2(2),1);
vec3 = reshape(rawData(3141:3472 ,2218:2765,5), s3(1)*s3(2),1);
std_13Dec2(5,1) = std(double(vec1));
std_13Dec2(5,2) = std(double(vec2));
std_13Dec2(5,3) = std(double(vec3));

```

```

data_13Dec2(6,1) = mean(mean(rawData(1407:1752 ,1718:1894,6)));
data_13Dec2(6,2) = mean(mean(rawData(2576:3055 ,1463:1875,6)));
data_13Dec2(6,3) = mean(mean(rawData(3141:3472 ,2218:2765,6)));
vec1 = reshape(rawData(1407:1752 ,1718:1894,6), s1(1)*s1(2),1);
vec2 = reshape(rawData(2576:3055 ,1463:1875,6), s2(1)*s2(2),1);
vec3 = reshape(rawData(3141:3472 ,2218:2765,6), s3(1)*s3(2),1);
std_13Dec2(6,1) = std(double(vec1));
std_13Dec2(6,2) = std(double(vec2));
std_13Dec2(6,3) = std(double(vec3));

```

```

data_13Dec2(7,1) = mean(mean(rawData(1407:1752 ,1718:1894,7)));
data_13Dec2(7,2) = mean(mean(rawData(2576:3055 ,1463:1875,7)));
data_13Dec2(7,3) = mean(mean(rawData(3141:3472 ,2218:2765,7)));
vec1 = reshape(rawData(1407:1752 ,1718:1894,7), s1(1)*s1(2),1);

```

```

vec2 = reshape(rawData(2576:3055 ,1463:1875,7), s2(1)*s2(2),1);
vec3 = reshape(rawData(3141:3472 ,2218:2765,7), s3(1)*s3(2),1);
std_13Dec2(7,1) = std(double(vec1));
std_13Dec2(7,2) = std(double(vec2));
std_13Dec2(7,3) = std(double(vec3));

```

```

data_13Dec2(8,1) = mean(mean(rawData(1407:1752 ,1718:1894,8)));
data_13Dec2(8,2) = mean(mean(rawData(2576:3055 ,1463:1875,8)));
data_13Dec2(8,3) = mean(mean(rawData(3141:3472 ,2218:2765,8)));
vec1 = reshape(rawData(1407:1752 ,1718:1894,8), s1(1)*s1(2),1);
vec2 = reshape(rawData(2576:3055 ,1463:1875,8), s2(1)*s2(2),1);
vec3 = reshape(rawData(3141:3472 ,2218:2765,8), s3(1)*s3(2),1);
std_13Dec2(8,1) = std(double(vec1));
std_13Dec2(8,2) = std(double(vec2));
std_13Dec2(8,3) = std(double(vec3));

```

```
clear rawData;
```

```
% 25 Jan 2014 data
```

```

rawDataFull =
importdata('C:\Users\Paula\Desktop\thesisAnalysis\thesis_data_subset\output\WV02_14JAN25201052_103001002
B37A900_14JAN25201052-M1BS-500100296100_02_P007_u16ns3031.tif');
rawData = rawDataFull(2642:7541,5166:8729,:);
clear rawDataFull;

```

```

data_14Jan(1,1) = mean(mean(rawData(2067:2419 ,1613:1828,1)));
data_14Jan(1,2) = mean(mean(rawData(2791:3492 ,1266:1755,1)));
data_14Jan(1,3) = mean(mean(rawData(3683:4000 ,2172:2764,1)));
s1 = size(rawData(2067:2419 ,1613:1828,1));
s2 = size(rawData(2791:3492 ,1266:1755,1));
s3 = size(rawData(3683:4000 ,2172:2764,1));
vec1 = reshape(rawData(2067:2419 ,1613:1828,1), s1(1)*s1(2),1);
vec2 = reshape(rawData(2791:3492 ,1266:1755,1), s2(1)*s2(2),1);
vec3 = reshape(rawData(3683:4000 ,2172:2764,1), s3(1)*s3(2),1);
std_14Jan(1,1) = std(double(vec1));
std_14Jan(1,2) = std(double(vec2));
std_14Jan(1,3) = std(double(vec3));

```

```

data_14Jan(2,1) = mean(mean(rawData(2067:2419 ,1613:1828,2)));
data_14Jan(2,2) = mean(mean(rawData(2791:3492 ,1266:1755,2)));
data_14Jan(2,3) = mean(mean(rawData(3683:4000 ,2172:2764,2)));
vec1 = reshape(rawData(2067:2419 ,1613:1828,2), s1(1)*s1(2),1);
vec2 = reshape(rawData(2791:3492 ,1266:1755,2), s2(1)*s2(2),1);
vec3 = reshape(rawData(3683:4000 ,2172:2764,2), s3(1)*s3(2),1);
std_14Jan(2,1) = std(double(vec1));
std_14Jan(2,2) = std(double(vec2));
std_14Jan(2,3) = std(double(vec3));

```

```

data_14Jan(3,1) = mean(mean(rawData(2067:2419 ,1613:1828,3)));
data_14Jan(3,2) = mean(mean(rawData(2791:3492 ,1266:1755,3)));
data_14Jan(3,3) = mean(mean(rawData(3683:4000 ,2172:2764,3)));
vec1 = reshape(rawData(2067:2419 ,1613:1828,3), s1(1)*s1(2),1);
vec2 = reshape(rawData(2791:3492 ,1266:1755,3), s2(1)*s2(2),1);
vec3 = reshape(rawData(3683:4000 ,2172:2764,3), s3(1)*s3(2),1);
std_14Jan(3,1) = std(double(vec1));

```

```

std_14Jan(3,2) = std(double(vec2));
std_14Jan(3,3) = std(double(vec3));

data_14Jan(4,1) = mean(mean(rawData(2067:2419 ,1613:1828,4)));
data_14Jan(4,2) = mean(mean(rawData(2791:3492 ,1266:1755,4)));
data_14Jan(4,3) = mean(mean(rawData(3683:4000 ,2172:2764,4)));
vec1 = reshape(rawData(2067:2419 ,1613:1828,4), s1(1)*s1(2),1);
vec2 = reshape(rawData(2791:3492 ,1266:1755,4), s2(1)*s2(2),1);
vec3 = reshape(rawData(3683:4000 ,2172:2764,4), s3(1)*s3(2),1);
std_14Jan(4,1) = std(double(vec1));
std_14Jan(4,2) = std(double(vec2));
std_14Jan(4,3) = std(double(vec3));

data_14Jan(5,1) = mean(mean(rawData(2067:2419 ,1613:1828,5)));
data_14Jan(5,2) = mean(mean(rawData(2791:3492 ,1266:1755,5)));
data_14Jan(5,3) = mean(mean(rawData(3683:4000 ,2172:2764,5)));
vec1 = reshape(rawData(2067:2419 ,1613:1828,5), s1(1)*s1(2),1);
vec2 = reshape(rawData(2791:3492 ,1266:1755,5), s2(1)*s2(2),1);
vec3 = reshape(rawData(3683:4000 ,2172:2764,5), s3(1)*s3(2),1);
std_14Jan(5,1) = std(double(vec1));
std_14Jan(5,2) = std(double(vec2));
std_14Jan(5,3) = std(double(vec3));

data_14Jan(6,1) = mean(mean(rawData(2067:2419 ,1613:1828,6)));
data_14Jan(6,2) = mean(mean(rawData(2791:3492 ,1266:1755,6)));
data_14Jan(6,3) = mean(mean(rawData(3683:4000 ,2172:2764,6)));
vec1 = reshape(rawData(2067:2419 ,1613:1828,6), s1(1)*s1(2),1);
vec2 = reshape(rawData(2791:3492 ,1266:1755,6), s2(1)*s2(2),1);
vec3 = reshape(rawData(3683:4000 ,2172:2764,6), s3(1)*s3(2),1);
std_14Jan(6,1) = std(double(vec1));
std_14Jan(6,2) = std(double(vec2));
std_14Jan(6,3) = std(double(vec3));

data_14Jan(7,1) = mean(mean(rawData(2067:2419 ,1613:1828,7)));
data_14Jan(7,2) = mean(mean(rawData(2791:3492 ,1266:1755,7)));
data_14Jan(7,3) = mean(mean(rawData(3683:4000 ,2172:2764,7)));
vec1 = reshape(rawData(2067:2419 ,1613:1828,7), s1(1)*s1(2),1);
vec2 = reshape(rawData(2791:3492 ,1266:1755,7), s2(1)*s2(2),1);
vec3 = reshape(rawData(3683:4000 ,2172:2764,7), s3(1)*s3(2),1);
std_14Jan(7,1) = std(double(vec1));
std_14Jan(7,2) = std(double(vec2));
std_14Jan(7,3) = std(double(vec3));

data_14Jan(8,1) = mean(mean(rawData(2067:2419 ,1613:1828,8)));
data_14Jan(8,2) = mean(mean(rawData(2791:3492 ,1266:1755,8)));
data_14Jan(8,3) = mean(mean(rawData(3683:4000 ,2172:2764,8)));
vec1 = reshape(rawData(2067:2419 ,1613:1828,8), s1(1)*s1(2),1);
vec2 = reshape(rawData(2791:3492 ,1266:1755,8), s2(1)*s2(2),1);
vec3 = reshape(rawData(3683:4000 ,2172:2764,8), s3(1)*s3(2),1);
std_14Jan(8,1) = std(double(vec1));
std_14Jan(8,2) = std(double(vec2));
std_14Jan(8,3) = std(double(vec3));

clear rawData;

```

```

% 2 feb 2015 data
rawDataFull =
importdata('C:\Users\Paula\Desktop\thesisAnalysis\thesis_data_subset\output\WV02_15FEB02191005_103001003
C260800_15FEB02191005-MIBS-500316195110_01_P003_u16ns3031.tif');
rawData = rawDataFull(2535:7464,4610:7603,:);
clear rawDataFull;

data_15Feb1(1,1) = mean(mean(rawData(1543:1822 ,1065:1200,1)));
data_15Feb1(1,2) = mean(mean(rawData(2520:3273 ,887:1204,1)));
data_15Feb1(1,3) = mean(mean(rawData(3302:3623 ,1510:2152,1)));
s1 = size(rawData(1543:1822 ,1065:1200,1));
s2 = size(rawData(2520:3273 ,887:1204,1));
s3 = size(rawData(3302:3623 ,1510:2152,1));
vec1 = reshape(rawData(1543:1822 ,1065:1200,1), s1(1)*s1(2),1);
vec2 = reshape(rawData(2520:3273 ,887:1204,1), s2(1)*s2(2),1);
vec3 = reshape(rawData(3302:3623 ,1510:2152,1), s3(1)*s3(2),1);
std_15Feb1(1,1) = std(double(vec1));
std_15Feb1(1,2) = std(double(vec2));
std_15Feb1(1,3) = std(double(vec3));

data_15Feb1(2,1) = mean(mean(rawData(1543:1822 ,1065:1200,2)));
data_15Feb1(2,2) = mean(mean(rawData(2520:3273 ,887:1204,2)));
data_15Feb1(2,3) = mean(mean(rawData(3302:3623 ,1510:2152,2)));
vec1 = reshape(rawData(1543:1822 ,1065:1200,2), s1(1)*s1(2),1);
vec2 = reshape(rawData(2520:3273 ,887:1204,2), s2(1)*s2(2),1);
vec3 = reshape(rawData(3302:3623 ,1510:2152,2), s3(1)*s3(2),1);
std_15Feb1(2,1) = std(double(vec1));
std_15Feb1(2,2) = std(double(vec2));
std_15Feb1(2,3) = std(double(vec3));

data_15Feb1(3,1) = mean(mean(rawData(1543:1822 ,1065:1200,3)));
data_15Feb1(3,2) = mean(mean(rawData(2520:3273 ,887:1204,3)));
data_15Feb1(3,3) = mean(mean(rawData(3302:3623 ,1510:2152,3)));
vec1 = reshape(rawData(1543:1822 ,1065:1200,3), s1(1)*s1(2),1);
vec2 = reshape(rawData(2520:3273 ,887:1204,3), s2(1)*s2(2),1);
vec3 = reshape(rawData(3302:3623 ,1510:2152,3), s3(1)*s3(2),1);
std_15Feb1(3,1) = std(double(vec1));
std_15Feb1(3,2) = std(double(vec2));
std_15Feb1(3,3) = std(double(vec3));

data_15Feb1(4,1) = mean(mean(rawData(1543:1822 ,1065:1200,4)));
data_15Feb1(4,2) = mean(mean(rawData(2520:3273 ,887:1204,4)));
data_15Feb1(4,3) = mean(mean(rawData(3302:3623 ,1510:2152,4)));
vec1 = reshape(rawData(1543:1822 ,1065:1200,4), s1(1)*s1(2),1);
vec2 = reshape(rawData(2520:3273 ,887:1204,4), s2(1)*s2(2),1);
vec3 = reshape(rawData(3302:3623 ,1510:2152,4), s3(1)*s3(2),1);
std_15Feb1(4,1) = std(double(vec1));
std_15Feb1(4,2) = std(double(vec2));
std_15Feb1(4,3) = std(double(vec3));

data_15Feb1(5,1) = mean(mean(rawData(1543:1822 ,1065:1200,5)));
data_15Feb1(5,2) = mean(mean(rawData(2520:3273 ,887:1204,5)));
data_15Feb1(5,3) = mean(mean(rawData(3302:3623 ,1510:2152,5)));
vec1 = reshape(rawData(1543:1822 ,1065:1200,5), s1(1)*s1(2),1);

```

```

vec2 = reshape(rawData(2520:3273 ,887:1204,5), s2(1)*s2(2),1);
vec3 = reshape(rawData(3302:3623 ,1510:2152,5), s3(1)*s3(2),1);
std_15Feb1(5,1) = std(double(vec1));
std_15Feb1(5,2) = std(double(vec2));
std_15Feb1(5,3) = std(double(vec3));

data_15Feb1(6,1) = mean(mean(rawData(1543:1822 ,1065:1200,6)));
data_15Feb1(6,2) = mean(mean(rawData(2520:3273 ,887:1204,6)));
data_15Feb1(6,3) = mean(mean(rawData(3302:3623 ,1510:2152,6)));
vec1 = reshape(rawData(1543:1822 ,1065:1200,6), s1(1)*s1(2),1);
vec2 = reshape(rawData(2520:3273 ,887:1204,6), s2(1)*s2(2),1);
vec3 = reshape(rawData(3302:3623 ,1510:2152,6), s3(1)*s3(2),1);
std_15Feb1(6,1) = std(double(vec1));
std_15Feb1(6,2) = std(double(vec2));
std_15Feb1(6,3) = std(double(vec3));

data_15Feb1(7,1) = mean(mean(rawData(1543:1822 ,1065:1200,7)));
data_15Feb1(7,2) = mean(mean(rawData(2520:3273 ,887:1204,7)));
data_15Feb1(7,3) = mean(mean(rawData(3302:3623 ,1510:2152,7)));
vec1 = reshape(rawData(1543:1822 ,1065:1200,7), s1(1)*s1(2),1);
vec2 = reshape(rawData(2520:3273 ,887:1204,7), s2(1)*s2(2),1);
vec3 = reshape(rawData(3302:3623 ,1510:2152,7), s3(1)*s3(2),1);
std_15Feb1(7,1) = std(double(vec1));
std_15Feb1(7,2) = std(double(vec2));
std_15Feb1(7,3) = std(double(vec3));

data_15Feb1(8,1) = mean(mean(rawData(1543:1822 ,1065:1200,8)));
data_15Feb1(8,2) = mean(mean(rawData(2520:3273 ,887:1204,8)));
data_15Feb1(8,3) = mean(mean(rawData(3302:3623 ,1510:2152,8)));
vec1 = reshape(rawData(1543:1822 ,1065:1200,8), s1(1)*s1(2),1);
vec2 = reshape(rawData(2520:3273 ,887:1204,8), s2(1)*s2(2),1);
vec3 = reshape(rawData(3302:3623 ,1510:2152,8), s3(1)*s3(2),1);
std_15Feb1(8,1) = std(double(vec1));
std_15Feb1(8,2) = std(double(vec2));
std_15Feb1(8,3) = std(double(vec3));

clear rawData;

% 2 feb 2015 data set 2
rawDataFull =
importdata('C:\Users\Paula\Desktop\thesisAnalysis\thesis_data_subset\output\WV02_15FEB02191125_103001003
CC6E400_15FEB02191125-M1BS-500340690080_01_P003_u16ns3031.tif');
rawData = rawDataFull(2169:6835,4404:7659,:);
clear rawDataFull;

data_15Feb2(1,1) = mean(mean(rawData(1712:1967 ,1291:1449,1)));
data_15Feb2(1,2) = mean(mean(rawData(2626:3503 ,1138:1376,1)));
data_15Feb2(1,3) = mean(mean(rawData(3430:3778 ,1756:2161,1)));
s1 = size(rawData(1712:1967 ,1291:1449,1));
s2 = size(rawData(2626:3503 ,1138:1376,1));
s3 = size(rawData(3430:3778 ,1756:2161,1));
vec1 = reshape(rawData(1712:1967 ,1291:1449,1), s1(1)*s1(2),1);
vec2 = reshape(rawData(2626:3503 ,1138:1376,1), s2(1)*s2(2),1);
vec3 = reshape(rawData(3430:3778 ,1756:2161,1), s3(1)*s3(2),1);
std_15Feb2(1,1) = std(double(vec1));

```



```

std_15Feb2(1,2) = std(double(vec2));
std_15Feb2(1,3) = std(double(vec3));

data_15Feb2(2,1) = mean(mean(rawData(1712:1967 ,1291:1449,2)));
data_15Feb2(2,2) = mean(mean(rawData(2626:3503 ,1138:1376,2)));
data_15Feb2(2,3) = mean(mean(rawData(3430:3778 ,1756:2161,2)));
vec1 = reshape(rawData(1712:1967 ,1291:1449,2), s1(1)*s1(2),1);
vec2 = reshape(rawData(2626:3503 ,1138:1376,2), s2(1)*s2(2),1);
vec3 = reshape(rawData(3430:3778 ,1756:2161,2), s3(1)*s3(2),1);
std_15Feb2(2,1) = std(double(vec1));
std_15Feb2(2,2) = std(double(vec2));
std_15Feb2(2,3) = std(double(vec3));

data_15Feb2(3,1) = mean(mean(rawData(1712:1967 ,1291:1449,3)));
data_15Feb2(3,2) = mean(mean(rawData(2626:3503 ,1138:1376,3)));
data_15Feb2(3,3) = mean(mean(rawData(3430:3778 ,1756:2161,3)));
vec1 = reshape(rawData(1712:1967 ,1291:1449,3), s1(1)*s1(2),1);
vec2 = reshape(rawData(2626:3503 ,1138:1376,3), s2(1)*s2(2),1);
vec3 = reshape(rawData(3430:3778 ,1756:2161,3), s3(1)*s3(2),1);
std_15Feb2(3,1) = std(double(vec1));
std_15Feb2(3,2) = std(double(vec2));
std_15Feb2(3,3) = std(double(vec3));

data_15Feb2(4,1) = mean(mean(rawData(1712:1967 ,1291:1449,4)));
data_15Feb2(4,2) = mean(mean(rawData(2626:3503 ,1138:1376,4)));
data_15Feb2(4,3) = mean(mean(rawData(3430:3778 ,1756:2161,4)));
vec1 = reshape(rawData(1712:1967 ,1291:1449,4), s1(1)*s1(2),1);
vec2 = reshape(rawData(2626:3503 ,1138:1376,4), s2(1)*s2(2),1);
vec3 = reshape(rawData(3430:3778 ,1756:2161,4), s3(1)*s3(2),1);
std_15Feb2(4,1) = std(double(vec1));
std_15Feb2(4,2) = std(double(vec2));
std_15Feb2(4,3) = std(double(vec3));

data_15Feb2(5,1) = mean(mean(rawData(1712:1967 ,1291:1449,5)));
data_15Feb2(5,2) = mean(mean(rawData(2626:3503 ,1138:1376,5)));
data_15Feb2(5,3) = mean(mean(rawData(3430:3778 ,1756:2161,5)));
vec1 = reshape(rawData(1712:1967 ,1291:1449,5), s1(1)*s1(2),1);
vec2 = reshape(rawData(2626:3503 ,1138:1376,5), s2(1)*s2(2),1);
vec3 = reshape(rawData(3430:3778 ,1756:2161,5), s3(1)*s3(2),1);
std_15Feb2(5,1) = std(double(vec1));
std_15Feb2(5,2) = std(double(vec2));
std_15Feb2(5,3) = std(double(vec3));

data_15Feb2(6,1) = mean(mean(rawData(1712:1967 ,1291:1449,6)));
data_15Feb2(6,2) = mean(mean(rawData(2626:3503 ,1138:1376,6)));
data_15Feb2(6,3) = mean(mean(rawData(3430:3778 ,1756:2161,6)));
vec1 = reshape(rawData(1712:1967 ,1291:1449,6), s1(1)*s1(2),1);
vec2 = reshape(rawData(2626:3503 ,1138:1376,6), s2(1)*s2(2),1);
vec3 = reshape(rawData(3430:3778 ,1756:2161,6), s3(1)*s3(2),1);
std_15Feb2(6,1) = std(double(vec1));
std_15Feb2(6,2) = std(double(vec2));
std_15Feb2(6,3) = std(double(vec3));

data_15Feb2(7,1) = mean(mean(rawData(1712:1967 ,1291:1449,7)));
data_15Feb2(7,2) = mean(mean(rawData(2626:3503 ,1138:1376,7)));

```

```

data_15Feb2(7,3) = mean(mean(rawData(3430:3778 ,1756:2161,7)));
vec1 = reshape(rawData(1712:1967 ,1291:1449,7), s1(1)*s1(2),1);
vec2 = reshape(rawData(2626:3503 ,1138:1376,7), s2(1)*s2(2),1);
vec3 = reshape(rawData(3430:3778 ,1756:2161,7), s3(1)*s3(2),1);
std_15Feb2(7,1) = std(double(vec1));
std_15Feb2(7,2) = std(double(vec2));
std_15Feb2(7,3) = std(double(vec3));

data_15Feb2(8,1) = mean(mean(rawData(1712:1967 ,1291:1449,8)));
data_15Feb2(8,2) = mean(mean(rawData(2626:3503 ,1138:1376,8)));
data_15Feb2(8,3) = mean(mean(rawData(3430:3778 ,1756:2161,8)));
vec1 = reshape(rawData(1712:1967 ,1291:1449,8), s1(1)*s1(2),1);
vec2 = reshape(rawData(2626:3503 ,1138:1376,8), s2(1)*s2(2),1);
vec3 = reshape(rawData(3430:3778 ,1756:2161,8), s3(1)*s3(2),1);
std_15Feb2(8,1) = std(double(vec1));
std_15Feb2(8,2) = std(double(vec2));
std_15Feb2(8,3) = std(double(vec3));

clear rawData;

% now that all the means have been found for each subimage of each image
% chip, combine these is a mean for each region for each band
for b = 1:8
    for i = 1:3
        vec = [data_11Dec(b,i) data_13Dec(b,i) data_13Dec2(b,i) data_14Jan(b,i) data_15Feb1(b,i) data_15Feb2(b,i)];
        tbl_mean(i,b) = mean(vec);
    end
end

% tbl_mean can now be used as input to the PCA function

% This script inputs an image, computes NDI on each pixel in the image
% and plot the results
% load image chip
clear;
close all;

% 22Dec 2011 data
rawDataFull =
importdata('C:\Users\Paula\Desktop\thesisAnalysis\thesis_data_subset\output\WV02_11DEC22195305_103001001
0AAEE00_11DEC22195305-M1BS-500092642100_01_P003_u16ns3031.tif');
rawData = rawDataFull(1530:5728,5380:9334,:);
% clear the full array so save processing time and memory
clear rawDataFull;
r1Sum = 0;
r2Sum = 0;
r3Sum = 0;

for i = 1:8
    r1Sum = r1Sum + rawData(1414:1710 , 1770:1953,i);
    r2Sum = r2Sum + rawData(2254:2480 , 1565:1856,i);
    r3Sum = r3Sum + rawData(2980:3327 , 2318:2771,i);
end

```

```
r1_2 = double(rawData(1414:1710 , 1770:1953,2))./double(r1Sum);  
r2_2 = double(rawData(2254:2480 , 1565:1856,2))./double(r2Sum);  
r3_2 = double(rawData(2980:3327 , 2318:2771,2))./double(r3Sum);
```

```
r1_7 = double(rawData(1414:1710 , 1770:1953,7))./double(r1Sum);  
r2_7 = double(rawData(2254:2480 , 1565:1856,7))./double(r2Sum);  
r3_7 = double(rawData(2980:3327 , 2318:2771,7))./double(r3Sum);
```

```
% calculate NDI for each pixel
```

```
ndiData1 = (r1_7 - r1_2)./(r1_7 + r1_2);  
ndiData2 = (r2_7 - r2_2)./(r2_7 + r2_2);  
ndiData3 = (r3_7 - r3_2)./(r3_7 + r3_2);
```

```
% map
```

```
figure  
imagesc(ndiData1);  
figure  
imagesc(ndiData2);  
figure  
imagesc(ndiData3);
```

## APPENDIX B: IMAGE CHIPS AND SUB-IMAGES

Below are figures showing the image chips from each data set used in the PCA analysis as well as the sub-image from each of those image chips. All image chips and sub-images are from Band 8 of the data set. Note that color scale is different for each image and pixel sizes vary for each of the sub-images.

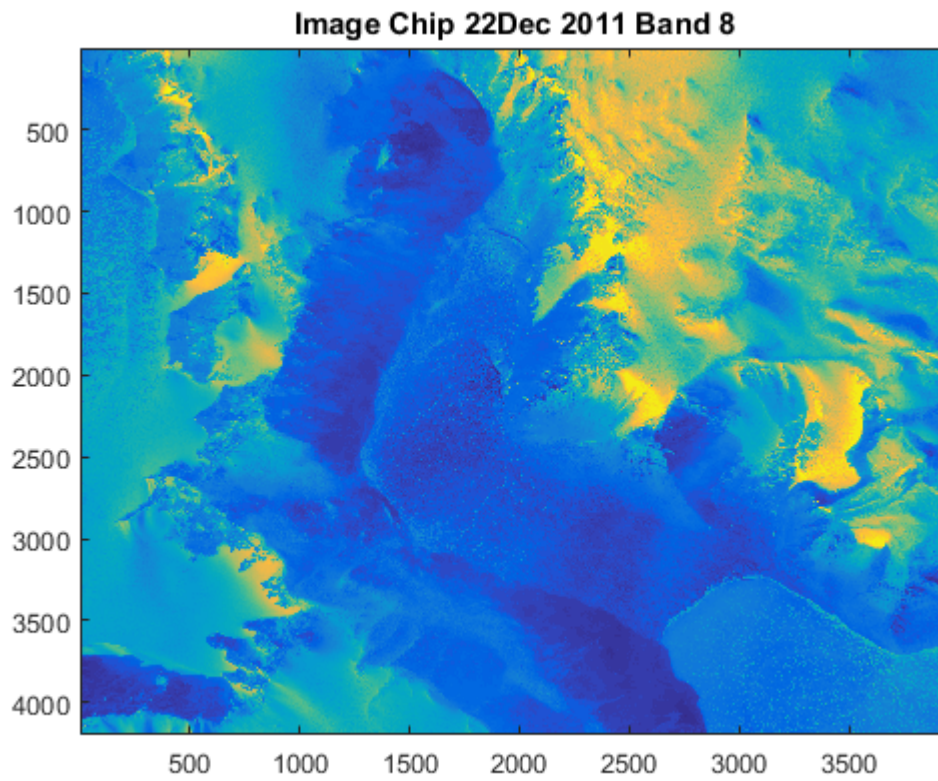


**Figure 23: Image Chip from 22 Dec 2011, Band 8**

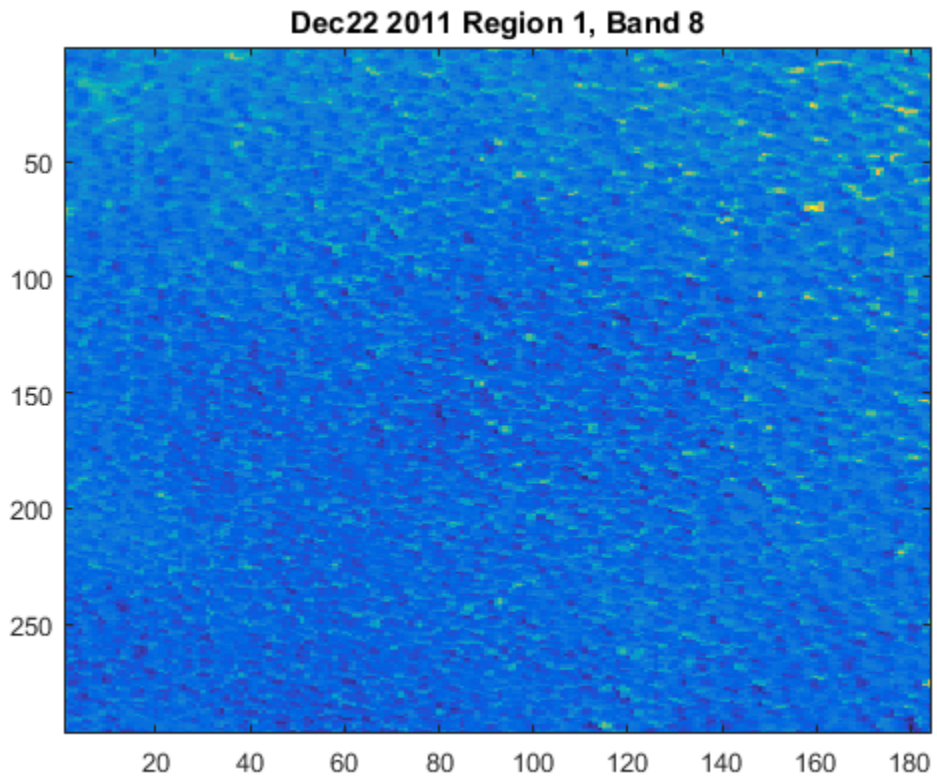


**Figure 24: Region 1 Sub-Image from 22 Dec 2011, Band 8**

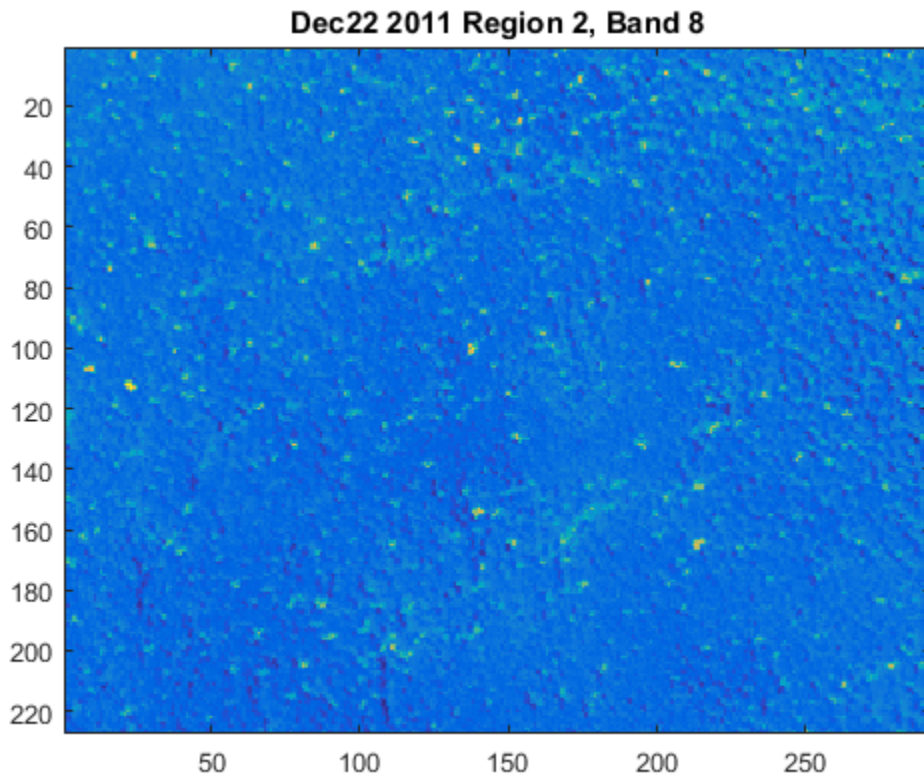


**Figure 25: Region 2 Sub-Image from 22 Dec 2011, Band 8**

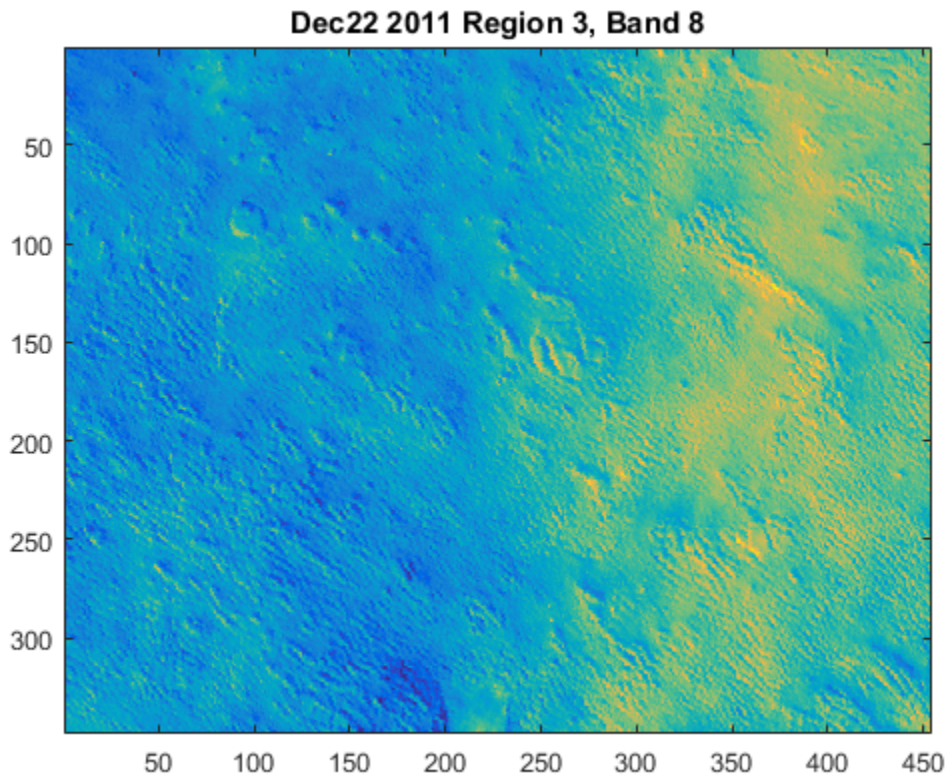


**Figure 26: Region 3 Sub-Image from 22 Dec 2011, Band 8**

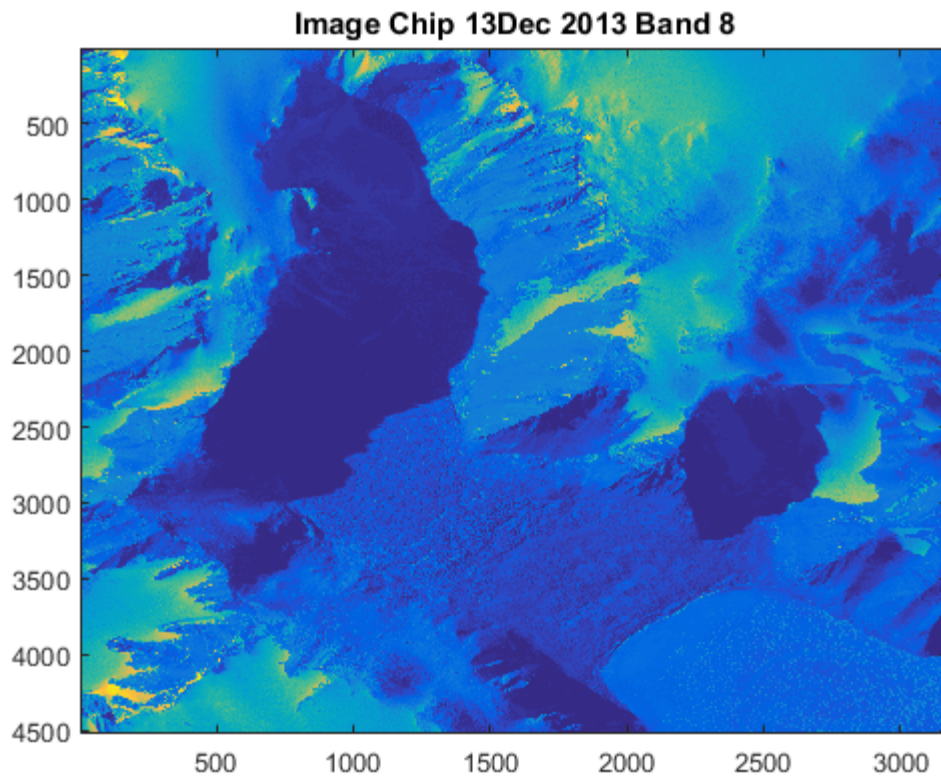


**Figure 27: Image Chip from 13 Dec 2013, Band 8**



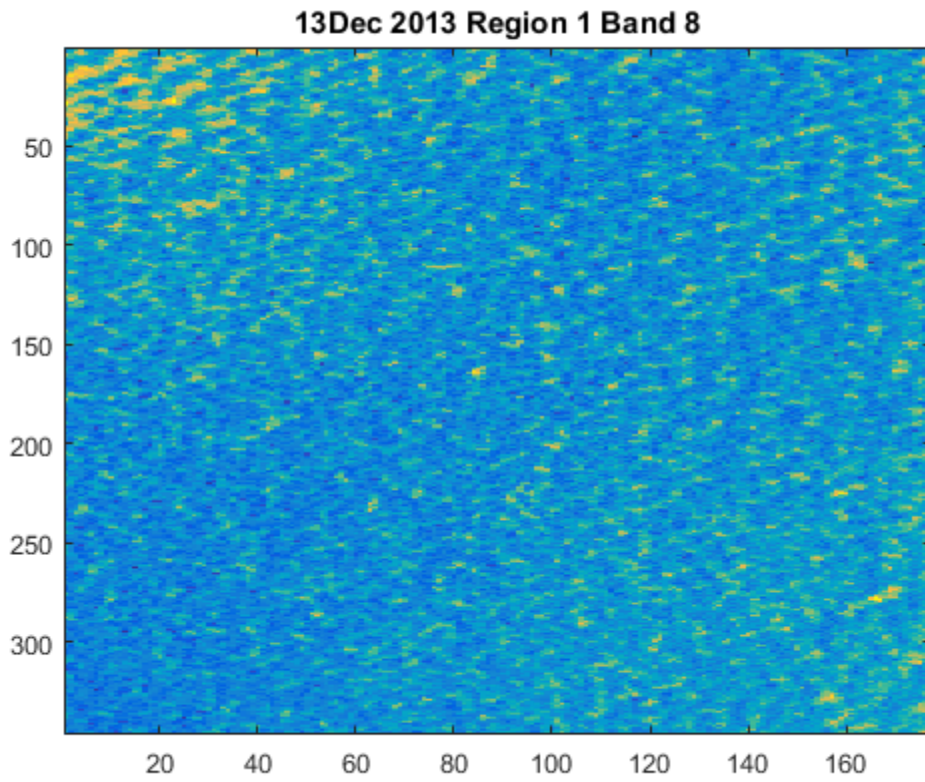


**Figure 28: Region 1 Sub-Image from 13 Dec 2013, Band 8**

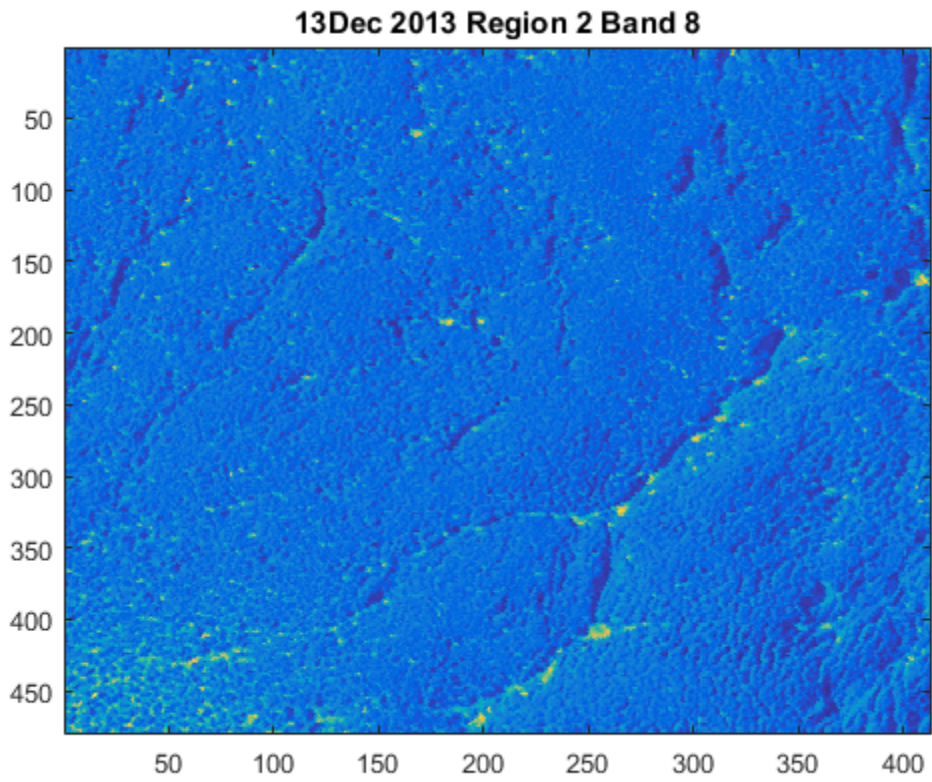


**Figure 29: Region 2 Sub-Image from 13 Dec 2013, Band 8**

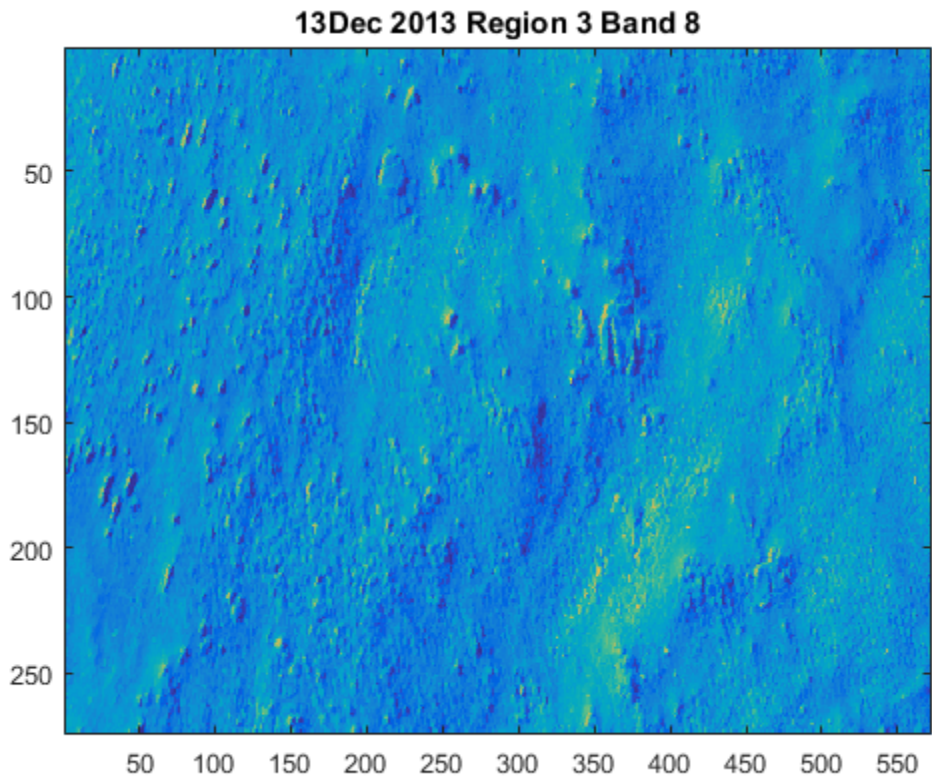


**Figure 30: Region 3 Sub-Image from 13 Dec 2013, Band 8**

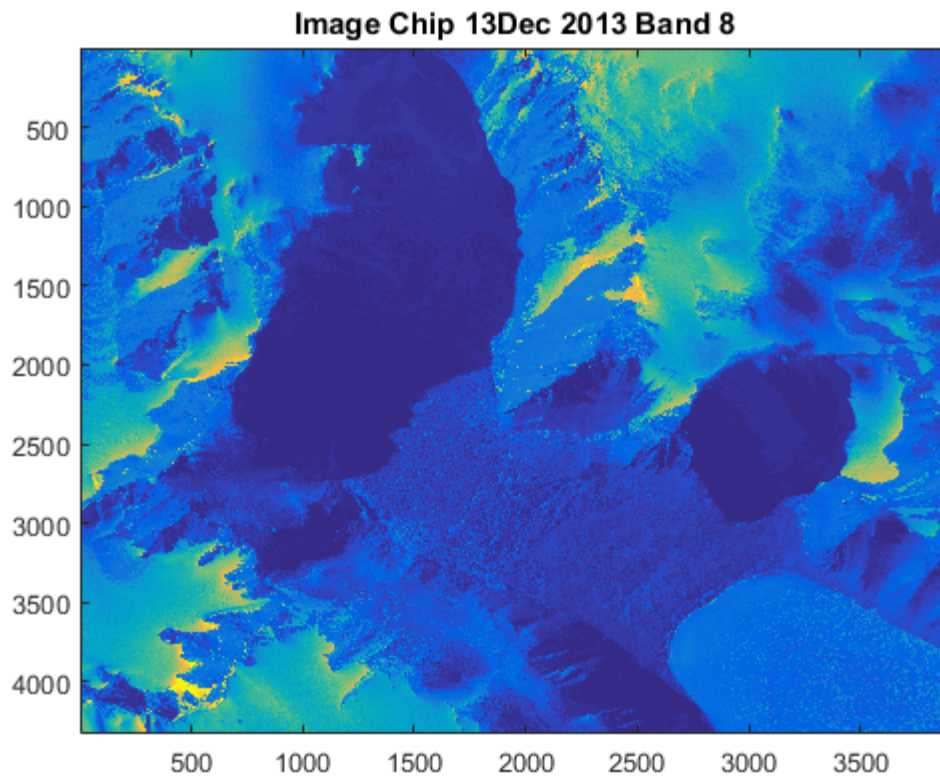


**Figure 31: Image Chip from 13 Dec 2013 (second image collected), Band 8**

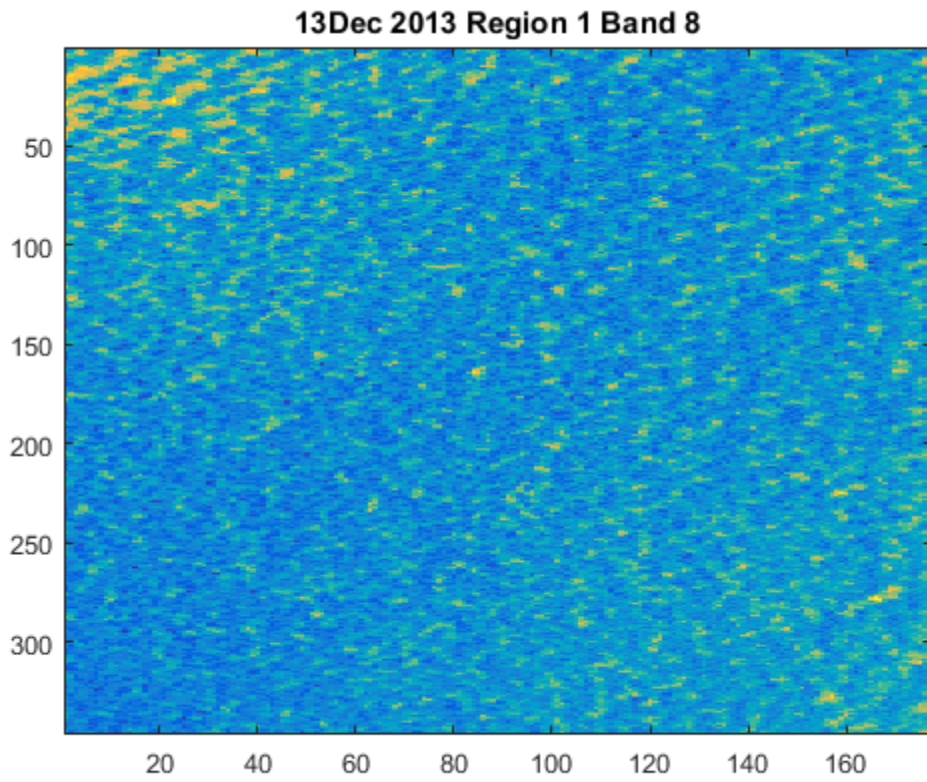


**Figure 32: Region 1 Sub-Image from 13 Dec 2013 (second image collected), Band 8**

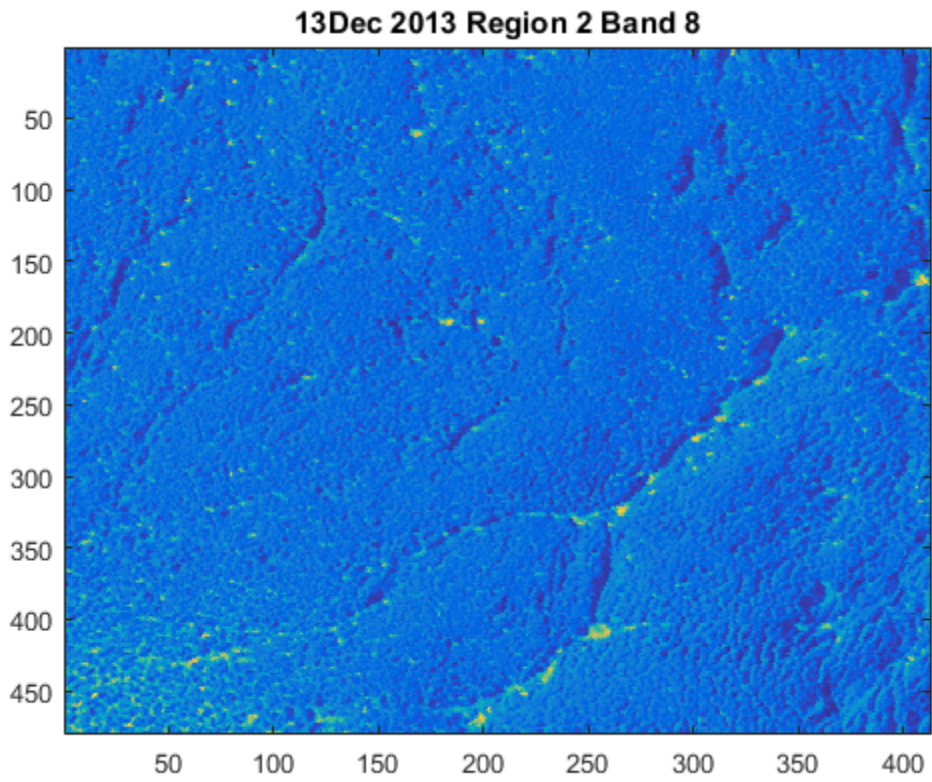


**Figure 33: Region 2 Sub-Image from 13 Dec 2013 (second image collected), Band 8**

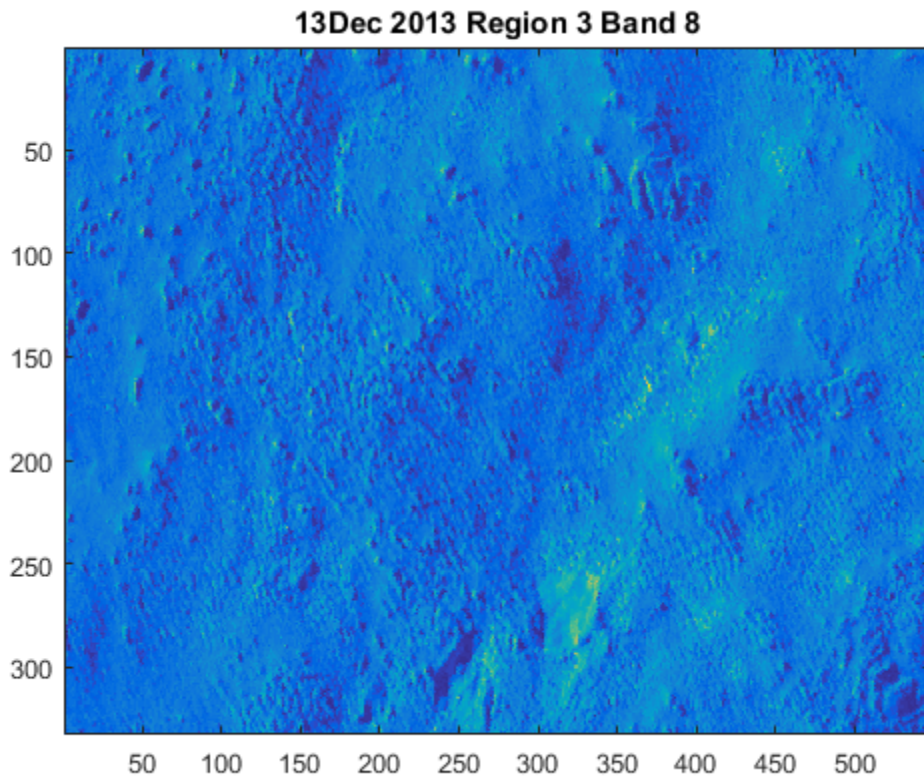


**Figure 34: Region 3 Sub-Image from 13 Dec 2013 (second image collected), Band 8**

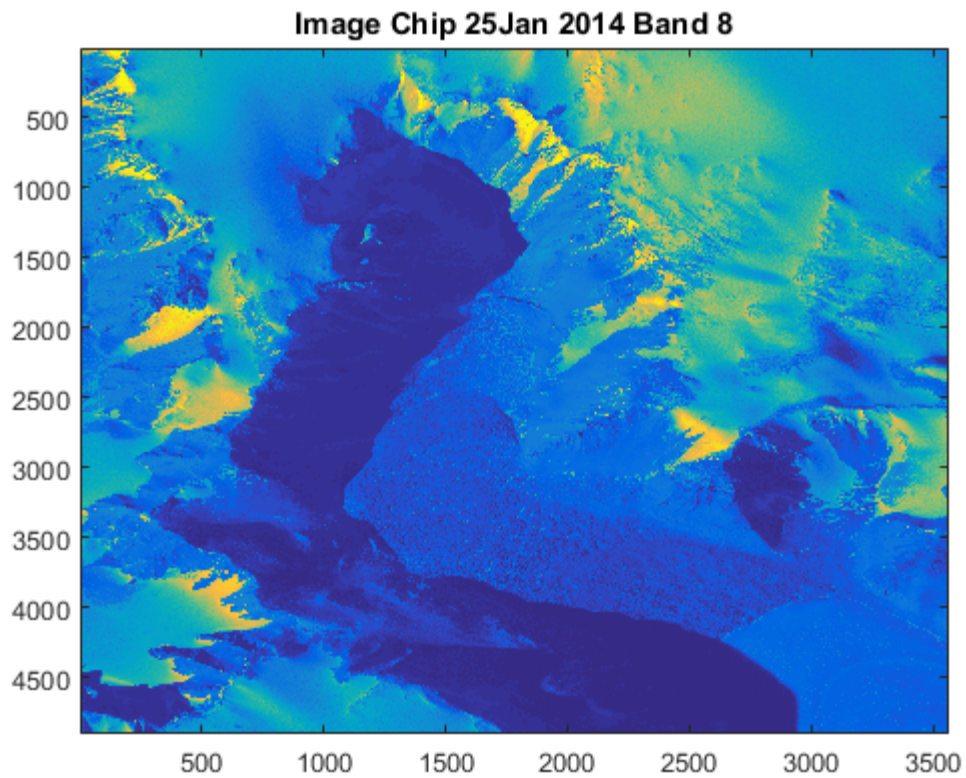


**Figure 35: Image Chip from 25 Jan 2014, Band 8**



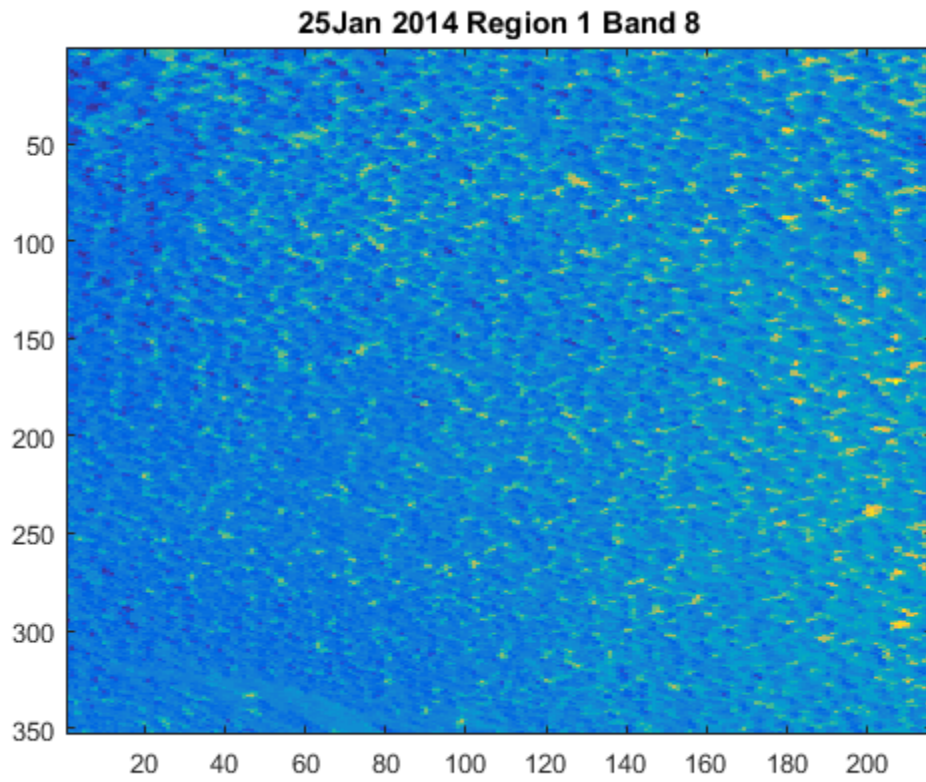


**Figure 36: Region 1 Sub-Image from 25 Jan 2014, Band 8**

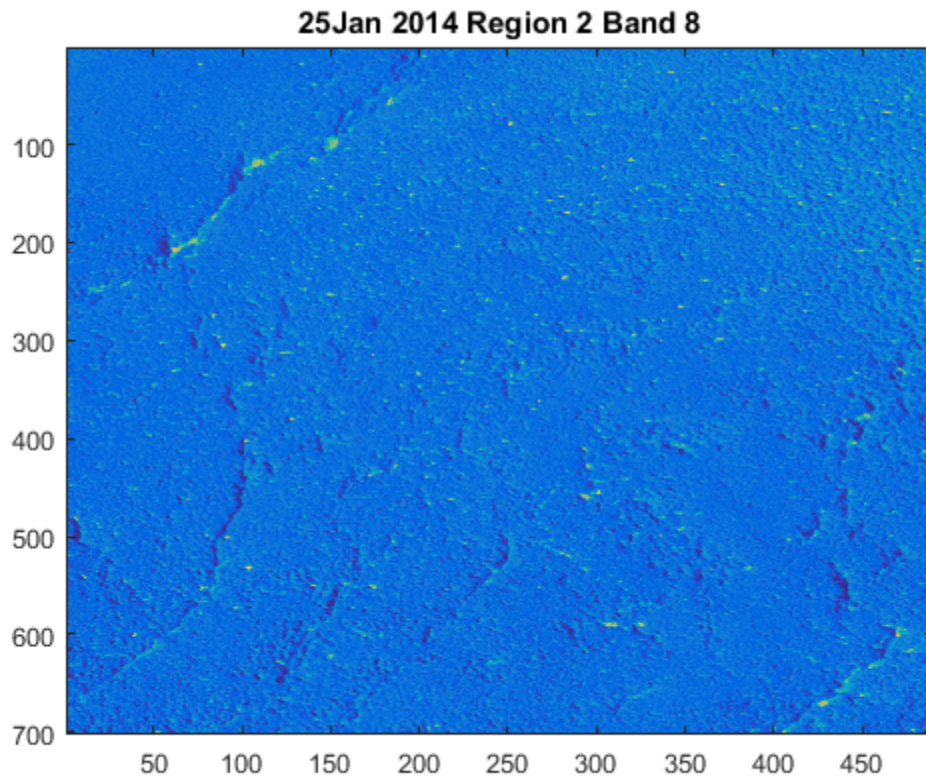


**Figure 37: Region 2 Sub-Image from 25 Jan 2014, Band 8**

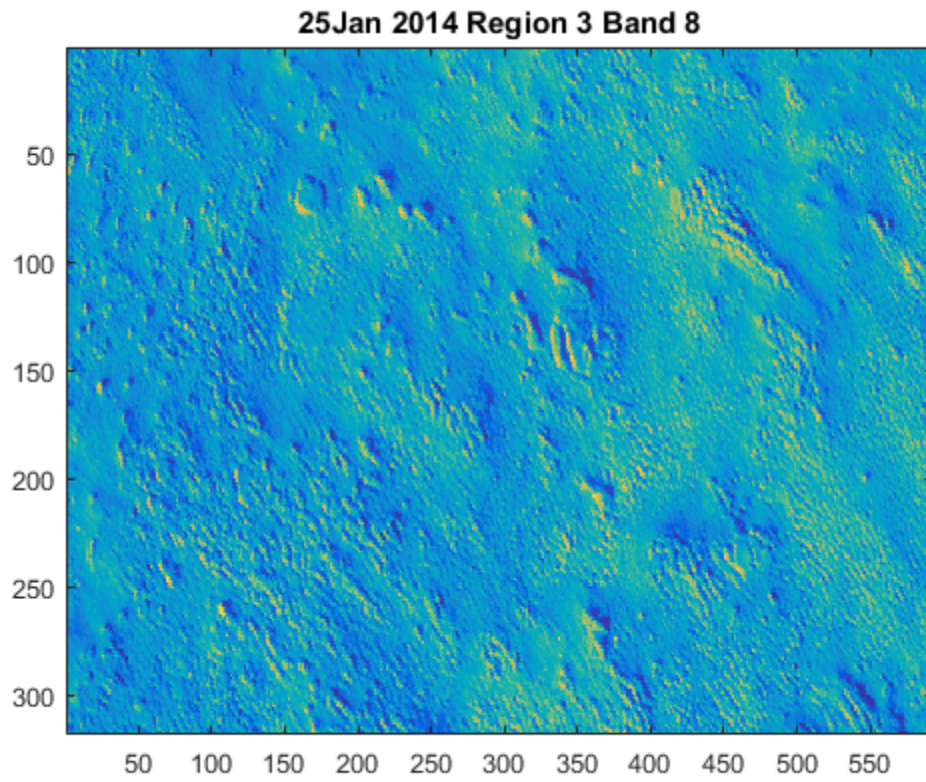


**Figure 38: Region 3 Sub-Image from 25 Jan 2014, Band 8**

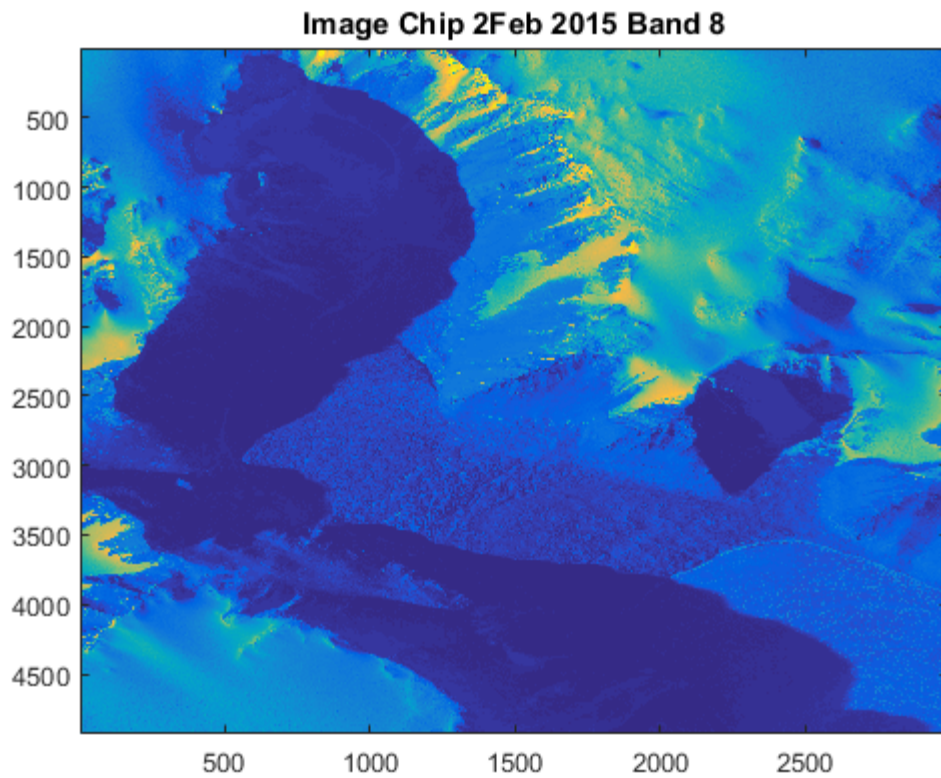


**Figure 39: Image Chip from 2 Feb 2015, Band 8**

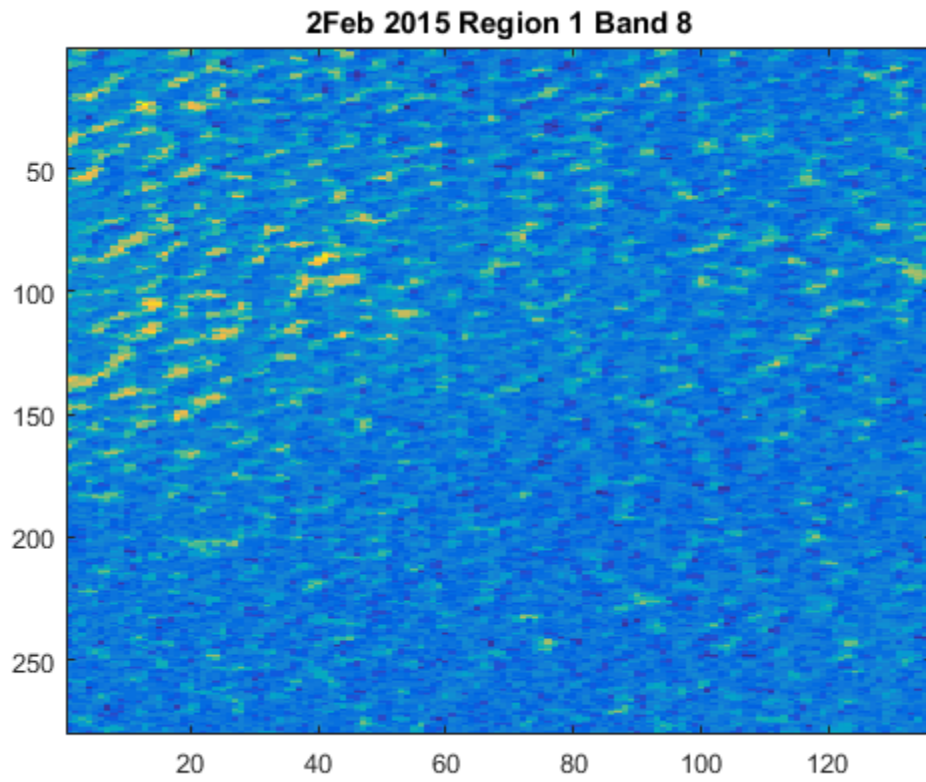


**Figure 40: Region 1 Sub-Image from 2 Feb 2015, Band 8**

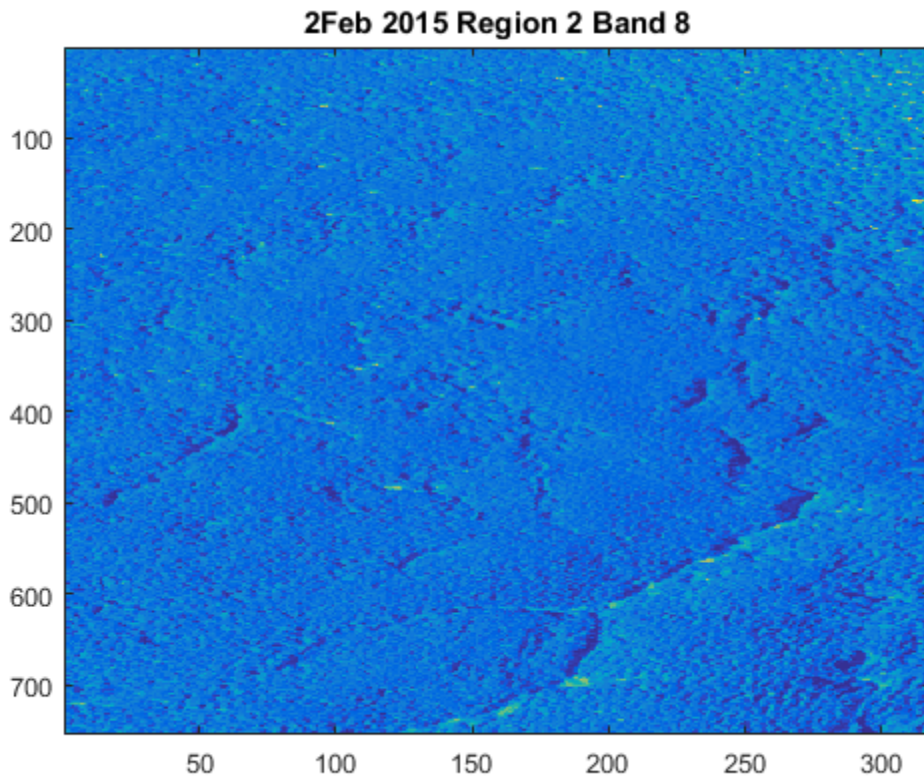


**Figure 41: Region 2 Sub-Image from 2 Feb 2015, Band 8**

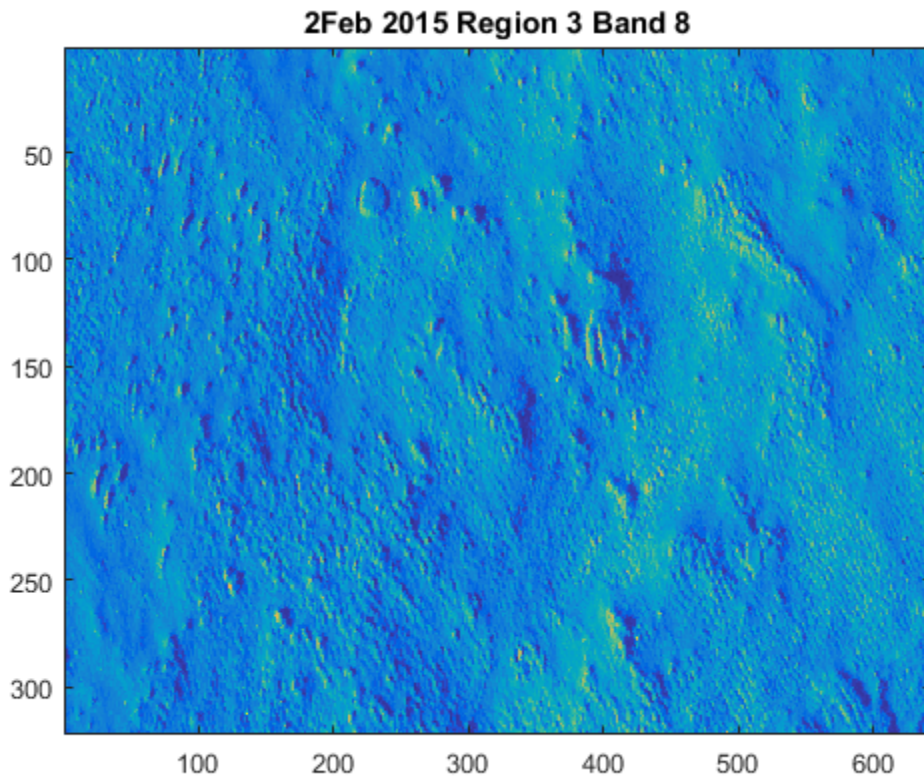


**Figure 42: Region 3 Sub-Image from 2 Feb 2015, Band 8**

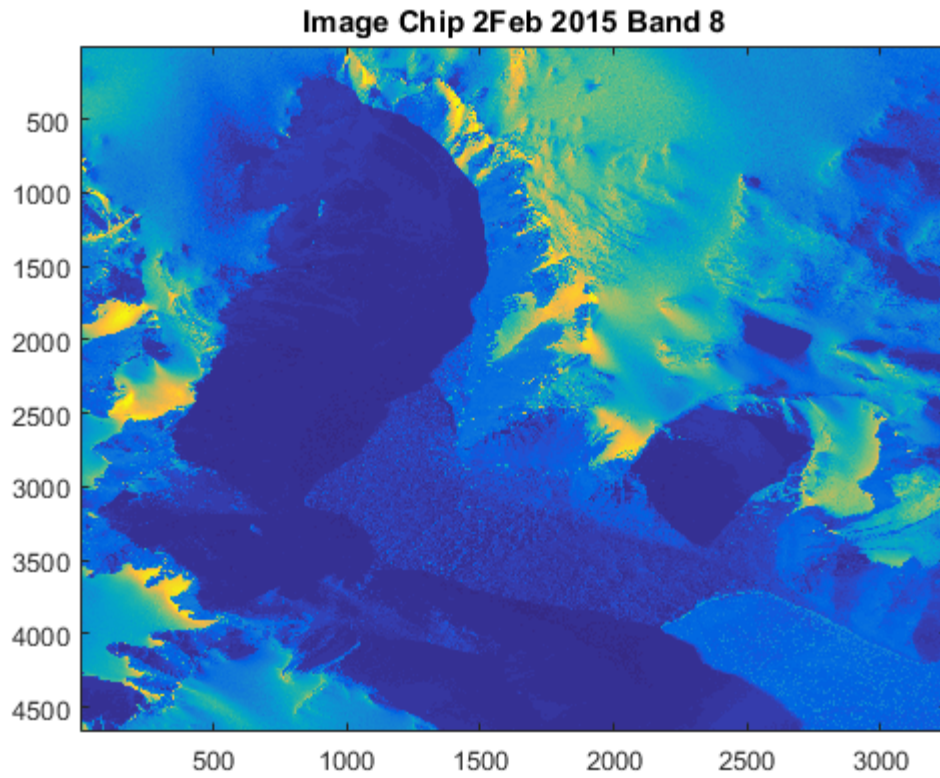


**Figure 43: Image Chip from 2 Feb 2015 (second image collected), Band 8**



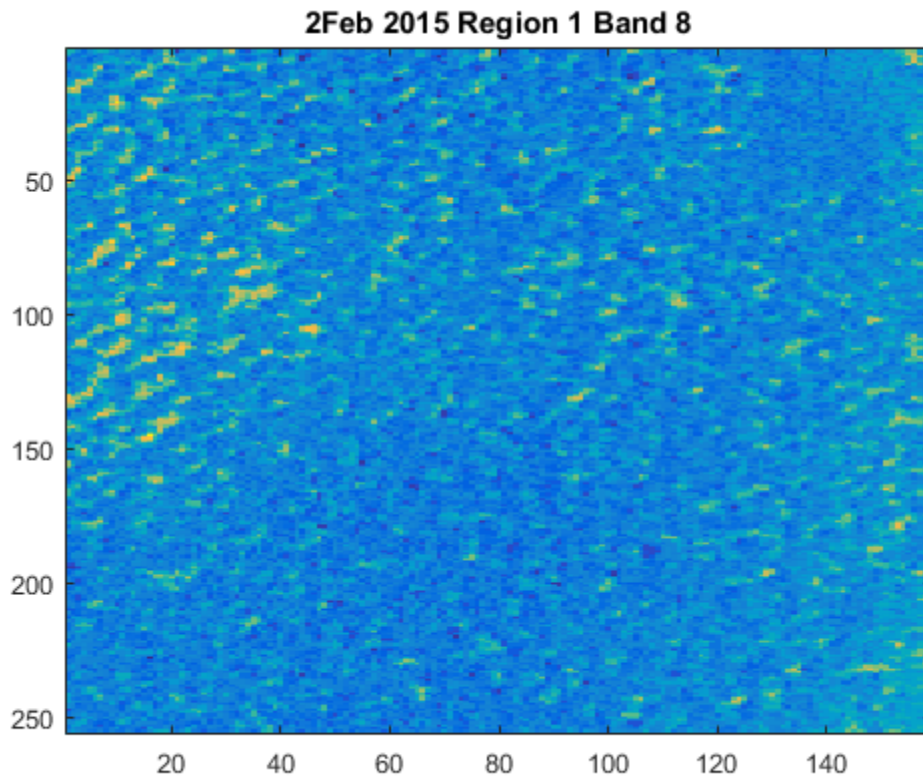


**Figure 44: Region 1 Sub-Image from 2 Feb 2015 (second image collected), Band 8**

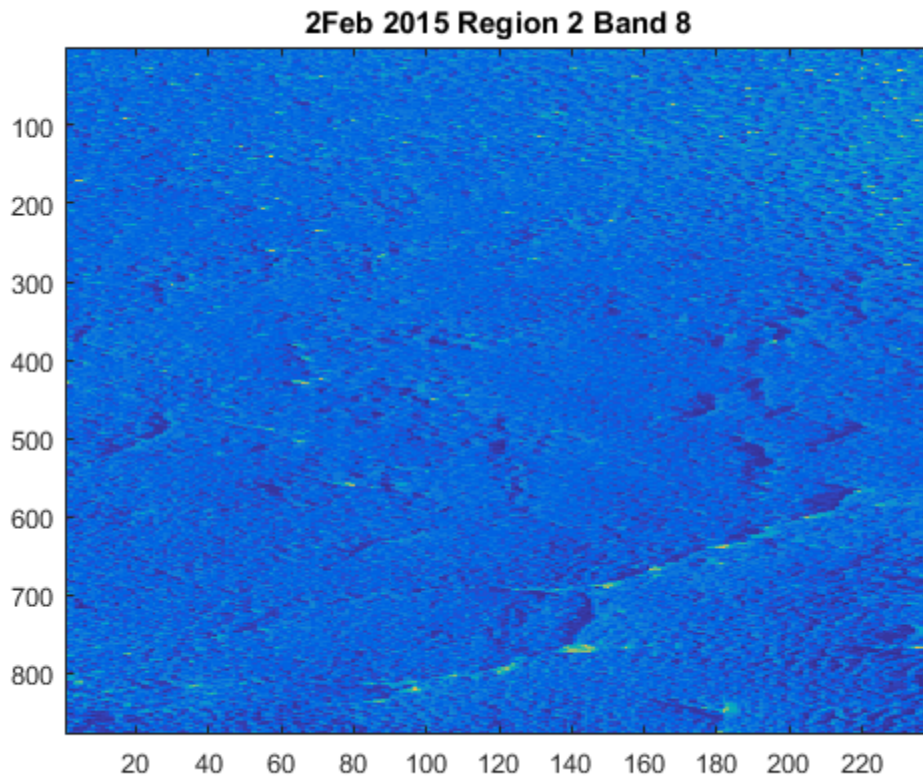


**Figure 45: Region 2 Sub-Image from 2 Feb 2015 (second image collected), Band 8**

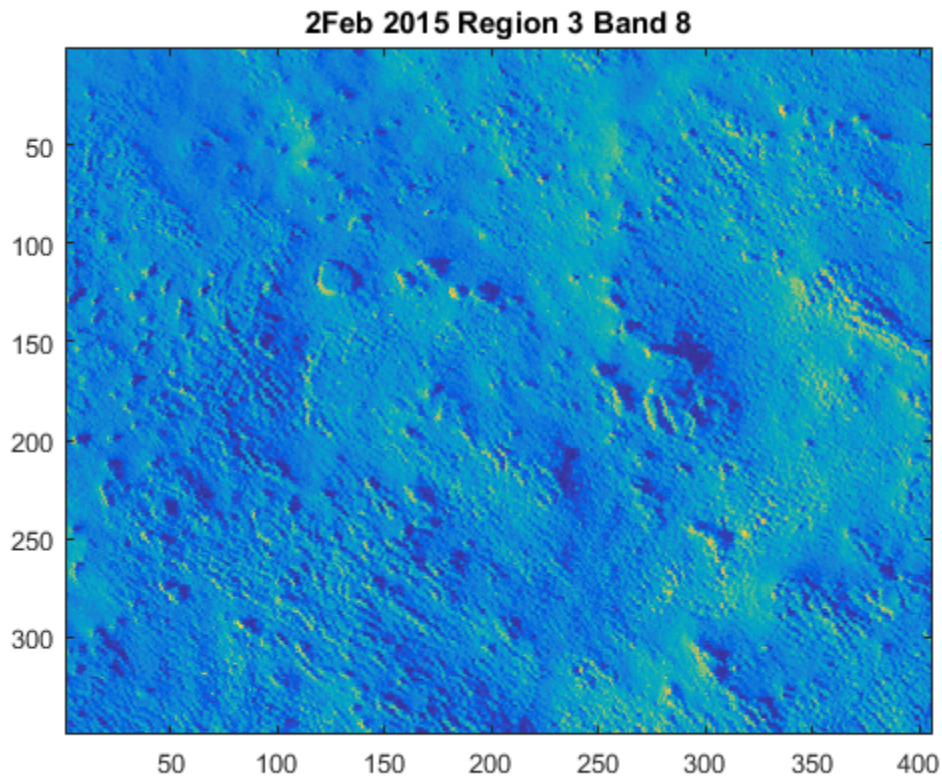


**Figure 46: Region 3 Sub-Image from 2 Feb 2015 (second image collected), Band 8**

## APPENDIX C: SUM-IMAGE PIXEL MEAN TABLES

This appendix contains a table for each image set's sub-image pixel means and standard deviations.

### Sub-Image Means for 11Dec

	Band 1	Band 2	Band 3	Band 4	Band 5	Band 6	Band 7	Band 8
Region 1 Mean	449.14	560.13	712.77	428.97	692.44	432.68	760.15	422.77
Region 2 Mean	395.90	473.36	577.03	336.95	539.51	330.38	583.13	322.04
Region 3 Mean	444.53	546.20	669.62	379.80	594.76	357.83	609.46	332.22

### Sub-Image Standard Deviations for 11 Dec

	Band 1	Band 2	Band 3	Band 4	Band 5	Band 6	Band 7	Band 8
Region 1 Std	54.44	82.47	115.42	70.12	112.95	70.54	117.01	63.63
Region 2 Std	39.21	60.67	88.10	54.49	88.86	56.24	97.75	53.11
Region 3 Std	25.09	39.45	59.65	37.48	63.20	40.17	73.06	41.05

**Sub-Image Means for 13Dec**

	Band 1	Band 2	Band 3	Band 4	Band 5	Band 6	Band 7	Band 8
Region 1 Mean	268.37	272.18	242.69	106.10	139.04	66.34	85.82	39.58
Region 2 Mean	271.81	310.77	360.57	209.16	340.66	207.89	373.31	202.22
Region 3 Mean	272.39	314.22	362.52	198.29	308.35	179.50	311.66	164.22

**Sub-Image Standard Deviations for 13Dec**

	Band 1	Band 2	Band 3	Band 4	Band 5	Band 6	Band 7	Band 8
Region 1 Std	35.14	40.61	36.90	15.76	21.25	10.01	13.28	5.37
Region 2 Std	33.83	52.81	79.00	51.42	88.73	56.90	103.78	55.44
Region 3 Std	11.16	24.70	50.31	35.93	64.79	42.02	82.14	44.61

**Sub-Image Means for 13Dec2**

	Band 1	Band 2	Band 3	Band 4	Band 5	Band 6	Band 7	Band 8
Region 1 Mean	234.88	240.58	218.67	97.56	129.24	62.88	83.68	39.37
Region 2 Mean	235.31	269.64	305.42	170.50	271.27	161.71	282.36	150.27
Region 3 Mean	231.36	262.06	293.73	156.83	238.99	137.07	234.02	123.35

### Sub-Image Standard Deviations for 13 Dec2

	Band 1	Band 2	Band 3	Band 4	Band 5	Band 6	Band 7	Band 8
Region 1 Std	35.24	39.00	35.60	15.37	20.34	9.60	12.37	5.25
Region 2 Std	44.59	68.66	99.13	61.56	105.97	65.63	117.50	61.66
Region 3 Std	11.83	22.67	44.28	31.44	56.42	36.65	71.89	39.26

### Sub-Image Means for 14Jan

	Band 1	Band 2	Band 3	Band 4	Band 5	Band 6	Band 7	Band 8
Region 1 Mean	320.15	409.84	544.00	339.17	561.22	348.35	628.53	339.36
Region 2 Mean	250.82	291.87	352.41	210.26	340.46	209.85	380.76	207.28
Region 3 Mean	255.41	300.57	363.12	204.30	317.81	186.62	329.17	175.41

### Sub-Image Standard Deviations for 14Jan

	Band 1	Band 2	Band 3	Band 4	Band 5	Band 6	Band 7	Band 8
Region 1 Std	83.03	136.60	200.75	122.17	200.47	120.70	200.06	96.91
Region 2 Std	35.41	59.25	91.49	59.57	99.89	63.49	111.93	59.12
Region 3 Std	11.92	27.25	57.27	41.12	72.48	47.13	92.13	51.05

**Sub-Image Means for 15Feb1**

	Band 1	Band 2	Band 3	Band 4	Band 5	Band 6	Band 7	Band 8
Region 1 Mean	221.16	231.37	218.96	101.09	132.44	67.47	88.39	41.51
Region 2 Mean	223.67	257.47	302.89	176.76	281.04	172.85	308.16	165.40
Region 3 Mean	229.44	268.06	316.17	175.38	268.21	157.95	272.30	142.55

**Sub-Image Standard Deviations for 15Feb1**

	Band 1	Band 2	Band 3	Band 4	Band 5	Band 6	Band 7	Band 8
Region 1 Std	27.00	32.35	32.03	14.72	20.21	9.92	13.31	5.62
Region 2 Std	21.25	36.94	62.26	43.47	78.23	50.74	98.61	52.79
Region 3 Std	9.51	22.43	49.05	36.39	64.59	42.61	83.84	45.27

**Sub-Image Means for 15Feb2**

	Band 1	Band 2	Band 3	Band 4	Band 5	Band 6	Band 7	Band 8
Region 1 Mean	217.73	230.56	221.17	103.06	136.07	69.93	93.04	44.18
Region 2 Mean	212.64	240.49	271.42	151.15	232.15	138.63	239.39	127.13
Region 3 Mean	214.63	246.23	276.90	147.59	219.69	126.70	211.23	109.83

### Sub-Image Standard Deviations for 15Feb2

	Band 1	Band 2	Band 3	Band 4	Band 5	Band 6	Band 7	Band 8
Region 1 Std	26.22	31.98	31.33	14.05	19.55	9.48	12.79	5.39
Region 2 Std	21.72	36.41	58.06	39.54	67.96	44.42	81.70	44.33
Region 3 Std	7.62	17.36	36.38	26.64	47.69	31.33	61.78	33.44